Dynamic and Mechanical Reinforcement in Gels of Synthetic and Biological Origin

MASTER'S THESIS

Heraklion, 2020

Dimitra Founta

UNIVERSITY OF CRETE

DEPARTMENT OF MATERIALS SCIENCE AND TECHNOLOGY

ACKNOWLEDGEMENTS

Foremost, I would like to express my sincere gratitude to my supervisor, Prof. Dimitris Vlassopoulos for giving me the opportunity to work in his lab and for the continuous support, motivation and enthusiasm he has provided me the past two years. I would really like to thank him also for the immense knowledge and experiences I gained. His guidance helped me in all times throughout my thesis where he helped me to discuss ideas, to meet excellent people/scientists and giving me the one amazing opportunity to travel around Europe. Moreover, I would like to thank my co-supervisor Prof. Peter Fischer and collaborator Caroline Giacomin from ETH Zürich for working with him and his team and of course all the discussions and great time I had in Zürich. Next, I would like to thank Dr. Esmaeel Moghimi, who was my advisor throughout my first year of my masters and played an important role, since he was always very helpful and positive. Also, I would like to thank Prof. Christos Likos and his PhD student Iurii Chubak for their great help and the great insight they provided with their simulation analysis. I am very grateful to the senior lab members, Prof. George Petekidis and Dr. Benoit Loppinet for the insightful comments and of course for kindly lending us the van which made our commute fun and safe.

Regarding the present fellow lab members … Special thanks to Katerina Rementzi, first for her massive help especially regarding the hagfish project and very importantly for all the discussions we had concerning science as well as everyday life. Big thanks to the, soon to be Drs, Manos and Nikos, great friends of years, who were and are always there whenever I needed them. Thanks for the awesome road trips, dinners, discussions and jokes we shared. Antje, thank you for introducing me and helping me with DLS and for the creative spirit and Antonis for being an amazing guy with the best "patents". Without his contribution my work would have been much more difficult. Consigllia, the 'fake' Italian who ended up being my klouva partner and teaching me how to drive –again- . Daniele P. for his helpful discussions and being also the best host for our pizza parties. Peponaki and Christina ("kai poios einai kala?") were always fun to be around and helped cope with everyday issues. Stelios for providing the best covers and also for gifting me the best mask. Mohan for the fun and honest discussions and comments he made. Andrei, our Russian guy for his fun attitude and memes and Nikos for the weird noises. Captain, our group meeting coordinator, for his hilarious commentaries. Also, I would like to thank new and past lab members Thanasis B., Panagiota B., Antonio G., Leo G., Maria K., Emmanuela F.

On a more personal aspect, I am very thankful to my friends Maria, Niki, Elisavet, Pantelis, Nikoleta for coping with me and my drama queen attitude at all times and for all the fun we had together during this years. On the same note, I am more than grateful to my partner -both in life and in crime- Christos, for being the most kind and loving person and a huge support at both fun and difficult moments. Melvin, for being the best writing buddy.

Last but definitely not least, I would like to thank from the bottom of my heart my loving parents Dimitris and Maria , first of all for helping me achieve my goals and teaching me to believe in me. Also my sister, Dioni and her fiancé Nikos for being the best company, having great laughs together and supporting me. At last, I would like to thank my brother, Kostis who was the most fun roommate and has the best decoration skills.

ABSTRACT

We investigate the dynamic and viscoelastic properties of associating polymers forming gels. Our study addresses two challenges, the detailed characterization of the associating moieties, and the understanding of the properties of the formed networks, especially in the context of mixtures where mechanical reinforcement represents the main target. To achieve our goals, and in view of potential applications, we use both synthetic and biological macromolecules. First, we examine the self-assembly mechanism of telechelic star polymers comprising diblock copolymers in selective solvents. They can be thought of as building blocks of responsive supramolecular materials. We study the effect of key parameters like they functionality (f) and fraction of the associating (solvophobic) groups on their self-organization mechanism and dynamics in dilute solution. Next we focus on improving the mechanical properties a mucus hydrogel formed by the mucin proteins derived from hagfish mucin vesicles by adding nanofillers or even a second network. We test different fillers and identify the consequences of interactions between the mucin matrix and fillers by means of linear and nonlinear (shear and capillary break-up extensional) rheological measurements. Hence, we manage to establish protocols for reinforcement. Our findings offer insights for linking the properties of these gels to their structure and for designing such soft composites with tunable rheological and mechanical properties.

TABLE OF CONTENTS

CHAPTER 1: INTRODUCTION

Soft matter comprises a vast range of materials, which interpolate between simple liquids and solids. Thanks to Pierre Gilles de Gennes , who was awarded a Nobel prize in physics in 1991 [1], "soft matter" became a new discipline in modern physics. The materials belonging to this family are consisted of mesoscopic range components, amongst them we can find liquid crystals, gels, biological membranes, colloidal suspensions, polymer solutions, polymer melts etc. Impulsive organization of individual building blocks into ordered structures due to external stimuli response is ubiquitous in most materials and all living organisms in nature [2]. Nature serves as the model for stimuli-responsive polymers, but it remains a challenge to create materials that interact with, or respond to, biological environments. Inspired by this, a remarkable effort is made aiming to understand and emulate this responsive behavior to such incentives (i.e., temperature [3]–[5], pH[6]–[8], light[9]–[11]). Soft matter self-organization actually can allow for controlled design, development and tunability of its structure assembly. In addition, recent advances in polymer chemistry have led to the synthesis of various copolymer architectures, paving the way for new responsive building blocks for composite materials with optimal physical and mechanical characteristics. Polymer systems can be developed into a variety of functional forms to meet industrial and scientific applications and can range from biological to synthetic. Patchy particles, i.e., particles with directional interactions that enable their self-organization into higher-order structures, are playing a primary role as novel building blocks of this new class of materials. Functionalized biomolecules, like DNA-grafted colloidal particles represent such an example of soft patchy particles. It is shown that can undergo aggregation due to interparticle interaction when temperature is reduced and lead to complex self-assembling structures[12]–[15]. However, the DNA grafting process is a very complicated and difficult step. A simpler alternative is achieved by using associating polymers, where there are units capable of interacting reversibly with similar units of other associating polymer chains. Hydrogels represent also a class of supramolecular networks which are ubiquitous in daily life, with applications ranging from food science, medicine to cosmetic industry. A polymer gel is a soft material capable of undergoing large deformation whilst swelling and absorbing water molecules. In turn, a deformed gel can change its chemical potential, contributing to energy exchange. Thus, a

polymer gel a variety of stimuli-responsive actions with respect to external environmental changes. Mucus is a kind of gel consisting of low amount yet high molecular weight mucin glycoproteins (~3%) that can form a polymer matrix of high water intake (~95%) with low modulus value, infused with inorganic salts. Mucus forms a dynamic semipermeable barrier that allows the exchange of helpful substances, i.e., nutrients, water, gases while being impermeable to most bacteria, toxins and other pathogens and they can entrap them and repel them [16], [17]. So far, their main application is to protect and lubricate human and animal organs. However, novel applications can emerge if we optimize their mechanical properties and of course the source. There are many different kind of mucus of different origin (i.e., gastric, mucosal, colon mucus etc.). The mucin concentration, the functionality (possible additional interactions or degradation) and the way of acting at different environments (saline or not) vary with the protein origin. For this reason, scientists target the mucus secreted from animals like porcine, snail or in our case hagfish in order to study and enhance mechanical properties and very importantly increase the resource yet decreasing cost. In this work, we investigate the tunable properties of polymeric networks of both synthetic and biological origin. Telechelic star polymers (TSPs) are well-defined synthetic building blocks that allow molecular tunability by simply changing some key parameters (i.e., composition, functionality). Compared to mucus nanocomposites, these building blocks are very small in size, yet both lead to reversible network formation. Therefore, by studying these two systems, we enhance our understanding of the fundamentals of physical network viscoelasticity and mechanical response vis a vis the role of molecular (molar mass, fraction of associating groups, charges, internal conformation and structure) and external (temperature, pH) parameters. In chapters 1-4 we provide the needed background (motivation, literature, materials and methods), while in chapters 5,6 and 7 we address the self-organization mechanisms of TSP building blocks into a percolated network and how is affected by different parameters. Subsequently, chapter 8 presents the rheology of a biological mucus system made of hagfish and two different ways of mechanical toughening, with addition of (i) nanocomposites and (ii) a second polymeric network.

CHAPTER 2: BACKGROUND

2.1 Soft Colloidal Systems

Soft colloids, such as microgels or star polymers, can be thought of as hybrids with properties encompassing both polymeric and hard colloidal features. These include stimuli-responsiveness, complex state transitions and tunable rheology. Due to these features, soft colloids can find wide-ranging applications as drug release agents, stimuli-sensors (e.g., pH, temperature), surface stabilizers in the food, oil and cosmetic

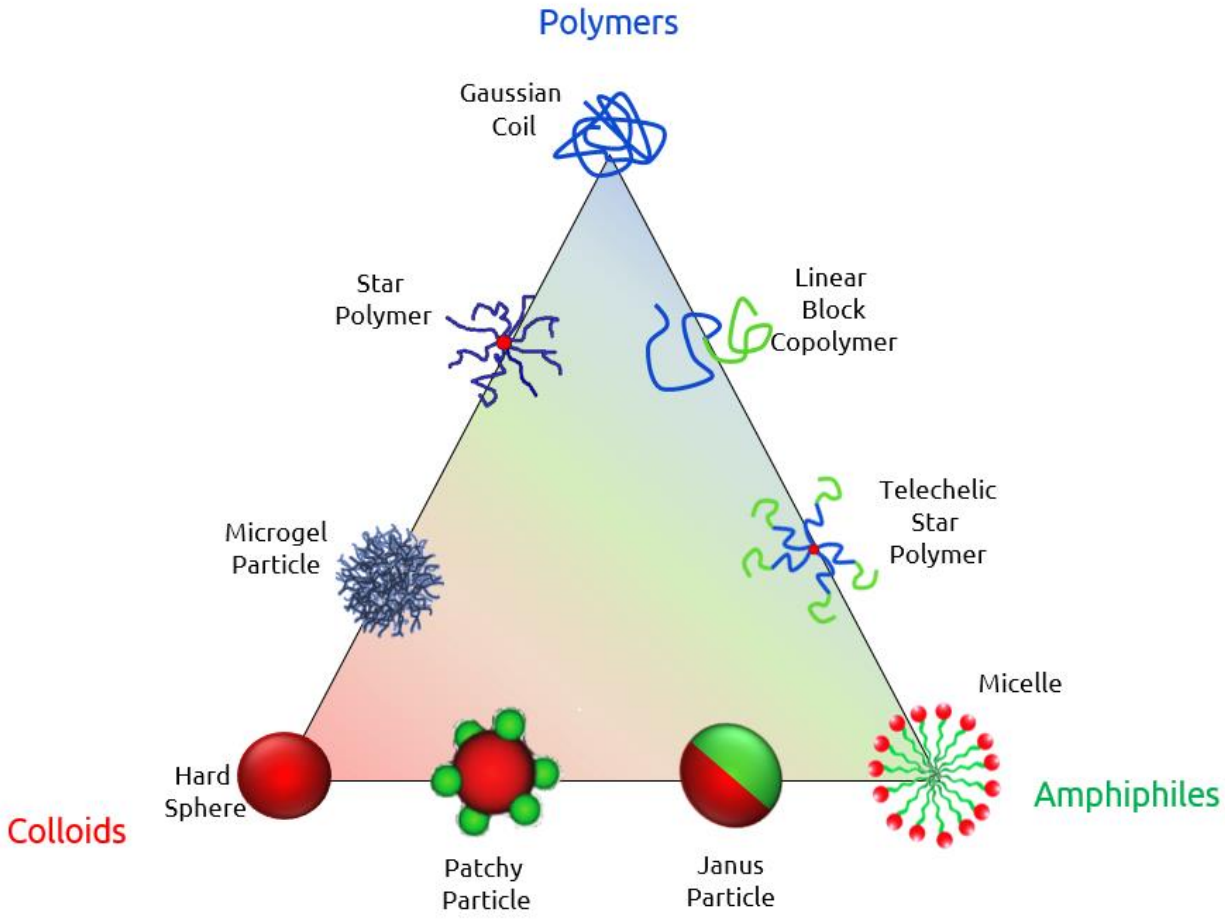

Figure 2.1: A ternary schematic diagram with three pillars of soft matter, (a) polymers (b) colloids (c) Amphiphiles on each top. More complex structures resulting from combination of two pillars are shown on the sides. In this thesis, we use intermediates of all categories. Towards the top, the softness increases since we move to a more polymeric character.

industry and viscosity modifiers. In addition, soft colloids display exceptional complex structures, and have become new model systems (in addition to hard spheres) to mimic the phase behavior of molecular systems. This alternative to rigid particles is promising because soft colloids are highly deformable that can adjust their conformation at wish. Depending on the application, the latter is governed by bulk elasticity and surface tension and may yield an increase of adsorption energy by orders of magnitude relative to rigid particles [18]. Figure 2.1 illustrates some soft colloidal systems including those used in this thesis, e.g., microgel particles like CARBOPOL or amphiphilic polymers like telechelic star polymers [19]. In general, to achieve tunable responsive macroscopic properties a synergy of the following parameters: (a) the type of monomers and their way of interactive with the solvent, the interactions between monomers ; (b) molecular characteristics like architecture, flexibility, block size ratio, molecular weight, molecular weight distribution, and (c) the control of exchange kinetics. Fundamental research has set the goal of investigating the principles that allow tailoring the properties of associating soft materials amenable to applications. Both star diblock copolymers and nanocomposites used for improving mechanical properties of mucus systems belong to this family.

2.2 Telechelic Star Polymers (TSPs)

The term ‘telechelic’ originates from the junction of two Greek words:, tele- means ‘remote/end’ while -chele means lip/claw. Telechelics are defined as polymeric molecules with reactive terminal groups that have the capacity to form intra-molecular as well as inter-molecular bonds[20]. While in most cases the term telechelic polymer is used when both ends of a polymer are functionalized, are also considered as telechelic macromolecules when only a part of the chain is functionalized but is able to interact with atoms in the same molecule (intra-molecularly) as well as to form bridges with other molecules (inter-molecularly). A well-established strategy to tailor rheological properties of polymeric materials is to incorporate associative groups

known as “stickers”. This way there is a tendency to organize into small aggregated leading to formation of physical sol or gel depending on the amount of the sticky ends. In comparison, conventional telechelic polymers have by default one sticky chain end therefore uniform distribution along the backbone thus facilitating the formation of more organized structures. In more detail, telechelic polymers is a class of reactive polymer possessing reactive functional groups at the chain ends, which are, not from monomers, deliberately introduced for further reactions [21]. Reactive polymers at chain ends represent promising building blocks for other classes of polymers, such as block copolymers and network polymers[22], [23]. The word “telechelic” was first used as an expression of these terminal reactive polymers in 1960 by Uraneck and coworkers to describe investigations of end group linkages of polybutadienes [24]. In this thesis, we focus on Telechelic star polymers (TSPs). TSPs are star polymers with associating groups at the chain ends (depending on the environment, e.g., selective solvent), thus attractive end arm sites [25], [26]. They comprise f (functionality) AB-block copolymers (arms) grafted on a common center with their solvophilic, A-blocks being at the interior of the star, and their solvophobic, B-blocks attached to the end of each arm. In what follows, N_A and N_B denote the number of A- and B-type monomers in a star arm, respectively, whereas stands for the ratio. The single-molecule behavior as well as the resulting many-body properties of concentrated systems depend on three parameters: the functionality f of the stars, the size ratio between A- and B-blocks and the attraction strength between the solvophobic B-blocks. Such systems have been investigated in the melt state, where association of the outer block is due to the enthalpic A-B interactions; in this case the B-block becomes attractive by changing the temperature, but it could also be a strong dipolar group such as zwitterion. The possible interplay of intra- and inter-molecular association reflects the competition between configurational entropy and attraction energy: for example, at high temperatures the association between different end groups will be suppressed, whereas at low-temperatures it will be a typical configuration. Such systems have been investigated in the melt state, where association of the outer block is due to the enthalpic A-B interactions, and their structural and viscoelastic properties have been shown to strongly depend on the temperature-dependent interplay of intra- and inter- molecular

associations. In solution, on the other hand, the attractions between outer blocks become stronger upon worsening solvent quality for one block, i.e., upon lowering temperature below the cloud point of the outer B-block. This, consequently, leads to the formation of soft patchy particles. In this work, we shall address these questions in order to explore the exciting possibilities for designing new materials with tailored dynamics.

2.3 Biology of Hagfish and its Slime

Hagfish are marine nocturnal fish in habit and can be found in most oceans. They are eel-shaped, slime-producing, jawless , spineless and belong in the species Myxini, also known as Hyperotreti [27]. They live buried either in mud or sand and eat polychaetes –marine worms- and other invertebrates. There are known to exist 67 different species of Myxini but the most studied one are Pacific Hagfish (Eptatretus stoutii) [28] and Atlantic Hagfish (Myxine glutinosa)[29]. In this work we focus on the Atlantic Hagfish species. A schematic illustration of the actual sea creature is shown in Figure 2.2(a). Hagfishes are ancient creatures and haven't evolved for about 300 million years. One of the most distinctive features of hagfish is their defense mechanism from predators, which consists of rapidly releasing large amounts of slime exudate when threatened, thus clogging the predator's mouth and gills [30], [31],[32]. The slime itself forms very fast (a few milliseconds) when the exudate is released from its ventrolateral slime glands that are located on both sides of its entire body as it is also shown in Figure 2.2(b) [33]. Interestingly, slime formation takes place when an extensional stress is applied (deriving from the mouth suction of predators), while it collapses in shear, so the hagfish can (shear-)escape if trapped by simply making a knot [34]. The exudate consists of two main protein components; these are the mucin vesicles and protein skeins. Skeins are coiled up proteins that unravel due to osmotic pressure and their length is about 15-30 cm. They explicit a very unique way of self-packing (Figure 2.2(c)) and despite their length, they can unravel without tangling. When skeins are released,

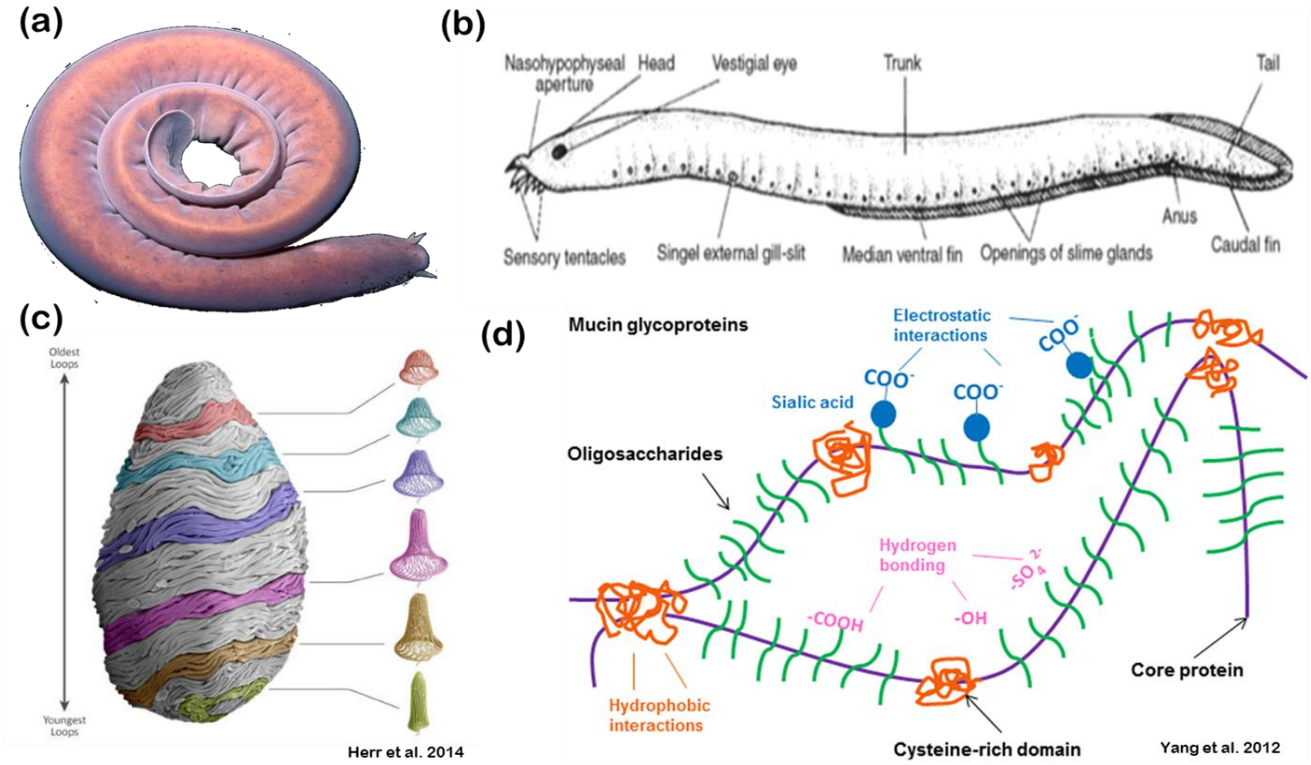

Figure 2.2: (a) The Atlantic hagfish (Myxine Glutinosa). (b) Its different parts and in particular the slime-glands. (c) Cartoon of the skein proteins and how they are packed (Herr et al. 2014). (d) Simplified animated version of mucin-like glycoproteins as drawn by Yang and coworkers in 2012.

a process triggered with very low mechanical stress, they make the backbone of the slime which is a soft neutral which offers great elasticity to the hydrogel. Then again, mucin vesicles are capsules that entrap mucin-like glycoproteins [35], [36]. When in contact with seawater and more importantly with divalent ions of Ca^{2+}, it boosts for the vesicles to open up and release the encapsulated proteins due to means if osmotic pressure [37] . These mucin-like proteins make a rigid, brittle polyelectrolyte network. These two combined form the hagfish slime, which is the most dilute hydrogel known to date (99.996% water). It has triggered a lot of interest in the direction of designing new biomaterials (i.e., smart fabrics, food stabilizers, drug carriers , advanced hydrogels) [38]. However, since the overall structure, mechanism of formation and chemistry are still not completely understood, it is meaningful to pursue systematic investigations of individual constituents. In this spirit, we have decided to isolate and investigate mucin proteins. One distinguishing feature is that effective gelation for mucin proteins of an elastic network (mucus) can occur with 0.01-0.02% wt. [34],[39].

The main target of this study is to make this mucus hydrogel “stronger” by improving its mechanical performance. Adding filler nanoparticles is one of the traditional approaches to toughen elastomers. In this study we follow such an approach by both forming a double network and using nanoparticles, as described in detail in the following.

2.4 Reinforcing mechanisms of polymer networks

2.4.1 Interpenetrating double networks (DNs)

Hydrogels are usually composed of a hydrophilic polymer that forms a single network (SN) which can absorb water molecules and thus swell. This type of network is weak and highly elastic. The lack in mechanical strength is mainly due to the solution-like nature of hydrogels since there is low density of polymer chains in the solution and thus small friction between them. Another reason is the heterogeneity of the network structure caused during the gelation process which is known as a result of large-scale imperfections [40], [41]. When a force is applied to a gel with heterogeneous structure, stress is concentrated at the shortest segment, leading to failure of the sample even at very low values (in the form of propagating cracks). Conversely, load-bearing biological soft tissues - like cartilage or tendon- are much stronger. At the synthetic level, there is a new class of hydrogels known as double-network hydrogels, where a high molecular mass neutral polymer network is merged within a swollen heterogeneous polyelectrolyte network of shorter chains [42]–[44]. Double-network gels are promising materials that allow for high water content while having high mechanical strength and toughness. One way of reinforcing single networks is to form interpenetrating networks, akin to double networks. DNs are a special type of network structure consisting of two types of polymer components with distinct characteristics:

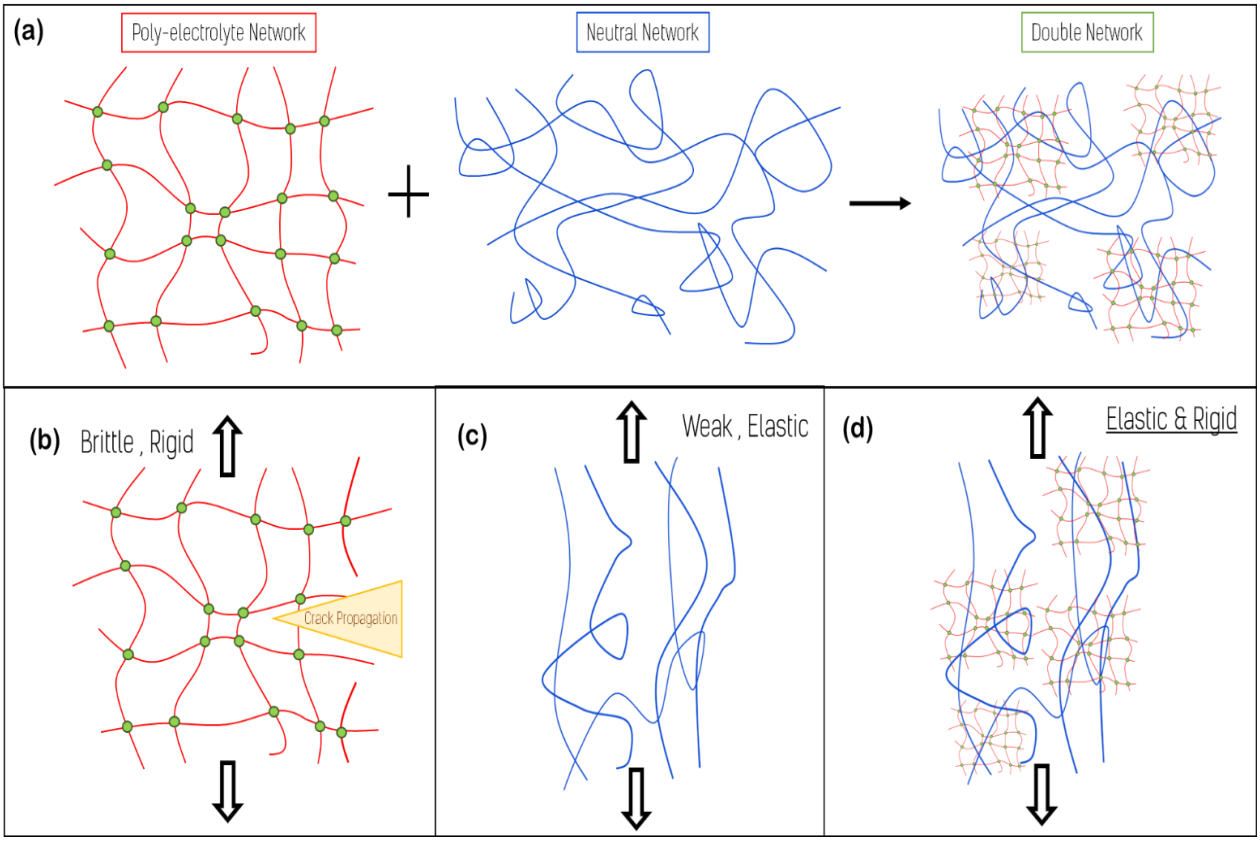

Figure 2.3: Single network components comprising a double network gel and response to an applied force. (a) Minor poly-electrolyte network and major neutral polymer network. When mixed together, they form a complex interpenetrated structure. In (b), (c), (d) we show simplistic illustrations of the three deformed networks due to the effect of an applied force.

the major soft and ductile network ($E_n=k_BT$) [45] which comprises loosely cross-linked neutral polymers and the minor which is a densely cross-linked polyelectrolyte network that is rigid and brittle ($E_n>>k_BT$) [42],[46]. The 'neutral' network corresponds to a what is known as a hidden length scale, (when the bonds of the other network break and the chain (e.g., protein) starts to unfold), whereas the 'charged' network has the sacrificial bonds, i.e., the ionic bonds that may easily break and recover; this is known as the bone fracture model [47]–[49]. The large number of crosslinks of the latter (stiff) network is primarily responsible for bearing the stress. These crosslinks form sacrificial bonds that break before the material fails. The deformable former network holds the gel together during extreme extension and redistributes stress to a large volume of the sacrificial bond network. The combination of the two networks (shown schematically in Figure 2.3) offers versatility and enhanced mechanical resistance. Based on the above, we may describe hagfish slime in the context of a double-network gel with the skeins (balls-of-

wool) being the backbone of the neutral network and the mucin-like glycoproteins comprising the polyelectrolyte component. In this thesis, we focus on the hydrogel component (i.e., the network of mucin-like glycoproteins) which is a charged single network formed by mucin-like GPEG proteins.

2.4.2 Nanoparticles as fillers for improving mechanical properties of polymer networks

Motivated by the famous lecture of Nobel laureate Richard P. Feynman "There's Plenty of Room at the Bottom" (Feynman, 1960) [50], the scientific community engaged in various revolutionary developments in the field of nanotechnology. They involved the ability to fabricate, characterize and manipulate artificial structure that can provide control of properties at nanometer scale. Several pioneering studies have revealed new physical properties of matter at intermediate scale between molecular and bulk. The class of materials known as nanocomposites are made of nanosized objects dispersed in polymeric matrices, and their macroscopic behavior arises from a combination of the novel properties of the individual building blocks and their mutual interaction. In this thesis, we focus on one particular kind of this family, nanoparticles of polymeric or colloidal nature and their role in potentially enhancing the mechanical strength of the weak mucin hydrogel. The use of nanoparticles to yield composite hydrogels has received a lot of attention over the years because of their potential to tailor the mechanical properties of composites in an unprecedented way, through molecular design of the network components. As already mentioned, toughening a polymeric network with nanoparticles depends largely on the interactions between the backbone of the gel and the particles. What is hard to characterize is the polymer-filler interaction. The attraction forces between particles, typically due to van der Waals and electrostatic (and maybe additional) forces, affect the particle-particle interaction and could deteriorate the overall performance of the composite [51]. The delicate balance between repulsion and attraction forces can be tailored by particle size, volume fraction, and surface modification [51]–[55]. Simulation results suggest that the presence of nanoparticles increase polymer packing density and could lead to an increase in the storage modulus [55], [56]. In case the particles are simply introduced

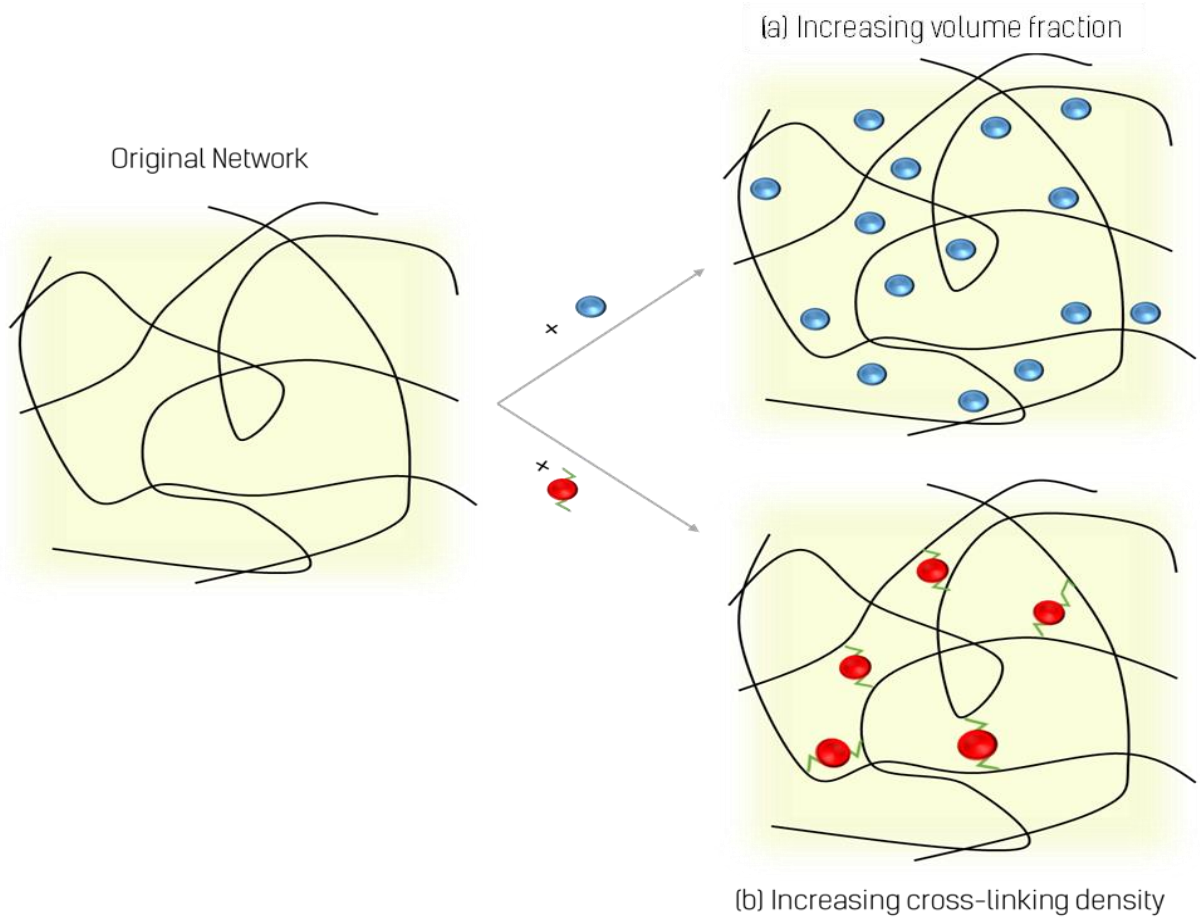

Figure 2.4: Schematic illustration of toughening mechanisms of a polymer network when nanoparticles are introduced. (a) Space-filling particles yielding an increase volume fraction and the elastic modulus (and viscosity) of the system, in general (b) Particles with binding sites: they interact chemically thus creating more bridges between the polymers and increasing crosslinking density hence the modulus of the system.

into the polymeric network, we consider them as space-filling, yielding an increase of the elastic modulus and brittleness. On the other hand, when particles are embedded via chemical interactions with the polymeric matrix, a stronger gel is formed. The two approaches are schematically illustrated in Figure 2.4.

CHAPTER 3: METHODS

In this chapter we introduce the basic theoretical background of the various experimental techniques and methodologies used in the present thesis. Details about sample preparation, measurement protocols and experimental setups are discussed. The main techniques used are dynamic light scattering (DLS) in the single scattering limit (photon correlation spectroscopy), small-amplitude oscillatory shear rheology (linear viscoelasticity) and capillary break-up extensional rheology (nonlinear response). Additional techniques, which have been utilized for material characterization, such as the turbidimetric analysis (UV-VIS spectroscopy) and zeta potential tests, are also briefly discussed.

3.1 Dynamic Light Scattering (DLS)

Dynamic Light Scattering (DLS, also known as Photon Correlation Spectroscopy or Quasi-Elastic Light Scattering) is an ubiquitous and non-invasive analytical technique used to measure the particle size distribution in size ranges of approximately 1 nm to 1 μm. The setup used for DLS experiments is the ALV-5000 (Germany) with Nd-YAG polarized monochromatic laser beam at a wavelength (λ) of 532 nm (Oxxius, France). In more detail, the single frequency beam after being vertically polarized through a series of lens and filters, hits the sample causing a scattering event due to the reaction of material elements in the solution sample, called scatterers. The scattered light caused by them fluctuating over time due to Brownian motion, is detected at a known scattering angle θ by a fast photomultiplier (PMT) detector, which is adapted on a goniometer. The variation of different angles allows us to have access at different length scales. The particles scattering of light gives information about their thermal motion, hence their diffusion. For controlling the temperature, an external bath circulating system was

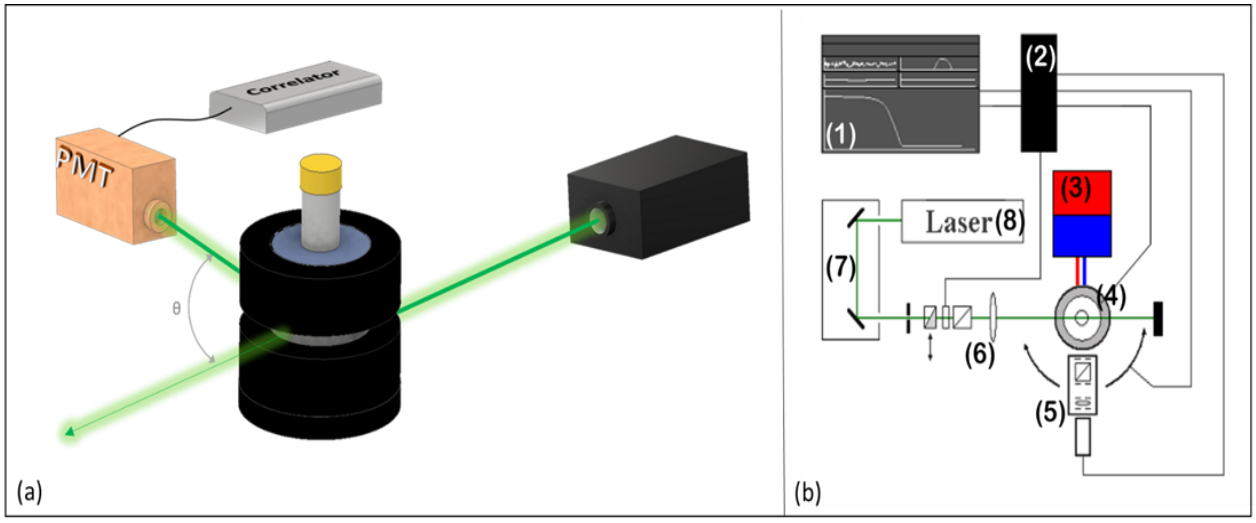

Figure 3.1: illustration of the Dynamic light scattering setup ALV-5000. (a) Schematic of the setup. The laser beam passes through the sample and illuminates it. The scattered intensity is collected by the high-sensitivity photon multiplier which is placed on a goniometer and based on the scattering angle θ the intensity signal is auto correlated via a correlator card (b) details of the setup: (1) computer receiving input from the correlator card (2). The laser (8) produces a beam directed to an opticam train including mirrors and polarizer (7. The beam then passes through a system of optical lens (6) and reaches the sample that sits in the DLS chamber (4). The temperature is controlled by means of an external bath (3) working with water circulation. Finally, the scattered light is collected by the photon multiplier which is placed on a goniometer (5) for measurements at various scattering angles θ

also used and has a range of 6°C-60°C .A graphic representation of the setup used is shown in Figure 3.1. Finally, a correlator transforms the received signal of the scattering intensity fluctuations of the solution into a digital signal, which is then auto-correlated for dynamic light scattering measurements (see Figure 3.2). Moreover in Figure 3.2, we illustrate examples intensity fluctuations and intermediate scattering function (ISF), reflecting the motion of small particles in the suspension (top) or of both large and small particles in the same sample volume (bottom). Based on the Stokes-Einstein-Sutherland equation, the larger the size, the slower the diffusion in the medium, and the larger the fluctuations (more scattering from large particles). On the other hand, the smaller the size the larger the diffusion in the medium and the faster the intensity fluctuations (less scattering by small particles). The scattering wavevector q is defined in terms of scattering geometry and is dependent on the scattering angle θ and some fixed parameter like the wavelength of the laser source in vacuum (λ) and the refractive index of the solvent (n) .This is known as the Bragg condition (Eq. 3.1) and specifies the wave vector component of the dielectric constant fluctuations that will give rise to a scattering angle θ.

$$\vec{q} = \frac{4\pi n}{\lambda}\sin\left(\frac{\vartheta}{2}\right) \tag{3.1}$$

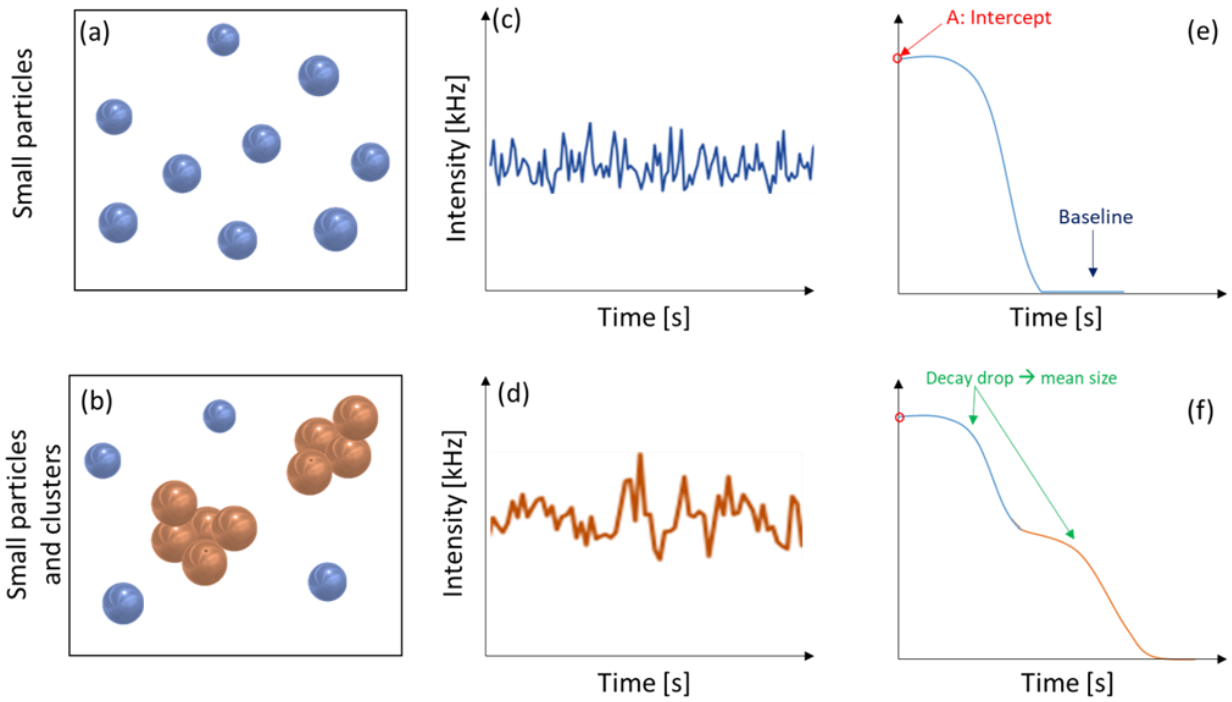

Figure 3.2: At the top, the scattering intensity (b) and its autocorrelation function (intermediate scattering function, ISF) (c) are shown for a system consisting of small particles (a). At the bottom, the same situation is illustrated for a system comprising both small particles and bigger clusters (b). In this case, a second slow mode appears in the ISF (f) and the intensity fluctuation peaks are larger and broader (d).

The scattering light is well approximated by the Rayleigh scattering model where the scattered intensity, I, Eq. 3. 2, is proportional to the sixth power of the particle radius, r [57]

$$I \propto \frac{r^6}{\lambda^4} \tag{3.2}$$

DLS is very sensitive to very low concentrations of contaminant size fractions such as filter spoil, dust from improperly cleaned lab-ware and aggregated particles, which may ruin the measurements. As already mentioned, DLS reflects the Brownian motion of the dispersed particles, which are constantly colliding with solvent molecules. These collisions cause a certain amount of energy to be transferred, which induces particle movement. The energy transfer is constant and therefore has a greater effect on smaller particles. As a result, smaller particles are moving at higher speeds than larger particles. The speed of the particles is quantified by the translational diffusion coefficient D, which we can be obtained by computing the intensity correlation function $g^{(2)}(q,\tau)$. The instrument by itself measures intensity autocorrelation function I<t> and with a correlator card can compute the $g^{(2)}(q,\tau)$ function. The normalized time

autocorrelation function of the intensity of the scattered light $g^{(2)}(q,\tau)$ for a given delay time τ is given by equation 3.3.

$$g^{(2)}(q,\tau) = \frac{<I(q,\tau)\cdot I(q,\tau+t)>}{<I(q,\tau)>^2} \quad (3.3)$$

Where I (t) and I (t + τ) are the intensities of the scattered light at times t and t + τ, respectively, and the braces indicate the averaging over t. For short time delays, the correlation is high because the particles don't have a chance to move to a great extent from their initial state. As the time delays become longer, the correlation decays exponentially, meaning that, after a long time period has elapsed, there is no correlation between initial and final states. This exponential decay is related to the motion of the particles, specifically the diffusion coefficient D. In many cases the ISF can be written in terms of the correlation function $g^{(1)}(q,\tau)$ of the scattered light field through the so-called Siegert relation (equation 3.4) [58] . A typical representation of the intensity correlation function is shown in Figure 3.2(d) for single particles and Figure 3.2 (f) for a solution with both single particles and clusters.

$$g^{(2)}(q,\tau) = 1 + \alpha \cdot [g^{(1)}(q,\tau)]^2 \quad (3.4)$$

α being the coherence factor, determined by the ratio of the detector area to the coherence area of the scattered light, which is usually a known and fixed parameter, in our case the value is α=0.36. In the simplest scenario of a homogenous dilute suspension of spherical particles under Brownian motion, $g^{(1)}(q,\tau)$ can be described as a single exponential decay with a decay rate of $\Gamma=Dq^2$ (equation 3.5).

$$g^{(1)}(q,\tau) = \exp(-\Gamma\tau) = \exp(-Dq^2\tau) \quad (3.5)$$

Once you get the value of diffusion coefficient you can estimate the hydrodynamic ratio using the Stokes-Einstein-Sutherland equation (Eq.3.6) [59]–[62].

$$D = \frac{k_B T}{6\pi\eta R_H} \quad (3.6)$$

Where k_B is Boltzmann's constant, T the absolute temperature during the measurement, η the dynamic viscosity of the dispersant at the desired temperature and RH the hydrodynamic radius of the particle.

Based on the form of the ISF we can proceed with different ways of analysis. In the present work, to analyze the data we used mainly the CONTIN algorithm [57].

3.1.1 CONTIN analysis

The CONTIN method is a more complex distribution method since it involves analysis of multi-mode distributions. In this case, is used the correlation function $g^{(1)}(q,\tau)$ of the particle suspension along with the CONTIN algorithm [57], [58] to evaluate the corresponding distribution of relaxation times from the distribution of decay rate G (Γ). Since the peaks in G (Γ) correspond to scattering events deriving from the monomers are usually sharp, they directly indicate the characteristic diffusion time τ_p of the particles. However, when aggregation takes place, we observe a broader peak that corresponds to the characteristic diffusion time of the assembled clusters (τ_c). Moreover, large aggregates may not be non-diffusive if their size prohibits a purely Brownian motion. G (τ) reflects the amount of scattered light with relaxation time to which are contributions from the characteristic diffusion time of and the lifetime of scattered particles. The function G (τ) is usually computed from the field correlation function (eq. 3.7) by means of the CONTIN algorithm.

$$g^{(1)}(q,\tau) = [g^{(2)}(q,\tau) - 1]^{1/2} \quad (3.7)$$

The CONTIN algorithm performs a numerical inverse Laplace transform of the correlation function $g^{(1)}(q,\tau)$. The decay rate distribution is given by a summary of several exponential decay functions that decay at different rates; this approach is very efficient for polydisperse and complex systems [59]. A generic model is represented by equations 3.8-3.9 below.

$$g^{(1)}(q,\tau) = \int G(\Gamma)\exp(-\Gamma\tau)\, dln\Gamma \quad (3.8)$$

$$G(\tau) = G(\tau)monomer + G(\tau)cluster = \frac{A_2}{\sqrt{2\pi\sigma_2^2}}\exp\left[-\frac{(ln\tau - ln\tau_2)^2}{2\sigma_2^2}\right] \quad (3.9)$$

The main point is to use CONTIN and to invert the decay rate (Γ) distribution for different values of the regularization parameter α. The quality of fitting depends on the curvature of the distribution. The proper selection of α is tricky because even a small difference can alter significantly the outcome of the fit and thus the diffusion coefficient value.

3.2 UV/Vis Spectroscopy

The instrument used in ultraviolet–visible spectroscopy is called a UV/Vis spectrophotometer. The machinery used for experiments was the UV-Vis spectrometer LAMBDA 950 by Perkin Elmer (USA) and the UV-Vis spectrometer Cary 300 by Agilent Technologies (USA). Both have a range of wavelengths from 200nm to 800nm. The main idea of this method is that these instruments can measure the light that is either absorbed or transmitted from various dilute solutions [60]. In brief, the non-monochromatic light derived from the source is analyzed into different colors through a set of lenses and a monochromator prism and hits the sample. A schematic representation is presented in Figure 3.3. Based on the components of the investigated sample, the characteristic absorbance or transmittance corresponds to an intensity spectrum, ideally with a clear peak [61]. Based on that, we can extract the absorption

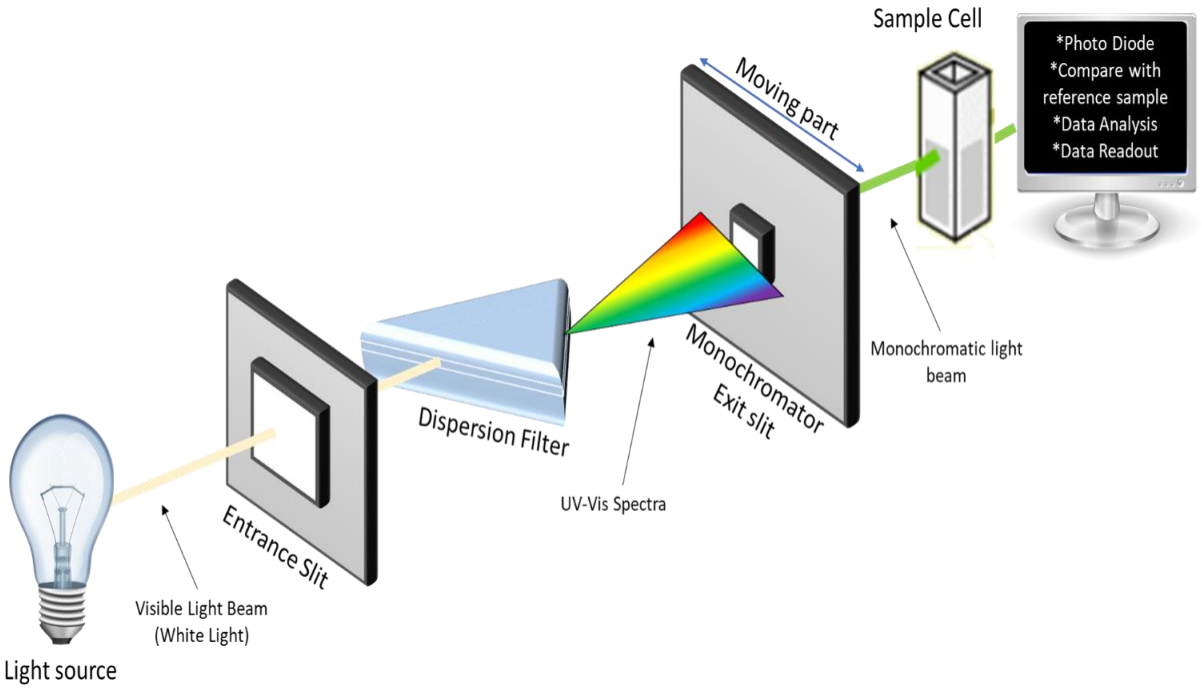

Figure 3.3: Simplified schematic illustration of the principle of operation of a UV-Vis Spectrometer.

for the wavelength that we are interested in and through the Bouguer-Beer-Lambert law (equation 3.10) calculate the concentration [62], [63].

$$log\ (^{Io}/_{I})\ = log(^{100}/_{T(\%)}) = A = \varepsilon dc \tag{3.10}$$

Where I_o is the intensity of the monochromatic light entering the sample and I the intensity of the light emerging from the sample. T (%) is the % transmittance calculated by the I_o/I ratio. A = log (I_o/I) [-] is the absorption of the constituents, d [cm] is the optical path size or else the length of the cuvette. Finally, ε [$M^{-1}cm^{-1}$] is the molar absorption coefficient and c [M] is the molar concentration. According to the aforementioned law, the technique assumes a measurement of the given relationship between the light intensities I and I_o. When measuring a sample, one has to account for the loss due to the solvent itself and potential reflection due to the cuvette surfaces. In order to eliminate this error, a reference measurement is performed. More detailed, the

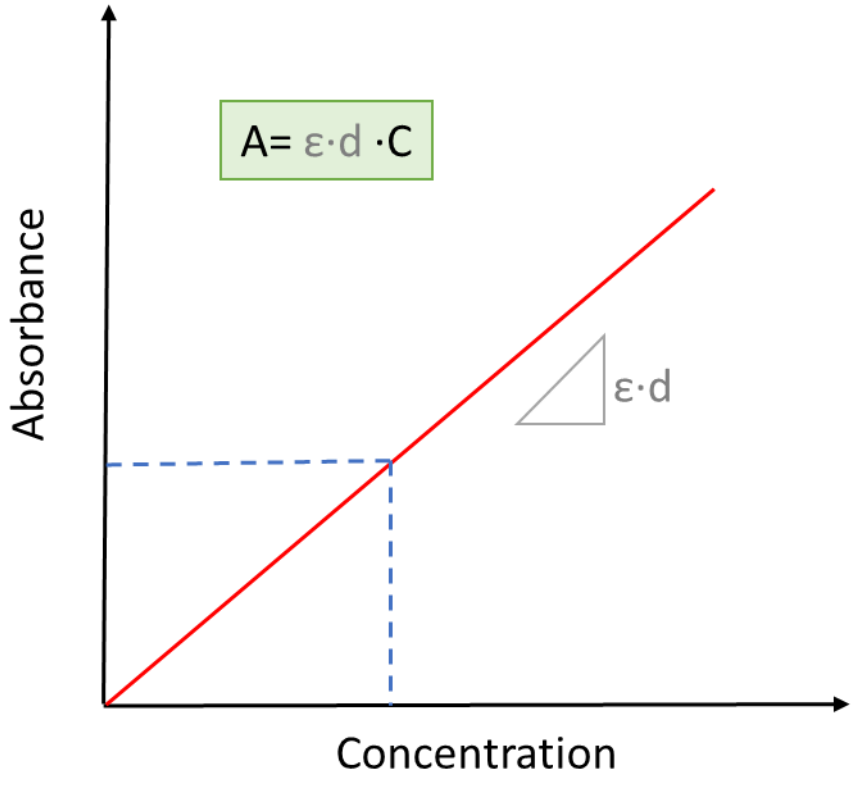

Figure 3.4: Concentration calibration curve based on the use of the Beer-Lambert law.

absorbance of radiation in the UV-Vis range causes atomic excitation, which refers to the transition of molecules from a low-energy ground state to an excited state. Before an atom can change excitation states, it must absorb sufficient levels of radiation for electrons to move into higher molecular orbits. Shorter bandgaps typically correlate to absorption of shorter wavelengths of light. The energy required for molecules to undergo these transitions, therefore, are electrochemically-specific. A UV-Vis spectrophotometer can use this principle to quantify the analytes in a sample based on their absorption characteristics [60][64]. This technique was used mainly for concentration determination of stabilized stock solutions in mucin vesicles [65], [66]. One of the most important consequences of the use of this technique is, as mentioned above, c the concentration determination of the substances. The way to do so, is by means of calibration curves when measuring many concentrations and their absorption (see Figure 3.4). It is important to try and create a linear relation between concentration and absorbance by starting from a very dilute solution and gradually increase the concentration or vice versa. It is suggested not to use very concentrated solutions (the concentration should not exceed the threshold of 0.001-0.01 mol/L) because then the interactions in the solution dominate between the solvent molecules and the absorbing species.

3.3 Zeta Potential Tests

The ZetaSizer-Nano ZS from MALVERN Analytical Instruments (UK) was used to perform zeta-potential measurements. What is referred to as zeta-potential, is actually the electrical charge of particles that are suspended in a liquid dispersant medium (see Figure 3.5). It can be used to describe double-layer properties of a colloidal dispersion [67]. The electrochemical potential is measured in mV. For colloids is considered as the electrical potential difference across the ionic layer around a charged colloidal ion. A system is considered stable for values less than -37mV or larger than +35mV. Values varying from +15mV to -15mV set the limit is where agglomeration starts , whereas a

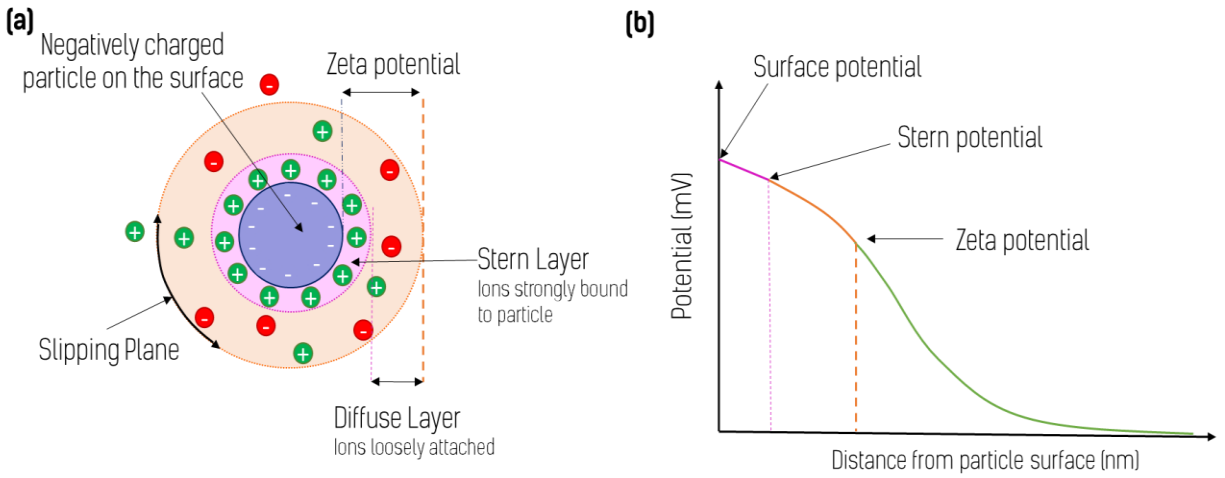

Figure 3.5: Schematic diagram illustrating the surface potential, stern potential, and zeta potential as a function of distance of a negatively charged particle in a dispersion medium. The different zones are color-coded.

value of 0mV states that the attractions between particles are strong enough for precipitation to occurs and lead to phase separation. Moreover, nanoparticles with a zeta potential between −10 and +10 mV are almost neutral whereas particles with values greater than +30 mV or smaller than −30 mV are considered strongly cationic or strongly anionic respectively [68]. In general, the ζ-potential cannot be measured directly, instead, it needs to be calculated from theoretical models or estimated experimentally usually based on electrophoretic mobility. The latter is indeed the method used by the Malvern ZetaSizer. In a nutshell, the instrument tracks the rate at which a charged particle moves in response to an electric field. The rate of migration from one electrode to the other is proportional to its ζ-potential, based on Smulochowski's theory [69], which is valid for any concentration or shape of the dispersed particles (since it assumes a sufficiently thin double layer, it ignores any contribution of surface conductivity).

3.4 Rheology

In nature there are two main types of materials, solids and liquids, with the former being purely elastic and the latter purely viscous. Elastic materials are characterized by Hooke's law: $\sigma=G\gamma$ and viscous materials by Newton's law: $\sigma=\eta\dot{\gamma}$ where σ is the shear

stress, γ the shear deformation, G the shear modulus (related to stiffness), $\dot{\gamma}$ the deformation rate and η the shear viscosity (resistance to flow). However, the majority of materials, e.g., those used in our daily life (i.e. ketchup, toothpaste, honey), are somewhere in the middle, i.e., viscoelastic, combining the elastic properties of a solid and the viscous ones of a liquid. Rheology is the science of deformation and flow of materials. There are two types of rheometric flows,[70], [71] (i) shear flow, where the imposed velocity gradient is perpendicular to the flow direction and (ii) uniaxial extensional flow, where the velocity gradient along the flow direction.

3.4.1 Oscillatory Rheology

There are two types of commercially available rotational rheometers, strain-controlled and stress-controlled. Both measure rheological response but they differ on the way of measuring. In this thesis, all measurements were performed with the stress-controlled rheometer MCR 501 of Anton Paar, Austria (Figure 3.6). Imagine a sample being sheared while sandwiched between two plates, with only the upper moving at constant (oscillatory) rotation speed. The signal coming from the instrument provides the strain γ. When operating in strain-controlled mode, the test is a controlled sinusoidal strain one, where the sine curve is determined on the amplitude and its oscillation frequency. The time-dependent strain applied is: $(t) = \gamma_o \sin(\omega t)$ and the corresponding measured stress is: $\sigma(t) = \sigma_o \sin(\omega t + \delta)$. For a purely elastic solid the applied

Figure 3.6: Anton Paar Modular Compact Rheometer (MCR) 501 (Austria).

sinusoidal deformation provides a stress which has no phase shift, δ=0°. For a purely viscous liquid the applied sinusoidal deformation has a shift of δ=90°. In the case of viscoelastic materials, the sine curves show a time lag between 0° and 90°. The complex shear modulus, $G^*=\sigma(t)/\gamma(t)$, describes the viscoelastic behavior of a sample. We can decompose it into two moduli, in-phase real and out-of-phase imaginary, G*= G' + iG". G' is called the storage modulus, represents the stored deformation energy and describes the solid-state behavior of the sample. On the other hand, G" is called loss modulus, representing the energy lost (dissipated) through (viscous) friction when flowing and describes the liquid-state of the sample. Tests performed typically are (i) dynamic strain sweeps (DSS), to determine the upper limit of the non-destructive deformation or else limit of viscoelastic region (LVE, typically occurring at small strain amplitudes); (ii) dynamic frequency sweeps (DFS), to describe the spectrum of behavior of a material in the LVE region, since high frequencies simulate fast motion on short timescale, whilst low frequencies simulate slow motion at long timescales; and (iii) dynamic time sweeps (DTS), to evaluate time-dependent viscoelastic behavior under constant strain and frequency (Figure 3.7). Moreover, long-time creep experiments were performed in order to extend the linear viscoelastic regime to lower frequencies.

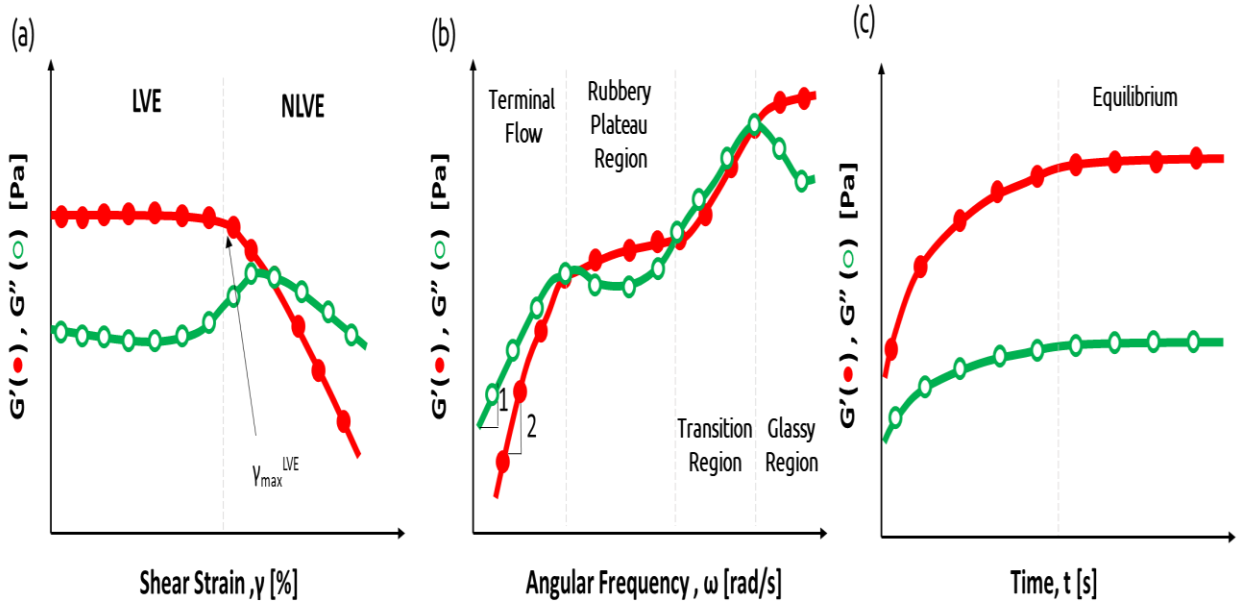

Figure 3.7: Indicative oscillatory shear rheological tests (a) Dynamic Strain Sweep; determination of LVE region (b) Dynamic Frequency Sweep; study of the flow properties over different time scales (c) Dynamic Time Sweep; time dependent behavior of the material. The insets in each graph highlight the main information we get from each test. Loss modulus (G") is symbolized with green line and open symbols, Storage modulus (G') is symbolized with a red line and closed symbols. All graphs are log-log representations.

The creep compliance J (t) was collected and analyzed as described by R.M.L. Evans *et al.*, [72]. All tests were executed with a cone-plate geometry of 50 mm, cone angle θ= 1° and a 0.102 μm gap.

3.4.2 Capillary Break-up Extensional Rheology

This method was the main rheological technique used for studying the stiffness mucin hydrogels and their composites. Due to the slippery nature of this system, the use of capillary break extensional rheometry by means of the HAAKE-CaBER1 (Thermo Scientfic, Germany) was rendered appropriate (Figure 3.8). With this technique, when a viscoelastic fluid is placed between two plates and stretched to a desired height, tension is applied (considered nearly uniaxial) and a capillary is formed, whose thinning to break is followed over time. There is an interplay of gravitational, viscous and interfacial forces and we assume that in the center of the capillary, after stretching, we have a purely uniaxial deformation up to the break-up point. We track the breakage of the capillary and in this way we collect information about the breakage time, the thinning profile of the filament and later on, while knowing the surface tension, we can extract a characteristic relaxation time and apparent extensional viscosity. The Caber instrument has a high precision laser micrometer to accurately track the thinning filament diameter profile, which computes the size of an object based on the intensity of light entering the sensing element. The output is the normalized diameter (D/D_1) which is tracked by the laser micrometer and plotted versus time until the break point (Fig. 3.9, Fig. 3.10). The plate motion is controlled by a linear motor. This system allows for fast response and reasonable

Figure 3. 8: CaBER HAAKE 1 by Thermo Fischer

control over the different stretch profiles used. The time needed for to stretch the sample is called strike time (t_S). An important parameter is the initial plate position determining the gap between the two plates. It is recommended to use an initial ratio $\Lambda_i=(2L_i/D_o)$ of 1 , i.e., if one uses a plate of diameter 6mm you, the choosen sample thickness (gap) should be 3 mm. If the initial gap is too large then the initial column of fluid is affected by the gravity and leads to erroneous final result. On the other hand the initial gap is too small, there is a strong dominating shear flow component from actually squeezing the sample and this affects the initial stretch and preconditions the flow profile. Also, the selection of the final gap plays also a role to the final stretch profile. For a better comparison, all different data sets should be based on the same final gap ratio (as much as possible). This gap ratio must be chosen such that it works for all samples, meaning that a capillary is formed, the instabilities are minimized and breakage takes place in a reasonable time frame. For the experiments presented in this

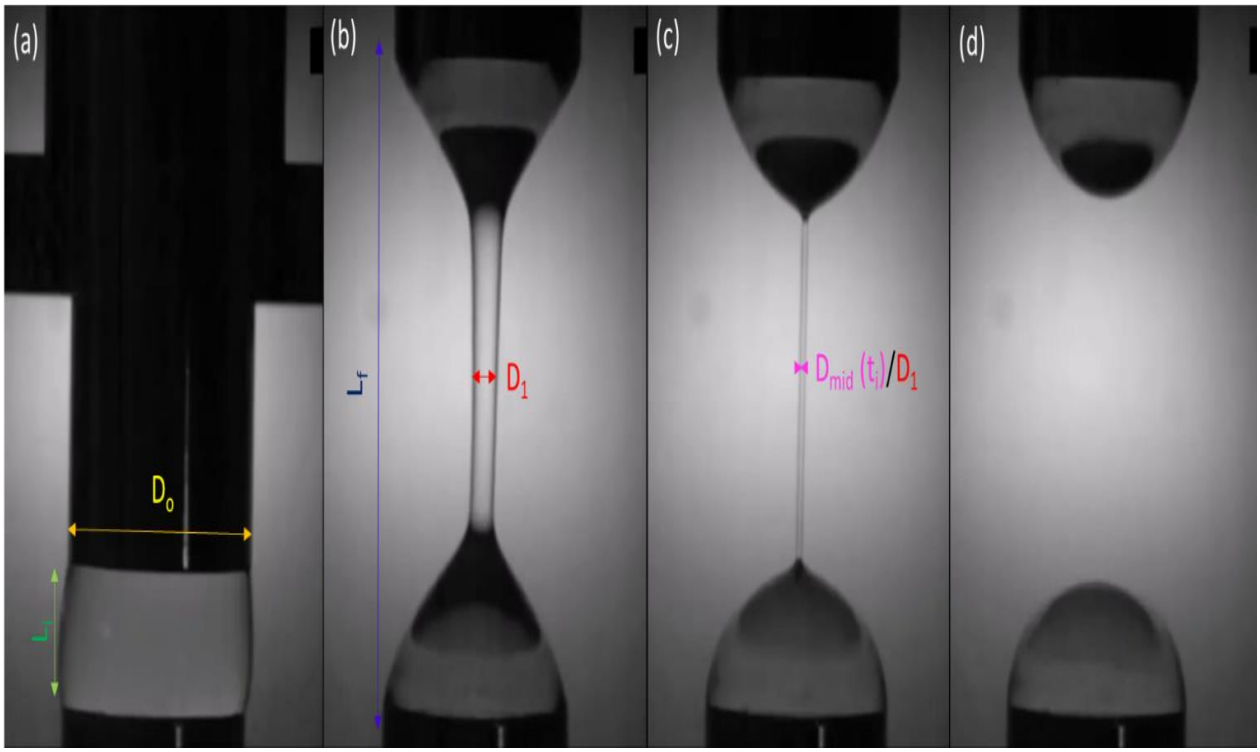

Figure 3.9: Images of the 3 main stages of a CaBER experiment. Right to Left: First, the initial position of the two plates with an ideal filament loading is shown. L_i is the gap between the two plates and is recommended to be $D_o/2$. In the next two photos, the measuring position right after the upper plate has reached its final position L_f and finally the last photo shows the breaking point of the capillary.

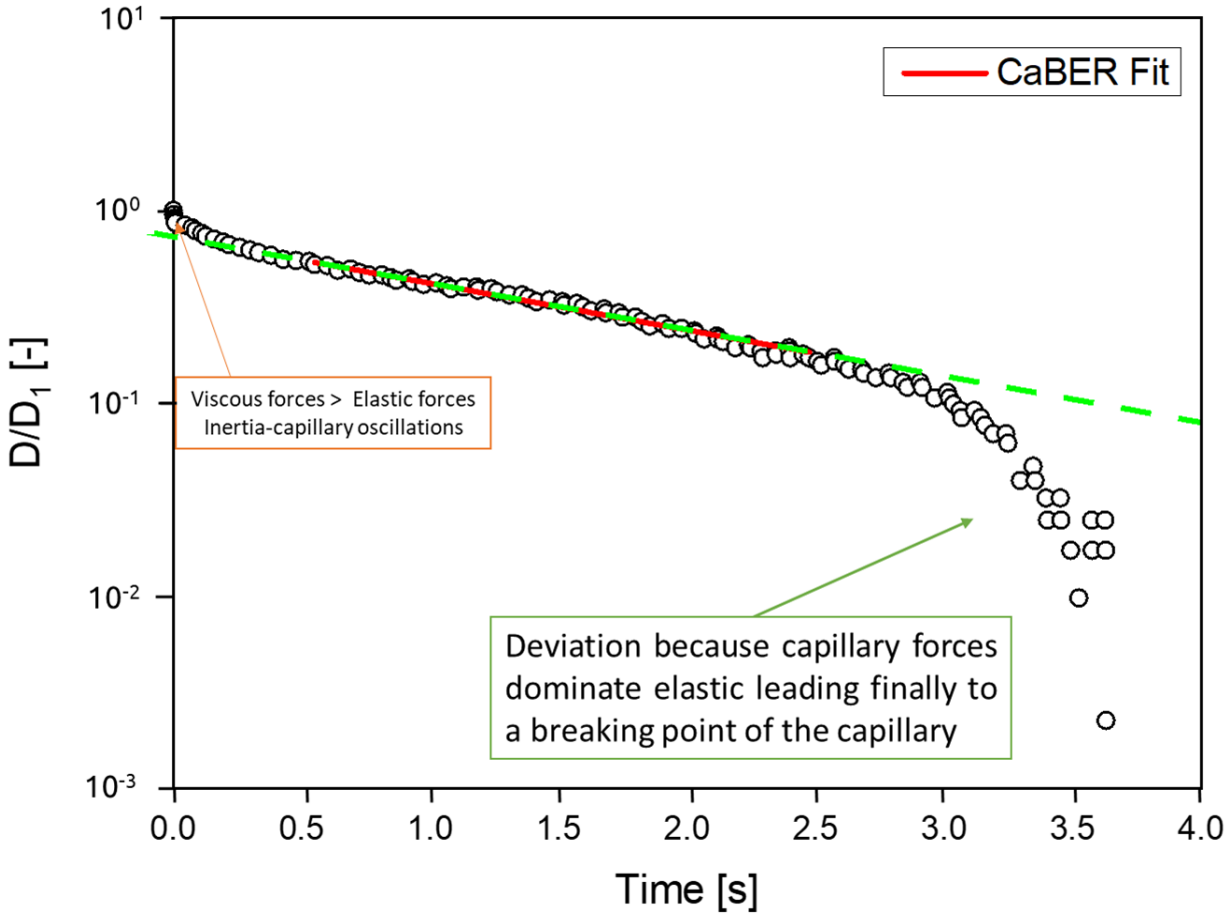

Figure 3.10: CaBER Data Analysis. Fitting with the viscoelastic equation 3.11 to extract apparent modulus G_{app} and relaxation time λ. The green dashed line is drawn to guide to the eye (it corresponds to a pure viscoelastic profile). The areas where deviation is observed are indicated with arrows and further explained in the insets.

work, a final gap of L_f ~ 11.48 mm was used, which corresponds to a ratio of $\Lambda_f=2L_f/D_o=3.56$. The upper plate reaches this final position by following a linear stretch profile, $L_f(t) = L_o \cdot t$ with a strike time of 50ms. Forces acting on the midpoint of the filament during initial stretching while the capillary is unbalanced and still developing, are surface-tension-driven, (which results in a flow away from the mid-point) and gravity-driven resulting to a flow from the top to the bottom plate. It is only after the filament gets thin and curved enough that the capillary forces are high enough that gravity has no influence on the system. Asides the gravitational phenomena, there are two other major issues while performing fast experiments. First, an instability associated with the formation of low-viscosity fluid droplets during breaking, known as beads-on-a-string (BOAS) effect [73], [74]. The second case is the strike time. If the

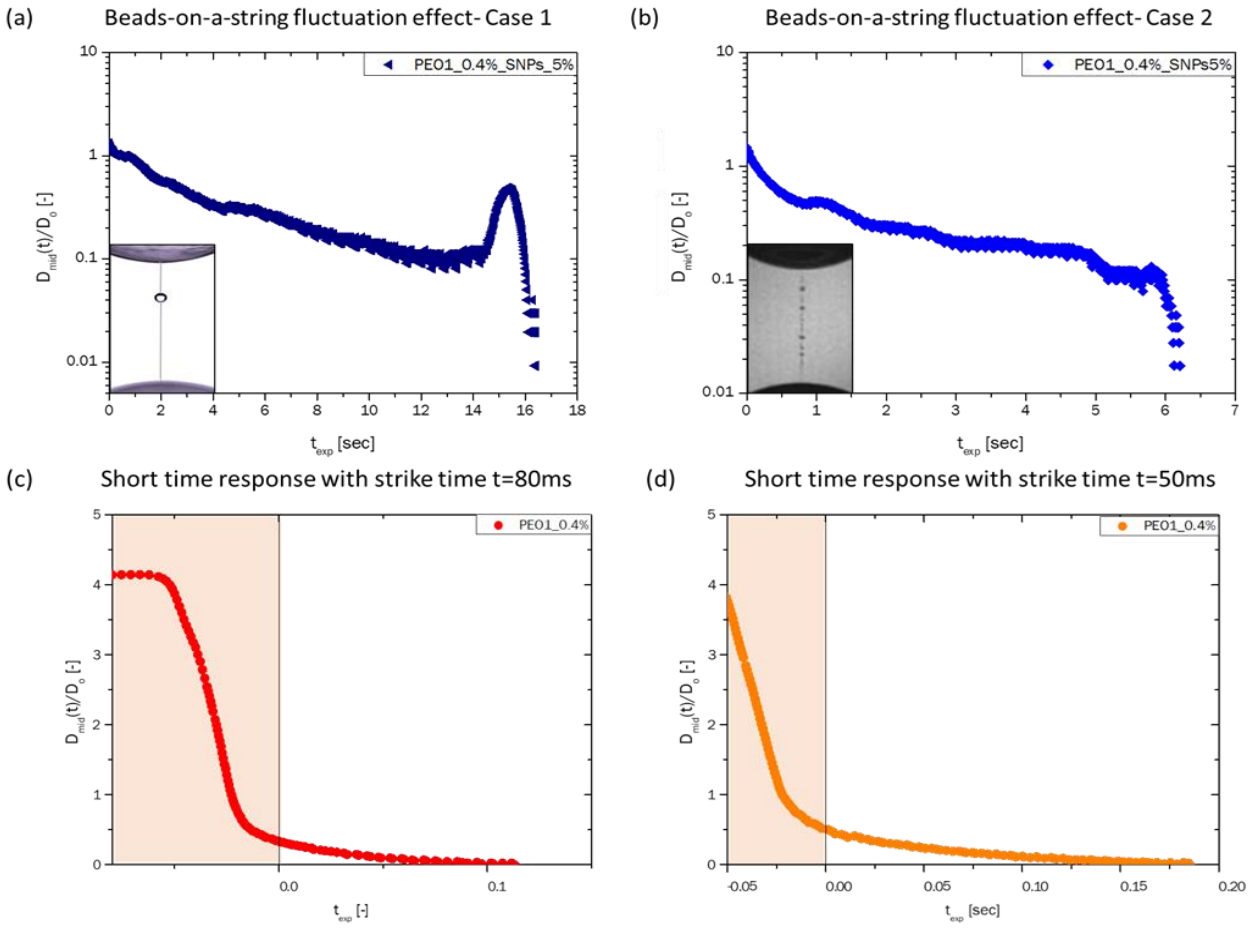

Figure 3.11: Graphical representation of common issues during fast Caber experiments. The upper set of graphs represents the BOAS instability, when the liquid filament breaks into droplets. Two different cases are shown: (a) the normal case where a capillary finally forms a single bead before it breaks; (b) BOAS effect where the entire capillary is divided into beads of different sizes, called generations. In the insets of (a) and (b) picture photo of each case is shown. In the bottom set of graphs an artifact of the instrument during fast tracking is shown: due to the long strike time an exponential decay takes place before the start to the actual experimental measurement, i.e., capillary thinning occurs during the (slow) stretching process. When strike times from 20ms to 80ms were tried this behavior was encountered. (c) Strike time 80ms (d) Strike time 50ms.

strike time is too long for your sample, the capillary starts the thinning process before reaching final position. Experimental results of these two problems are shown in Figure 3.11. Detailed analysis of the time evolution of the midpoint diameter of an elastic fluid can be described by the following equation 3.11:

$$\frac{D_{mid}(t)}{D_1} = \left(\frac{G_{app} \cdot D_1}{4 \cdot \sigma}\right)^{1/3} e^{-t/3\lambda} \tag{3.11}$$

Where D_{mid} (t)/D_1, is the normalized diameter evolution, G_{app} the apparent elastic modulus, σ the surface tension of the sample and λ the characteristic relaxation time. It is possible to extract λ and G_{app} by directly fitting equation 3.11 (see Figure 3.10) to the data. Moreover, an apparent extensional viscosity, η_{app} can be calculated through equation 3.12:

$$\eta_{app}(\dot{\varepsilon}) = \frac{\sigma \cdot R_{mid}}{\dot{\varepsilon}} = \frac{-\sigma}{dD_{mid}(t)/dt} \tag{3.12}$$

The Hencky strain ε (t) experienced by the fluid element at the axial mid-plane at time t can be defined using the mid-filament diameter, in equation 3.13:

$$\varepsilon(t) = -2\ln(\frac{D_{mid}(t)}{D_o}) \tag{3.13}$$

CHAPTER 4: MATERIALS

This chapter discusses the materials used in this thesis. They are (i) Telechelic Star Polymers (TSPs) comprising diblock copolymer arms and (ii) a biological hydrogel of mucin-like glycoproteins originating from hagfish slime. First we describe the synthesis and sample preparation of the TSPs. Subsequently, we present the biology of hagfish slime with special emphasis on mucin-like glycoprotein, the sample preparation protocol and also the characterization of the various additives used for trying to reinforce the hagfish mucin network. We also describe the procedure followed for determining the concentration of such protein solutions.

4.1 Telechelic Star Polymers (TSPs)

4.1.1 Synthesis

Telechelic star polymers (TSPs) are star polymers with ionic groups at the chain ends, thus attractive end arm sites [25],[26]. TSPs consist of f –AB-block copolymer arms grafted on a common center through state-of-the-art synthesis methods, in our case anionic polymerization. Star diblock copolymers with 3, arms of styrene and butadiene 1, 4 blocks and with 6 and 16 arms of styrene and isoprene blocks have been synthesized and used in this thesis (see Figure 4.1). High-vacuum anionic synthesis was employed with sec-Butyllithium (1.1 mmol) as initiator and benzene (C_6H_6) as solvent. In order to create polymeric stars comprising diblock-copolymer arms was used the grafting-to method. A detailed cartoon of the synthesis is presented in Figure 4.1 for the preparation of a 3-arm Telechelic star polymer. All samples were synthesized in the Polymer Synthesis Lab of Professor N. Hadjichristidis at KAUST, Saudi Arabia. The TSPs used and their main characteristics are listed in Table 4.1.

Table 4.1 : Molecular characteristics of investigated star diblock copolymers

Name	Sample[1]	f (arms)	Mw^{arm} (g/mol)	Mw^{star} (g/mol)	a(PS)[2]	a(PI)/(PB)[2]
f3-N2	(**PS**-b-PB)$_3$-2	3	8,800	26,700	0.23	0.77
f3-N4	(**PS**-b-PB)$_3$-4	3	13,000	40,500	0.14	0.86
f3-N6	(**PS**-b-PB)$_3$-6	3	13,000	40,000	0.33	0.67
f6-inv	(**PI**-b-PS)$_6$	6	45,000	270,000	0.49	0.51
f16-inv	(**PI**-b-PS)$_{16}$	16	51,000	816,000	0.50	0.50
f16-S1	(**PS**-b-PI)$_{16}$	16	55,300	835,200	0.49	0.51
f16-S2	(**PS**-b-PI)$_{16}$	16	65,800	996,400	0.25	0.75

[1]Bold are indicative of the outer block.
[2] Mass fraction was calculated via ^{1}H-NMR spectroscopy in $CDCl_3$ at 25 °C

Polymer star synthesis method : Grafting-to

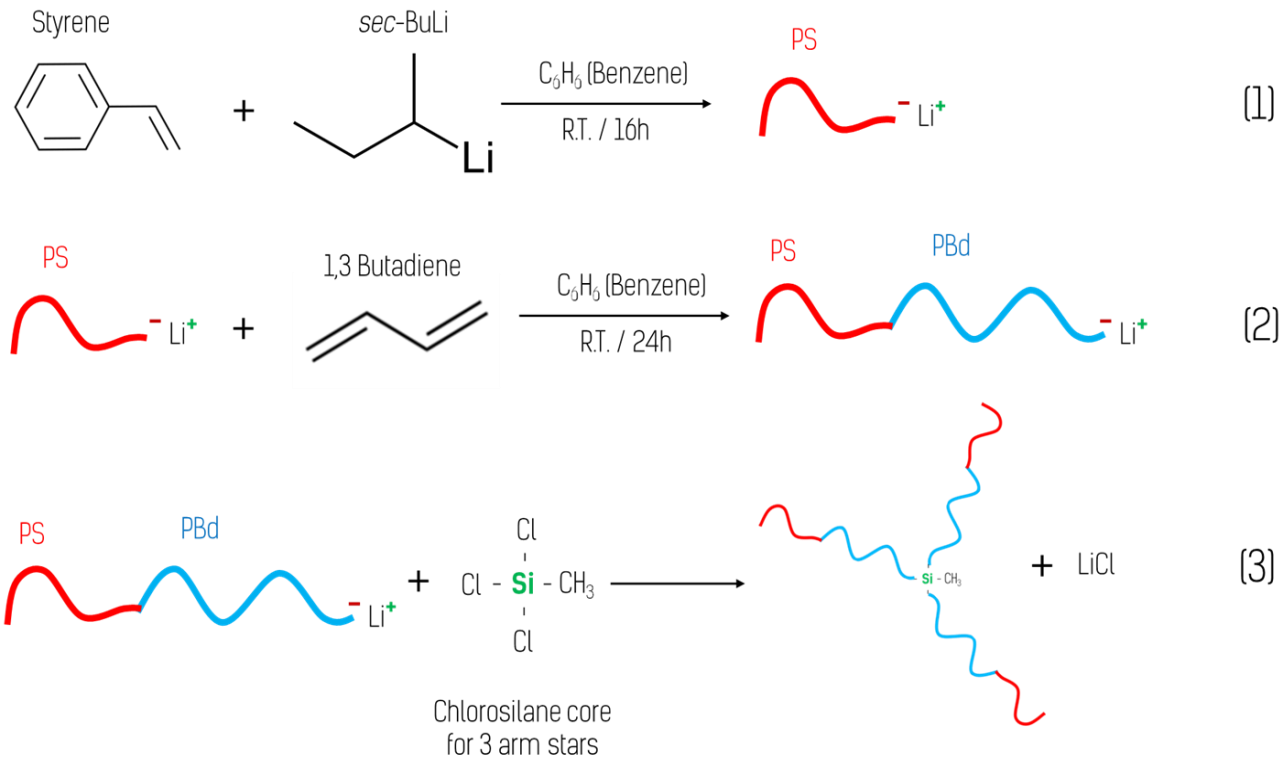

Figure 4.1: Synthesis steps for 3-arm star diblock copolymers (PS-b-PBd) $_3$. The process is divided in three main steps. First is the initiation step where sec-Buli is used as initiator and styrene as the monomer for the synthesis of the first (outer) block. Next, 1, 3 butadiene is introduced and the polymerization continues so the second (inner) block with an active end group is created. Finally, the arms are attached onto chlorosilane cores and 3-arm star diblock-co-polymers are produced.

4.1.2 Sample preparation for light scattering (LS) tests

In order to perform reliable light scattering experiments and extract high quality data we have to be very cautious while preparing samples. Is very important for the sample not to be turbid, not to absorb at the specific wavelength of the laser light source and not have a matching refractive index with the dispersant. Before use, all samples were stored in a deep freezer (T=-60^{o}C) to reduce the risk of degradation In order to ensure that the samples were fully dissolved in solvent 1-phenyldodecane, volatile dichloromethane co-solvent was used. Cresol® antioxidant was added at ~0.1%wt. Before transferring to a LS measuring cell, a sample was let at least 24 hours to ensure homogeneity. The cleaning procedure involved washouts using acetone with a filter of 0.45μm at least five times. Next, we used aluminum foil to cover the top of the cell and placed it in a vacuum chamber for approximately 20 minutes in order to be fully dried. Next, we added the sample into the LS cell by using a clean syringe and 0.45 μm hydrophobic filter. It is very important to prepare dust-free samples since dust particles are large in size (μm scale) and scatter a lot, ruining the quality of our data collection. Finally, the cell was loosely sealed with foil and set aside to allow for the co-solvent to fully evaporate. Before each DLS experiment, the samples were equilibrated at T = 60°C, which is above the cloud point of the outer PS-block (~55°C), for 10 min to erase thermal history. Then, the sample was quenched to the desired temperature and equilibrated. The equilibration process was probed by measuring the ISF until it reached steady values over time (baseline). The duration of equilibration depended on the temperature and ranged from 10 min at T = 60 °C to 10 hours at T = 20 °C.

4.2 Hagfish Mucin Proteins and Additives

4.2.1 Exudate collection and stabilization

The Atlantic Hagfish was fished from Atlanterhavsparken in Ålesund's Fjords Norway, by NTNU aquarium's staff. Slime exudate sampling was performed under the ethical

specifications met by Forsøksdyrutvalget (FOTS ID 6912) under the supervision of Møreforsking Nyhetsarkiv. The protocol followed by L. Böni *et al.* [38] is based on a protocol established by Herr and coworkers [75] which is described subsequently in more detail . The hagfishes were seized from about 80m depth using home-made built traps and then transferred to a vessel filled with seawater. Thereafter, they were anaesthetized in a mixture of 1:9 of clove bud oil (Sigma-Aldrich) and ethanol in a concentration of 1mL per 1 Lt of seawater. Following that, the hagfishes were washed quickly, placed on a dissection board dried and a mild electrical stimulation was performed close to the ventral pores with a stimulation device (HPG1, Velleman Instruments, 80 Hz, 8 -18 V) in order for the exudate to be released. The secreted exudate was collected with a spatula, stabilized in a high osmolarity citrate/PIPES (CP) buffer solution (mucin "stock" solutions) and stored straightaway at 4°C. The CP buffer comprised 0.1M PIPES (1, 4-Piperazinediethanesulfonic acid) from MERCK and 0.9M Sodium Citrate by SIGMA. For further enzymatic and bacterial stability 0.02%wt. sodium azide (NaN_3) and 0.02%wt. Sigmafast™ were added to a protein inhibitor cocktail by SIGMA. Finally, the fishes were transferred first to a recovery bath and finally back into the sea. It is important to mention that the high osmolarity buffer (CP) which contains polyvalent ions does not rupture the vesicles. Studies on vesicle membrane state that their membrane is impermeable to polyvalent ions [76].

4.2.2 Mucin-like glycoproteins isolation

Since we are interested in studying the mucin vesicles, it is important to isolate the two proteins after collecting the stabilized exudate. According to the literature [65], [75], [77], in order to achieve this the exudate is centrifuged at ~ 10.000-16,000 rpm for 10-5 min , respectively, at 10°C into 1.5 ml tubes. With this process samples are produced, which are separated into three distinct layers: the thread skeins, mucin vesicles and the natural supernatant of the slime, which is a clear fluid. After centrifugation, the natural supernatant from each sample was pipetted off using a micropipette and placed into clean Eppendorf tubes.

4.2.3 Slime sample preparation

I. Fast network formation via sloshing

To prepare hagfish slime from an already stabilized mucin vesicle stock solution, the quantities needed to be added (for efficient gelation) were based on an extended study discussed by Rementzi *et al.* [39], [66]. Mixing the original stock solutions with a micropipette was vital in order to ensure homogeneity and also re-disperse the vesicles in the CP buffer since they were settled at the bottom. After collecting the desired amount of mucin stock solution, Milli-Q was added and the mixture was sloshed gently 8 times for the majority of the mucin vesicles to open and allow for a fast network formation. The number 8 is an empirical albeit effective protocol for this kind of sample preparation. Note that sloshing is important to be gentle since even mild agitation may collapse the system by thread association, as shown in Figure 4.2 (b). This protocol is sensitive and user-dependent, while an uncertainty pertains to whether all mucin vesicles have opened-up. Hagfish gel produced in this way could not be studied by oscillatory shear rheology due to very low signal (discussed below).

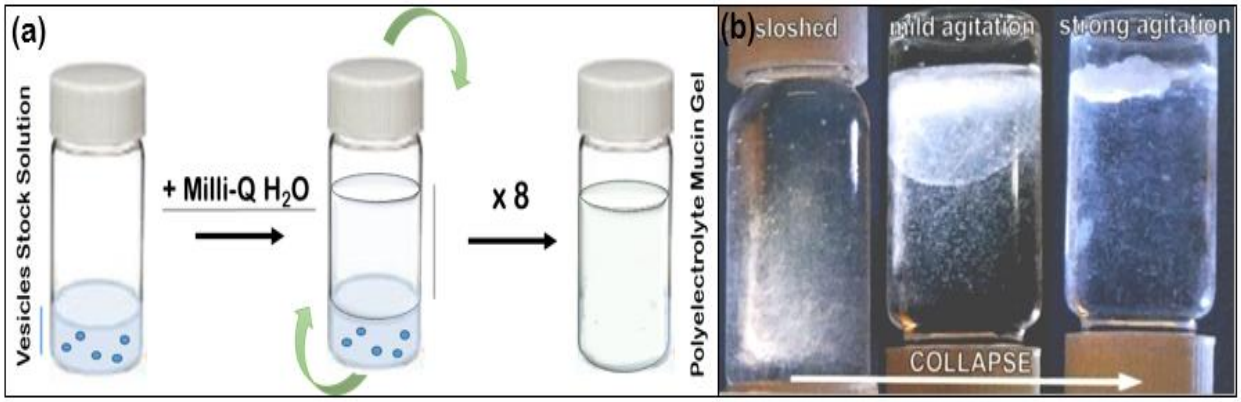

Figure 4.2: Fast hydrogel network formation by sloshing. (a) cartoon of the three-step formation process of forming the mucus gel via sloshing. Number 8 (times to slosh) is empirical but found to yield reliable samples. (b) Mucus gel can easily collapse if not handled gently. This photo is taken from L. Böni, PhD Thesis, 2018, ETH Zürich

II. Network formation via dialysis

An alternate protocol for forming a mucin protein gel involves dialysis. In order to prepare the samples were used 25kDa dialysis films were used, as well as two plastic clumps for sealing the dialysis tubes both at the top and bottom side. The first step is to close the one end of the membrane and then add a small quantity (~100-200 μL) of mucin batch stock solution, which needs to be gently mixed with a micropipette in order to be homogenized, and then seal the other end of the dialysis tube. Rinsing with excess of Nanopure water and placing it into a beaker filled with Nanopure water (~2L) is the next step and is followed by covering with aluminum foil and placing in the fridge (4°C). The dialysis process lasts 3 days and the water needs to be renewed at least 3 times per day. Each time one needs to change the Nanopure bath, rinse thoroughly both the beaker and the bag making sure one only touches the edges of the dialysis tube. Using this sample preparation protocol, it is possible to prepare comparatively large amounts of slime in a salt-free environment (ideally 0M). The sample after dialysis

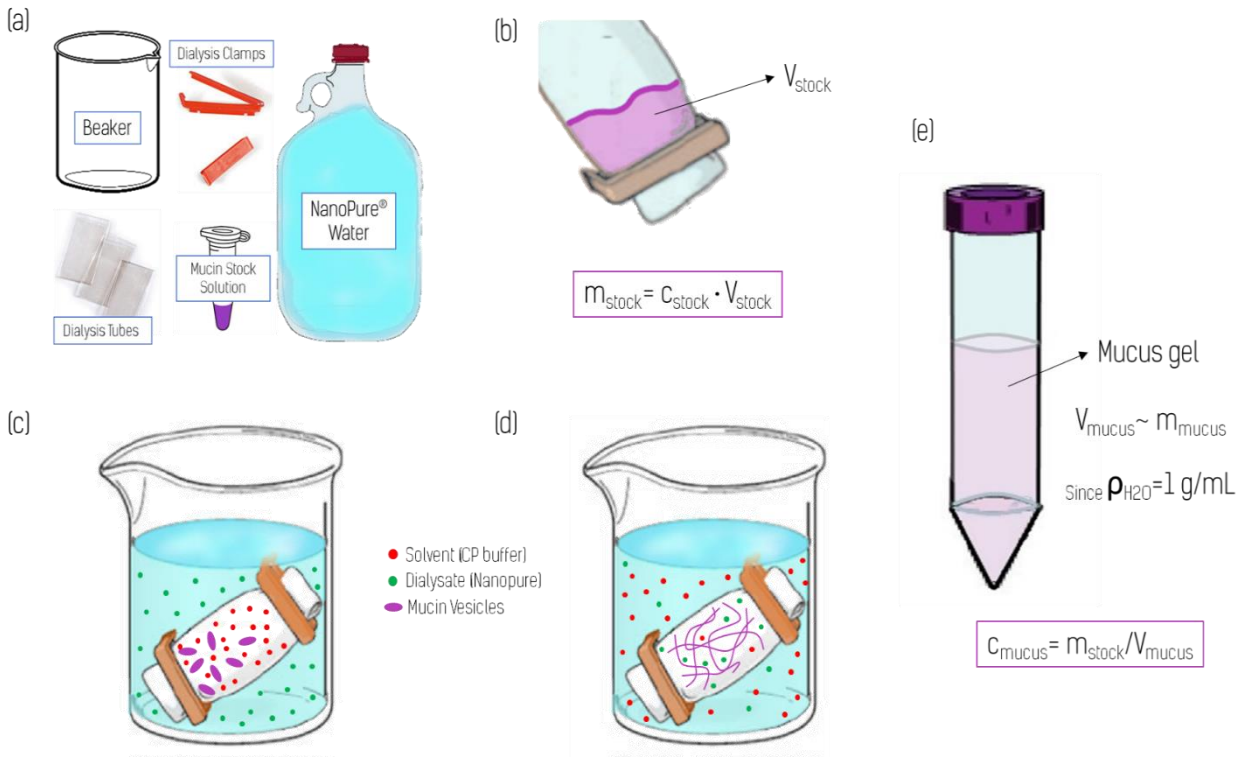

Figure 4.3: Schematic of the mucus network formation via dialysis protocol. (a) Equipment; (b) add stock; (c) start of dialysis (d) equilibrium state (vesicles swell and form network), a process performed multiple times; (e) when ready, we measure the mass and calculate concentration.

is released gently and placed in a new pre-weighted Eppendorf tube. This allows to estimate the water intake of the gel. This step was used for (approximately) estimating the concentration in mucin proteins forming a network. The following example explains the way to extract the final mucus concentration: We know that the mass of mucin and water equals the mass of the actual mucus. Let's assume that mucus mass is 1.0 g. Assuming further that its density is almost identical to that of water (1 g/ml) at room temperature, we estimate 1ml of mucus gel. If this final gel was originated from 100 µl of buffer solution with stabilized mucin vesicles introduced into the dialysis tube and the concentration of the stock solution was 15 mg/ml, then we can estimate the mass of mucin proteins. Hence, the final mucus concentration is 1.5 mg/1.0 ml =1.5 mg/ml. The preparation steps described above are illustrated in Figure 4.3.

4.2.4 Additives

I. Silica (SiO_2) Nanoparticles.

LUDOX®-TM50 from ALDRICH is a colloidal suspension of SNPs (average diameter stated in literature ~22-32 nm) dispersed in H_2O. Colloidal silica is an aqueous suspension of particle size less than 20 nm, formed by polymerization of silicic acid from dissolved SiO_2 and stabilized with Na^+. Silica nanoparticles have both anionic and cationic sites on their surface which leads to an unstable system if not stabilized properly. A schematic cartoon of a SiO_2 particle with particular focus on surface sites is shown in Figure 4.4. The samples used for characterizing the silica filler were 0.5%wt SNPs in 0.01 M CaCl2 and 0.5%wt SNPs in 0.01M in KCl [78] . The characterization study was performed with the Malvern ZetaSizer in order to obtain both their average size (d = 37.4 ± 8.7 nm; hence, quite polydisperse, about 25%) and zeta potential (-17.6 ± 1.2 mV). The ζ-value was is indicative of a system in the unstable regime. The pH for both

samples was ~7.5 which is also very close to the isoelectric point of the mucin proteins [38].

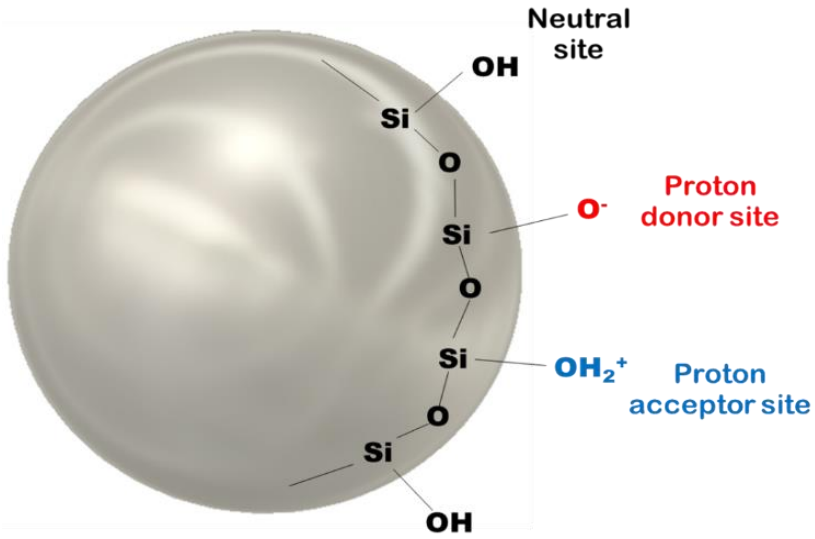

Figure 4.4: Silica nanoparticle. The active sites on the surface could be either (i) Neutral (-OH) (ii) Anionic or proton donor site (O^-) or (iii) Cationic or proton acceptor site ($-OH_2^+$). The final surface charge depends on the dispersed medium and the use of stabilizers.

II. Poly(Ethylene Oxide) (PEO)

Poly (Ethylene Oxide) from SIGMA-ALDRICH, PEO-1 Mw = 2,000,000 g/mol and PEO-2 Mw = 8,000,000 g/mol) was mainly used to confirm our studies on DNs. Both PEO powders were dissolved in Milli-Q and two aqueous solutions 2%wt. (with PEO-1) and 0.4%wt. (with PEO-2) were prepared. They were stored in the fridge and used as stock solutions. For the dissolution of the powders it was used a magnetic stirrer and they were stirred –not vigorously- until the solution was clear. PEO-1 solution was dissolved in about 72 hours

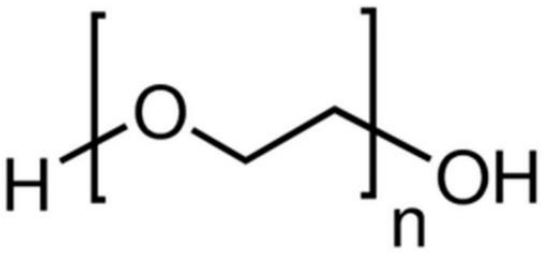

Figure 4.5: Chemical formula of PEO.

whereas PEO-2 in about a week since it has greater molecular weight. Its chemical backbone is shown in Figure 4.5.

III. Poly(Vinyl Alcohol) - (PVA)

Polyvinyl alcohol (PVA) is a semicrystalline, hydrophilic, linear synthetic polymer which is synthesized by hydrolyzing polyvinyl acetate [79], [80]. For our study we used a PVA from VWR Chemicals with Mw = 115,000 g/mol and a degree of hydrolysis of ≥88%. For commercial grade PVA, a common polydispersity index range is 2-2.5. PVA powder was dissolved in Milli-Q and an aqueous solution of 10%wt. was prepared and used as a stock solution. For sufficiently dissolving the PVA powder into water, it was necessary to raise the solution's temperature to ~70°C for 1 hour and then move to a cold plate while stirring at very low speed. Note that this is a very important step since PVA is a polymer that can form crystal regions which are undesirable. After about 72 hours the solution was clear enough and there was not sight of any flake or powder residue. The solution was sealed during the entire process to prevent water evaporation. The chemical formula of PVA is shown in Figure 4.6

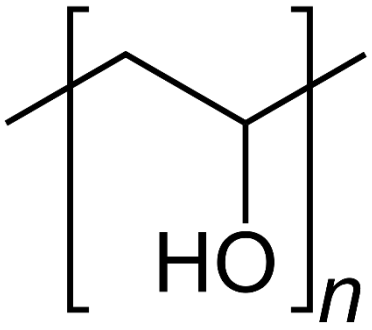

Figure 4.6 : Chemical formula of PVA

IV. CARBOPOL®

CARBOPOL®-ULTREZ 20 by Lubrizol, is a water-soluble polymer, used mainly as an emulsifying, stabilizing, suspending, thickening and gelling agent. CARBOPOL® belongs to the poly (acrylic acid) polymer family (Figure 4.7), however the exact chemical structure is not publically available. It is relatively easy to disperse in water because of its self-wetting properties. When dispersed it forms a microstructure that comprises swollen, elastic microsponge-like particles. A 10%wt. aqueous stock solution was made and stored in the fridge

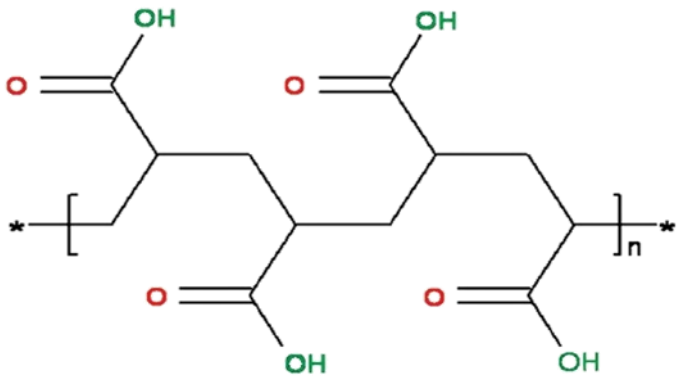

Figure 4.7: Chemical formula of Poly (acrylic) Acid. Based on literature, it is the backbone of the industrial CARBOPOL®-ULTREZ

(T=4°C). Once again, before introducing such particles to our system is important to know a relative size of the particles and of course the zeta potential value. CARBOPOL® solutions of various concentrations were measured with the Malvern ZetaSizer. The approximate values are d = 150 nm and z = -35 mV. Evidently, the polydispersity of the system is substantial.

V. Organosilica (MPTS) Nanoparticles

Thiolated organosilica (MPTS) nanoparticles, or else mucoadhesive nanoparticles, are used as fillers that can bind with special cites of the mucin matrix [81], [82]. For their synthesis , the protocol introduced by Irmukhavetova [81],[83] was used. In brief, 20ml of DMSO (SIGMA) were mixed with 0.5 mL of a 0.5M NaOH aqueous solution (made out of NaOH pellets from SIGMA). When fully dissolved, 0.75mL of 3- Mercaptopropyltrimethoxysilane (MPTS) by Alfa Aesar were added. The mixture was continuously stirred and ventilated for 24h at room temperature. The presence of oxygen is vital for the formation of sulfur bridges (Figure 4.8a). Next, the nanoparticle suspension was dialyzed with Milli-Q water for 48hours (8 changes of 500mL Milli-Q). To this end, a dialysis membrane of 25kDa was used. Finally, the purified NPs suspension was stored in the fridge (T=4°C). Subsequent characterization revealed an average diameter of ~67 nm and a z-potential of about -50 mV, indicating a slightly repulsive yet stable suspension. All data collected are displayed in Figure 4.8

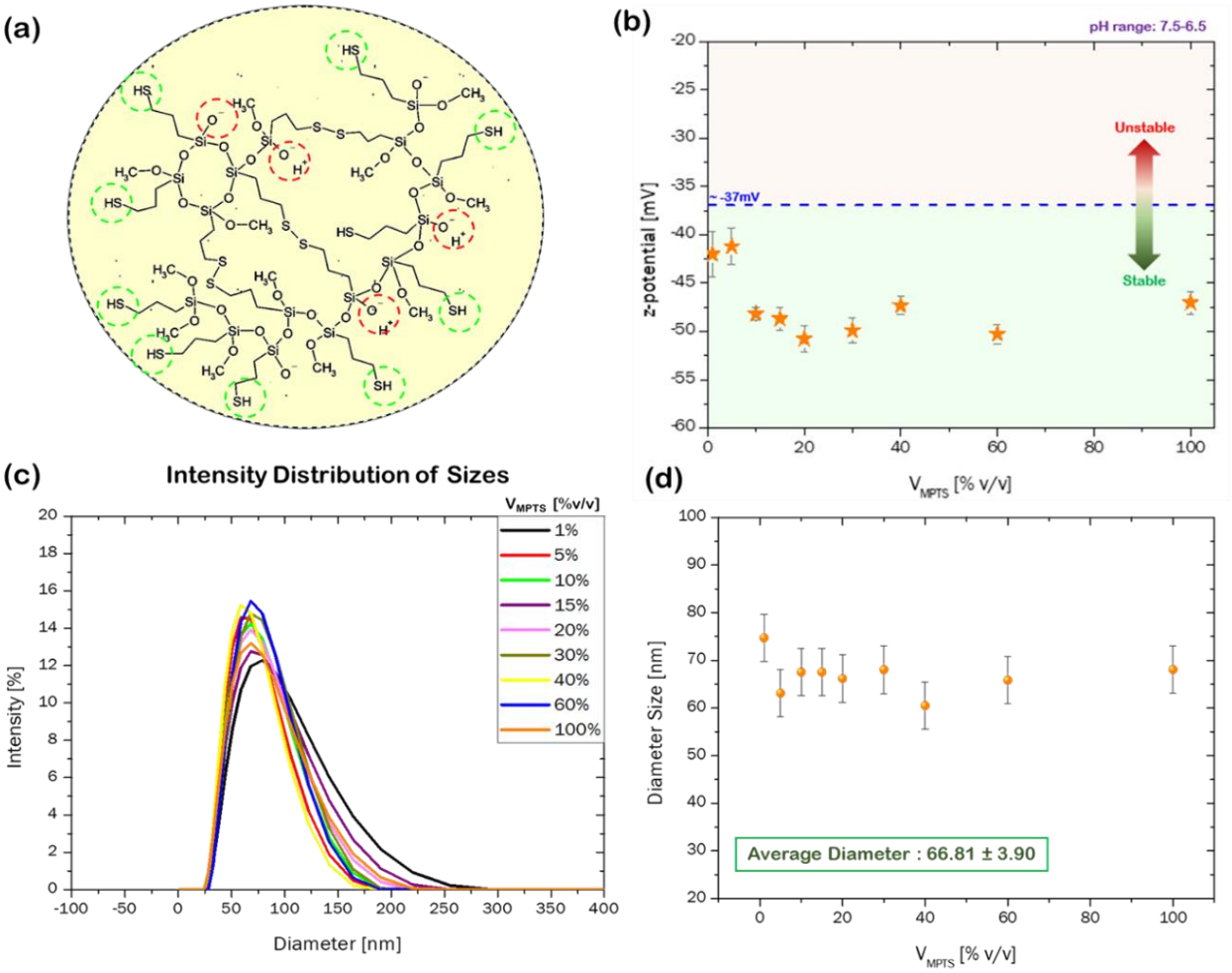

Figure 4.8: (a) MPTS Organosilica nanoparticle as sketched by Irmukhametova *et.al,* 2011. Circled with ▬ are the sulfide ends whereas with ▬ are highlighted some ionic sites that could cause destabilization. (b) Zeta-potential tests of the different samples. They are in the stable regime below -37mV. (c) Intensity Distribution of Sizes. (d) Size analysis.

4.3 Concentration of stabilized mucin stock solutions

Since we cannot have control over the amount of mucin vesicles for each sample it is important to determine the concentration of the mucin vesicles in each stock solution. For this reason, we used the concentration calibration curves proposed by Salo *et al.* [77] and later Zurflüh, Böni and Rementzi *et al.* [34], [66], [84]. These curves are constructed by collecting the value of each UV measurement with a sample that was subsequently freeze-dried in order to measure the dry mass of the vesicles. Indeed, we can correlate the outcome of the UV-Vis tests at a wavelength of 350nm with the concentration of the solution through some calibration curves [77], [84], [85] shown also in Figure 4.9. In order to determine the actual concentration, one has to start from a fixed concentration in volume and then either increase or decrease the concentration linearly. In our case we always started with a concentration of 1% v/v and then decreased it to 0.5% v/v, 0.25% v/v and 0.125%v/v. More specifically, we first collected 10μL of the stock solution, making sure that is well-mixed, and then added 990μL of CP buffer, reaching a total volume of 1 mL. Three different batches of each concentration

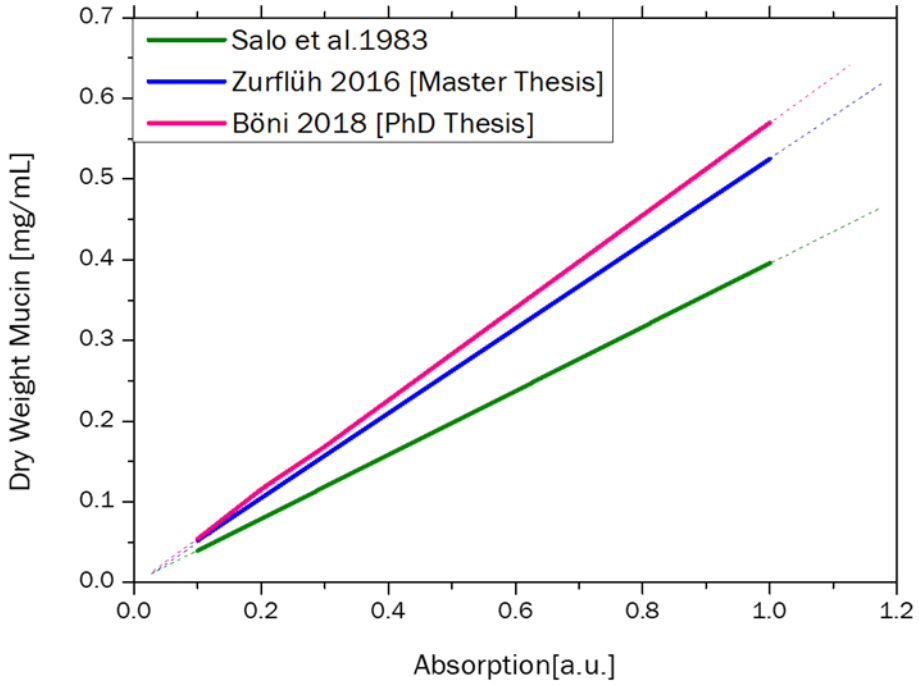

Figure 4.9: Correlation curves from UV-Vis absorption measurements at wavelength of 350 nm with the dry weight mucin for concentration determination in mucin vesicles of the stock solutions. Salo: y = 0.396x, Zurflüh: y = 0.525x, Böni: y = 0.573x-0.003.

were prepared and the UV-Vis tests were performed at least 3 times to acquire reliable statistics. Based on Zurflüh's study of a stock solution which we consider to be 100% [84] and by using equation 4.1 we can calculate the concentration in % v/v (c_{ref}):

$$y = 21.238x - 0.1528 \tag{4.1}$$

Where y is c_{ref} and x is for absorption of the corresponding concentration. Finally, this value is used to extract the concentration of the mucin vesicles by using equation 4.2:

$$c_{vesicles} = \frac{c_{ref}}{c_{meas}} \cdot 2.6(\frac{mg}{mL}) \tag{4.2}$$

Where $c_{vesicles}$ is the concentration of the vesicles in the stock solution, c_{ref} the concentration determined from the calibration curve and c_{meas} the concentration determined from the 2.6 mg/mL stock standard solution curve (pink line, introduced by Böni, presented in Figure 4.9). Table 4.2 lists the so-determined concentration of vesicles in the solutions.

Table 4.2: Mucin stock solutions and determined vesicles concentration determined through UV-Vis measurements analysis process.

Table 4.2	
Stock Solution	**$C_{vesicles}$ (mg/mL)**
S1	8.2
S2	2.6
S3	12.5
A	11.3

CHAPTER 5: SELF ORGANIZATION OF LOW FUNCTIONALITY TELECHELIC STAR POLYMERS IN DILUTE SOLUTION[1,2]

Telechelic star polymers (TSPs) are star polymers with ionic groups at the chain ends [25], [26]. They are consisted of f diblock copolymer arms grafted on a common center through state-of-the-art synthesis methods. Each diblock arm has a fraction α referring to the outer solvophobic monomers and (1-α) for the inner solvophilic. Hence, the arms of TSPs have a binary nature making them particularly sensitive to variations of the external conditions thus allowing each particle to self-assemble into a soft particle with attractive patches on its surface [86],[87]. In such a TSP system, is possible to cover the entire range of interactions, from purely repulsive to attractive soft colloids simply by changing the solvent quality. There has been put a great effort to understand their organization mechanism through experiments[88]–[90], but it is mainly by simulation analysis [90], [91],[92] . To explicate, in solutions, the attractions between outer blocks become stronger upon worsening solvent quality, i.e. upon lowering temperature below the cloud point of the outer B-block, in our case Polystyrene. This, consequently, leads to the formation of sticky ends. The self-aggregating behavior of TSP solutions is dependent on mainly three factors; the functionality (f) of the stars, the block size ratio (α), and the attraction strength between the outer solvophobic blocks enhanced upon worsening solvent quality. In this chapter, we first address the effect of attraction strength and following to that effect of the attractive block fraction on the self-organization of 3-arm Telechelic star polymers in dilute solutions.

First, we focus on the simplest possible system, stars comprising of three asymmetric block copolymer arms, with solvophilic inner and solvophobic outer blocks. We start off by explaining the change of the structure at the single polymer level upon cooling. In particular,

[1] This chapter is published as: E. Moghimi *et al.,* ''Self-Organization and Flow of Low-Functionality Telechelic Star Polymers with Varying Attraction'', *ACS Macro Lett*., vol. 8, no. 7, pp. 766–772, 2019.

[2] This chapter is published as: E. Moghimi *et al., "*The influence of arm composition on the self-assembly of low-functionality telechelic star polymers in dilute solutions," *Polym. Colloid Sci.*, 2020.

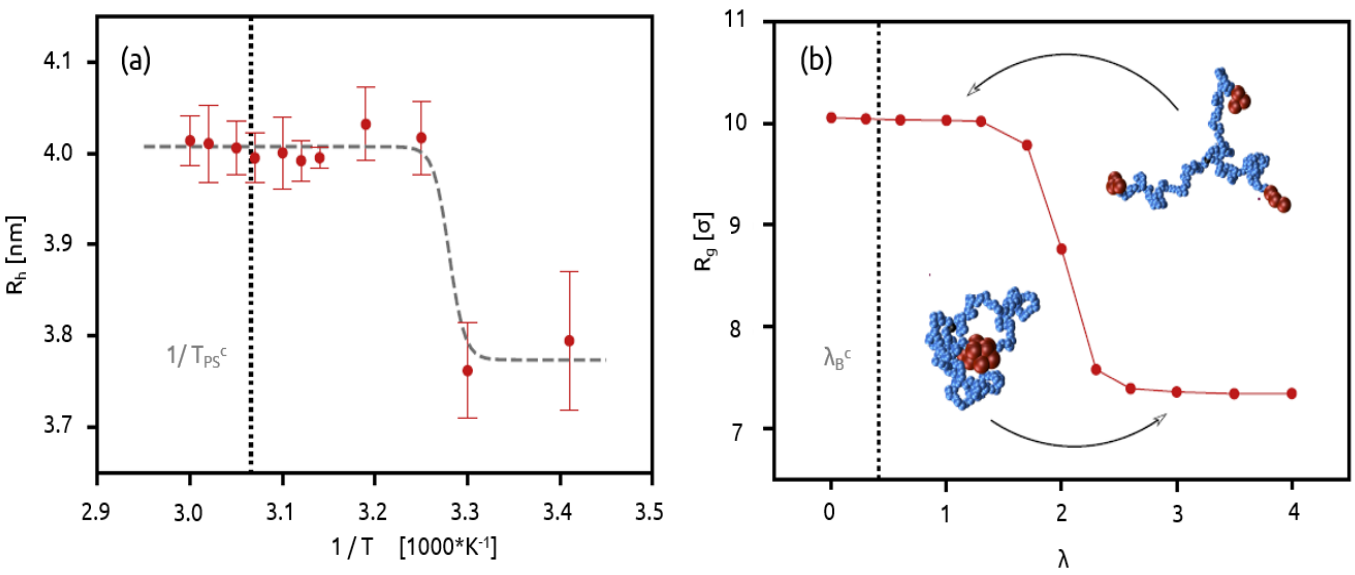

Figure 5.1: Comparison between single star properties in experiments and simulations. (a) Hydrodynamics radius, Rh, extracted from the fast process in ISFs at c = 0.7c*. The dashed line is a guide to the eye. (b) Radius of gyration of a single three-arm Telechelic star with NA = 65 and NB = 3 as a function of the attraction parameter, λ. Insets illustrate typical conformations of the TSP at corresponding values of λ. Dotted horizontal lines in (a) and (b) correspond to the cloud point of the outer block. DPD simulation analysis was carried out from Christos Likos group, Universität Wien.

we consider a dilute solution (c=0.07c*) of a TSP with f = 3 and α (PS) = 0.23 (f3-N2, see Table 4.1) at different temperatures. Fig.5.1a provides the hydrodynamics radius Rh associated with the fast process in the intermediate scattering functions (ISFs) in the dilute regime and calculated using the Stokes–Einstein-Sutherland relation, which effectively represents the size of a single freely moving molecule. As a direct comparison, in Fig.5.1b is shown the gyration radius of the star as obtained from DPD simulations at different values of the attraction coupling constant (λ). Remarkably, in both cases is observed a reduction of the molecule size upon cooling. Descriptive snapshots of the individual TSP before and after the shrinkage are given in Fig. 5.1(b) to further help visualizing and understanding the self-assembly process. When the B-monomers, colored in red, are in a good solvent (i.e. for small values of λ), the star is open and the attraction between star arms is negligible. Upon worsening the solvent quality, solvophobic monomers first start to form short-lived patches ($1 < \lambda < 2.5$) that can be easily destroyed by thermal fluctuations. This ultimately leads to the collapse of a whole TSP with f = 3 into a watermelon-like structure ($\lambda > 2.5$) leading to a significant characteristic decrease of the star's radius of gyration. The hydrodynamic radius of the single star, seems to follow the trend since it exhibits identical behavior upon cooling (size reduction for T below 30 °C) and is consistent with the self-assembly picture introduced above.

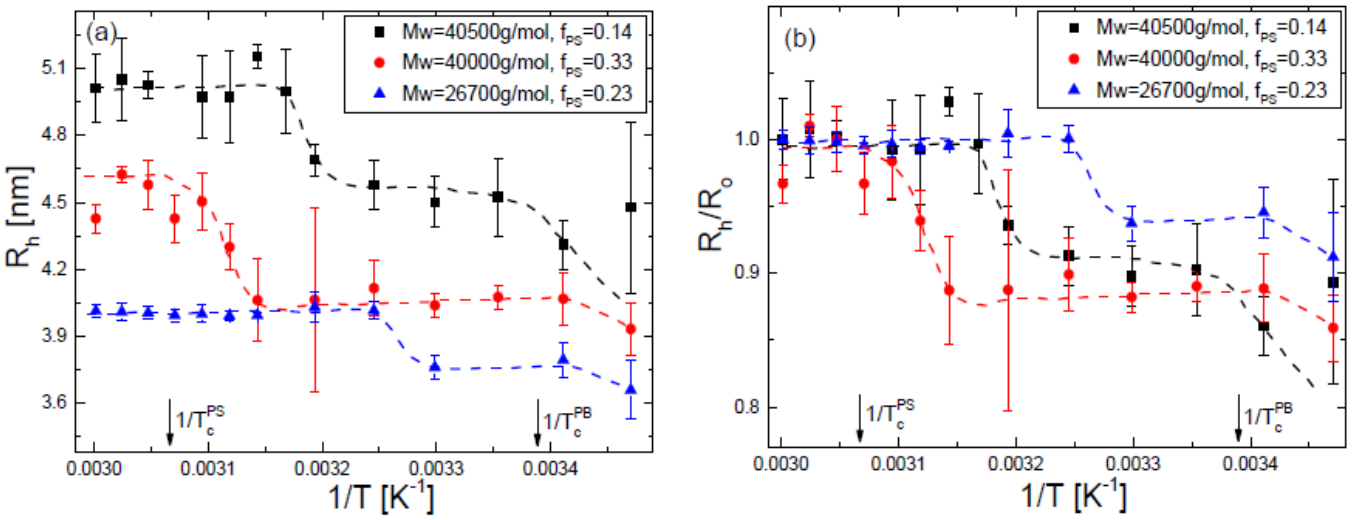

Figure 5.2: (a) the hydrodynamic radius, Rh, of individual TSPs in the dilute solution calculated from the fast process in the experimentally determined ISFs. (b), Rh normalized by its plateau value at high temperatures. The dashed lines serve as a guide to the eye. The black arrows indicate the cloud-points of inner PB and outer PS blocks.

Furthermore, a more detailed examination of Figure 5.1 reveals that both in experiments and simulations the decrease in size of a single TSP occurs within a narrow region of temperatures and attraction strength. The ability of simulations to describe the experimental findings reliably gives confidence in using them as the main tool for exploring the parameter space, which is otherwise inaccessible experimentally. Note that the radius of gyration was too small to be probed by DLS; hence, the comparison will be made between experimental R_h and simulated R_g. The former, R_h, is an apparent size of the TSP and it is often assumed that $R_h(T)/R_g(T)$ is a constant ratio; this is not strictly true because of the different origins of these quantities. Nevertheless, the existence of a transition temperature for the single TSP caused by interarm association is an apparent feature of both quantities. On that event, we then focus on how and if the fracture the outer PS-block has an effect on the dynamical relaxation of the system at low densities. For this reason we used as a model system the above-mentioned ,f3-N2, and studied dilute solutions of 3 arm TSPs of different PS fractions and molecular weight about 40,000 g/mol, f3-N4 with α(PS)=0.14 and α(PS)=0.33. More details about the systems are mentioned in Table 4.1. The single star hydrodynamic radius for all three systems are exhibited in Figure 5.2(a). One can see that despite the fact both TSPs have almost the same molecular weight, the difference in their size when in good solvent conditions, originates from the difference in the fraction of PS as explained in the following. The radius of gyration of a

star homopolymer in good solvent conditions is given by $R_g \approx \kappa(f) b N^{\nu}$, where ν=0.588, N is the number of Kuhn segments in a star, b is the size of a Kuhn segment, and $\kappa(f)$ which dependents on the number of arms, is a numeric constant that takes into account the star functionality. Using the latter relation it can be found that the size of a star made of purely PB is about 65% larger compared to that made of purely PS, $R_g^{PB} \approx 1.65\ R_g^{PS}$, given that their molecular weight is the same. Hence, it is expected that the increase in PS fraction reduces the size of a TSP. In order to safely compare the collapse for stars of different size, the TSP size was normalized by the plateau value of hydrodynamic radius at high temperatures. The TSP with a larger fraction of outer PS-blocks, α (PS) =0.33, shows the first-step reduction in size at higher temperatures and the second-step drop at slightly lower temperatures compared to the TSP with a smaller PS fraction, α (PS) =0.14 since we have a smaller incompatibility parameter in this case (χ_{PS}). However, in both stars the reduction in size is about 15% (see Figure 5.2(b)). Further insight, about their conformation when the outer B-block is in bad solvent was provided through particle dynamic simulation analysis by *C.* Likos *et al.* in Figure 5.3 , where we observe that a lower PS fraction leads to formation of smaller interpaticle patch which forms a less compact and less symmetrical particle [93]. In addition, in Figure 5.2 we show the results for a TSP with a smaller molecular weight (26,700 g/mol) with the outer PS-block fraction which is α (PS) = 0.23 between the other two aforementioned higher molecular weight TSPs. The main difference is that the TSP with the smaller molecular weight shows the decay in size at a much lower temperature compared to the other. Moreover, the decrease in size is also weaker, which could be attributed to the shorter length of its arms. In Figure 5.4, we show the experimental ISFs at a fixed wave vector, q=0.02475 nm^{-1}, and various

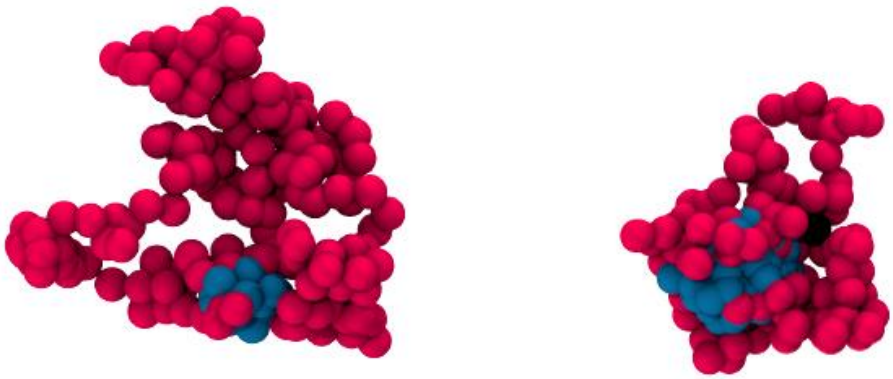

Figure 5.3: Characteristic TSP conformations with a= 0.1 (left) and a = 0.3 (right) at a high attraction strength. The simulated single stars have f = 3 arms of length N = 64 using a coarse-grained DPD model. B-monomers are blue, A –monomers are red, star centers are black. Solvent particles are not shown for clarity.

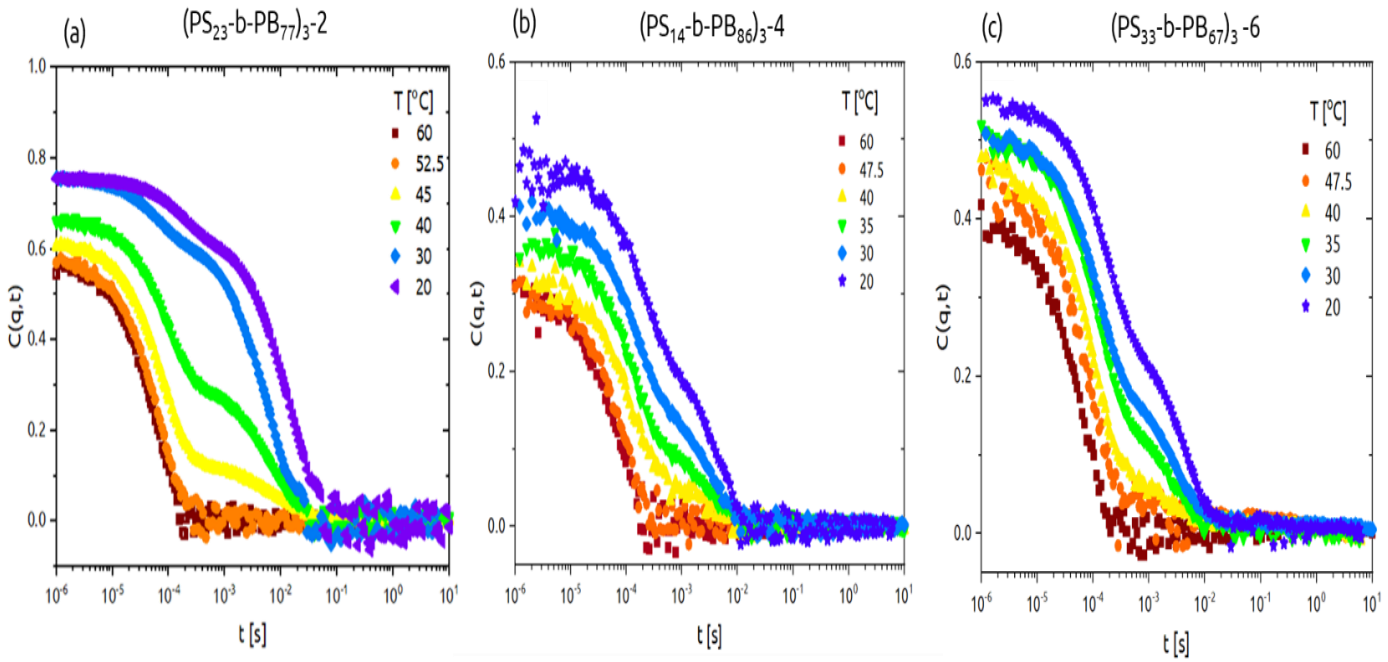

Figure 5.4: Experimental Intermediate Scattering Functions [g^2 (t)-1] upon increasing attraction strength via decreasing temperature for dilute solutions of 3-arm TSPs varying the outer PS block fraction (a) f3-N2: Mw = 26,700 g/mol , a (PS) =0.23 (b) f3-N4 : Mw= 40,500 g/mol a(PS)=0.14 , (b) f3-N6 : Mw=40,000 g/mol , a(PS)=0.33

temperatures for the three samples. The reason that all ISFs at short times is well-below one is due to the fact that a part of scattered intensity originates from density fluctuations associated to solvent molecules. If the scattered intensity was solely caused by TSPs, then ISF would start from one. The first correlogram, Fig 5.3(a), is for the one smaller molecular weight whereas 5.3(b) and 5.3(c) are the ISFs of the TSPs with comparable total

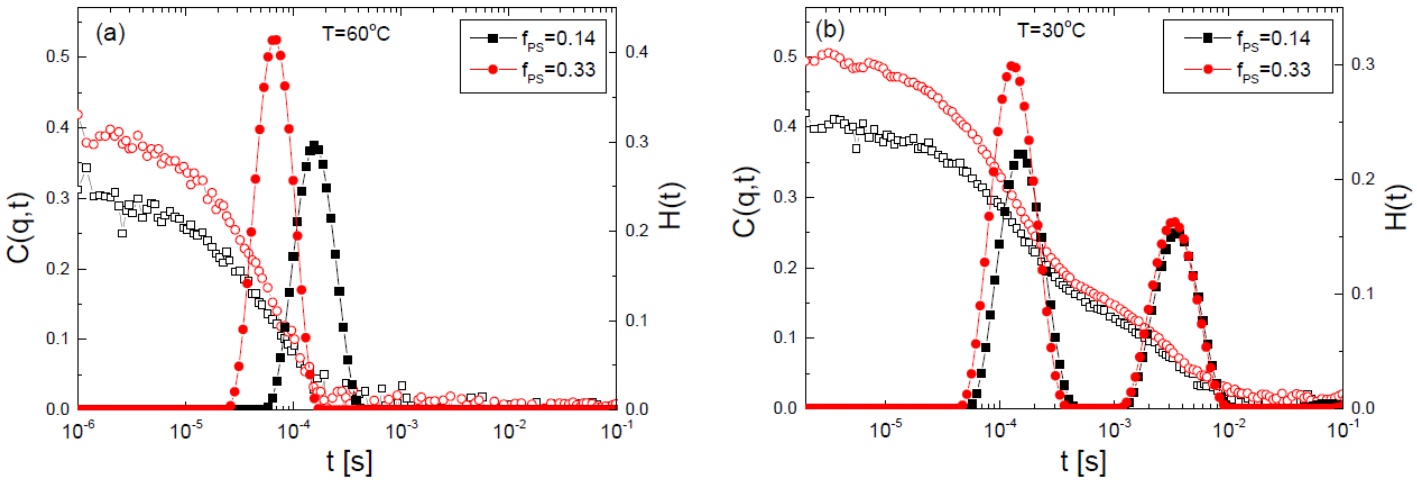

Figure 5.5: ISF (open symbols, left axis) and its corresponding relaxation times spectrum (closed symbols, right axis) deduced from the constrained regularization method for the TSPs with PS fractions of α (PS) = 0.14 (black squares) and 0.32 (red circles) at q = 0.02475 nm^{-1} for T = 60 °C (a) and T = 30 °C (b).

molecular weights but with distinct PS weight fractions. Despite that, the ISFs show two distinct trends upon changing temperature for all three cases. At high temperatures, the ISFs show a single exponential decay indicating the existence of individual stars in the solutions. However, when temperature is reduced below the θ-temperature of the outer-block, the ISF features a two-step decay which indicates the coexistence of two distinct populations in the system. The first decay (fast process) in the ISF is similar to the one observed at high temperatures and hence represents the individual stars in solution. On the other hand, the second decay (slow process) taking place at longer times suggests the presence of larger aggregates (clusters of TSPs). The slow process becomes more pronounced as temperature is decreased. The two-step relaxation of the dynamics indicates the coexistence of clusters (represented by a slow process) and single TSPs (fast process). The CONTIN analysis of ISFs exhibits two well-separated peaks in the relaxation spectrum, which represent the relaxation times of single stars and clusters. The corresponding relaxation times are used to calculate the diffusion coefficient and, subsequently, the hydrodynamic radius of a single TSP and clusters using the Stokes–Einstein-Sutherland relation the relaxation spectrum is calculated from the inverse Laplace transformation of the ISF using the constraint regularized method [43]. Typical results of such analysis for the TSPs with two different PS fractions at T = 60 °C and 30 °C are shown in Figure 5.5. The relaxation spectrum at 60 °C shows a single peak, which

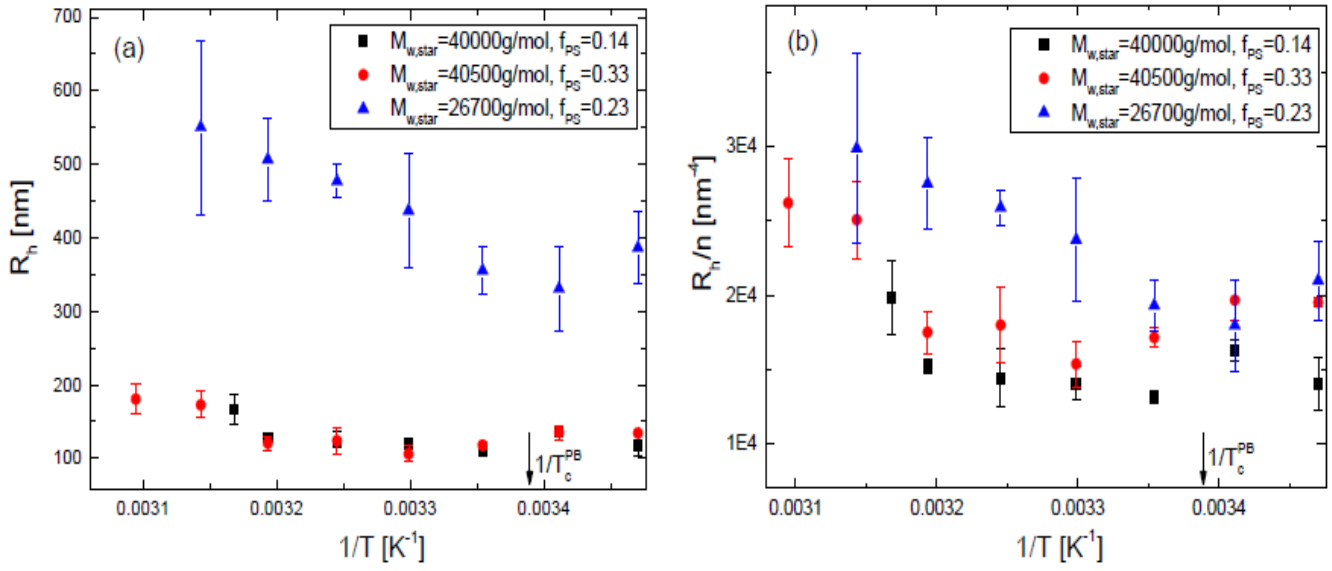

Figure 5.6: (a) The hydrodynamic radius, Rh, of clusters extracted from the slow process in the experimental ISFs. (b) The ratio of Rh to the number density n of TSPs in the solution. The black arrow indicates the cloud-point of inner PB blocks.

is rather sharp. In Figure 5.6, we present the temperature dependence of clusters' for the Rh systems of TSPs with the same molecular weight but two different PS fractions. In both TSPs, the cluster size shrinks on cooling. This we can explain as, for lower attraction strength the stars start organizing into micelles in a way that the solvophobic B-blocks assemble a micellar core and the A-block make a solvophilic corona. Upon decrease temperature this core becomes denser in order to expel the solvent molecules so we have actually less TSPs that can participate in a micelle. So we end up having smaller yet more micelles. Nevertheless, the interconnectivity between the different micelles is increasing in a way that they can start forming a percolated networkHowever, a slight but consistent increase in the cluster size is observed when temperature is further reduced below the cloud-point of the inner PB-block. Moreover, the hydrodynamic cluster size does not show change with the fraction of outer PS block. However, the smaller molecular weight TSP shows a cluster size that is nearly three times larger. This could be due to a higher concentration of TSPs. To rule out the effect of concentration, we have normalized the cluster size by the number density of TSPs in solution. The number density takes into account for the number of stickers available in the solution (see Figure 5.6b). With such normalization, the difference in cluster size between different TSPs are reduced to a great extent. The minor differences could originate from the complex nature of self-organization of TSPs due to differences in their molecular characteristics.

CHAPTER 6: DYNAMICS AND SELF-ASSEMBLY OF 16-ARM TELECHELIC STAR POLYMERS

TSPs with low functionality (f < 5) are known to collapse into a watermelon structures in dilute solution, with one single patch on the surface of the particle[86]. We provided experimental evidence for this in Chapter 5, by presenting data for various 3-arm TSPs. However, simulations suggests that when the number of d arms increases, more complex structures are

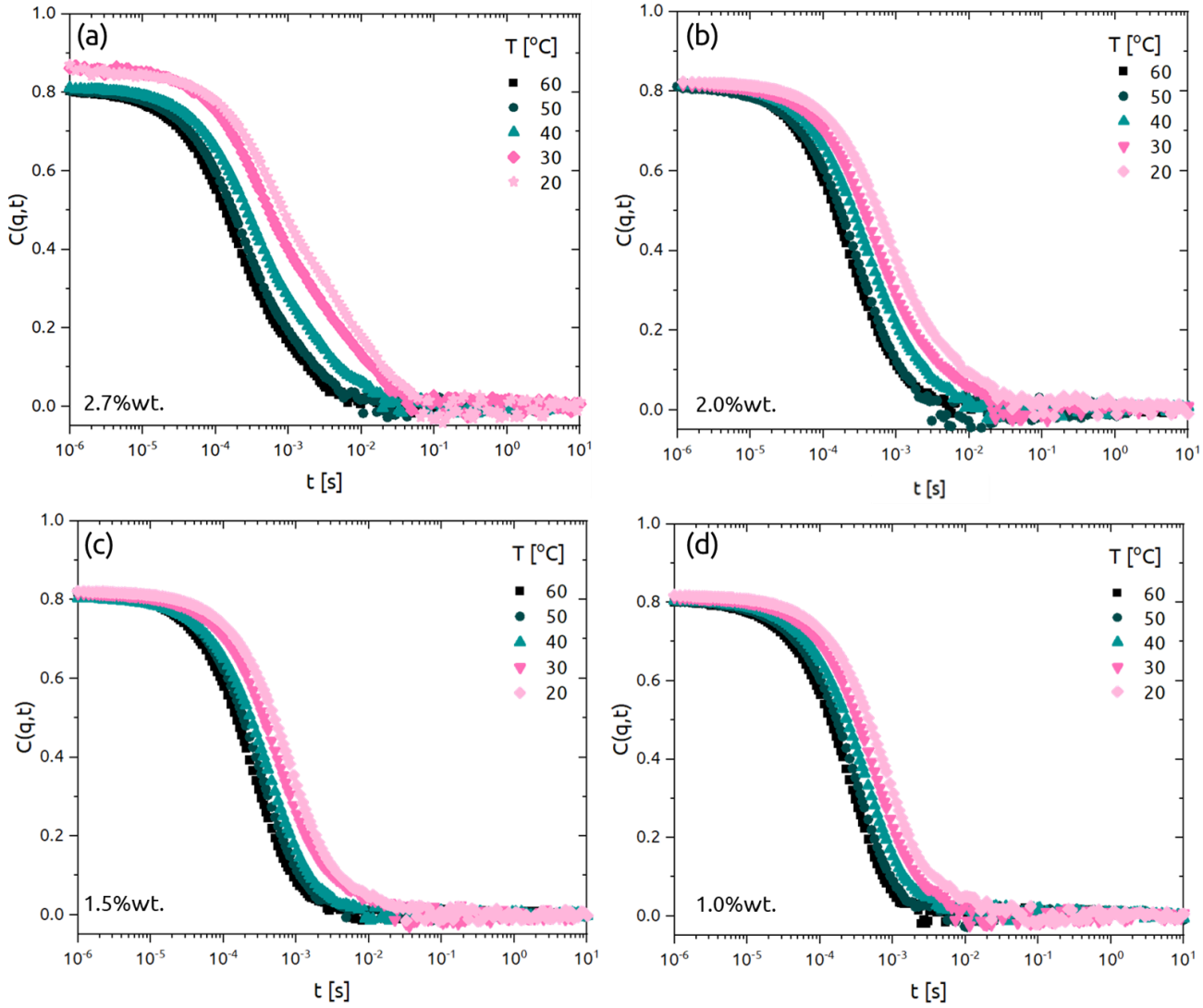

Figure 6.1: Experimental Intermediate Scattering Functions (ISFs) upon increasing attraction strength via decreasing temperature of the solutions of a 16-arm TSPs with α (PS) block fraction of 0.49 and M_w^{star}= 835,200 g/mol varying the %wt. concentration (a) 2.7%wt. (b) 2.0%wt. , (b) 1.5%wt. , (d) 1.0%wt.

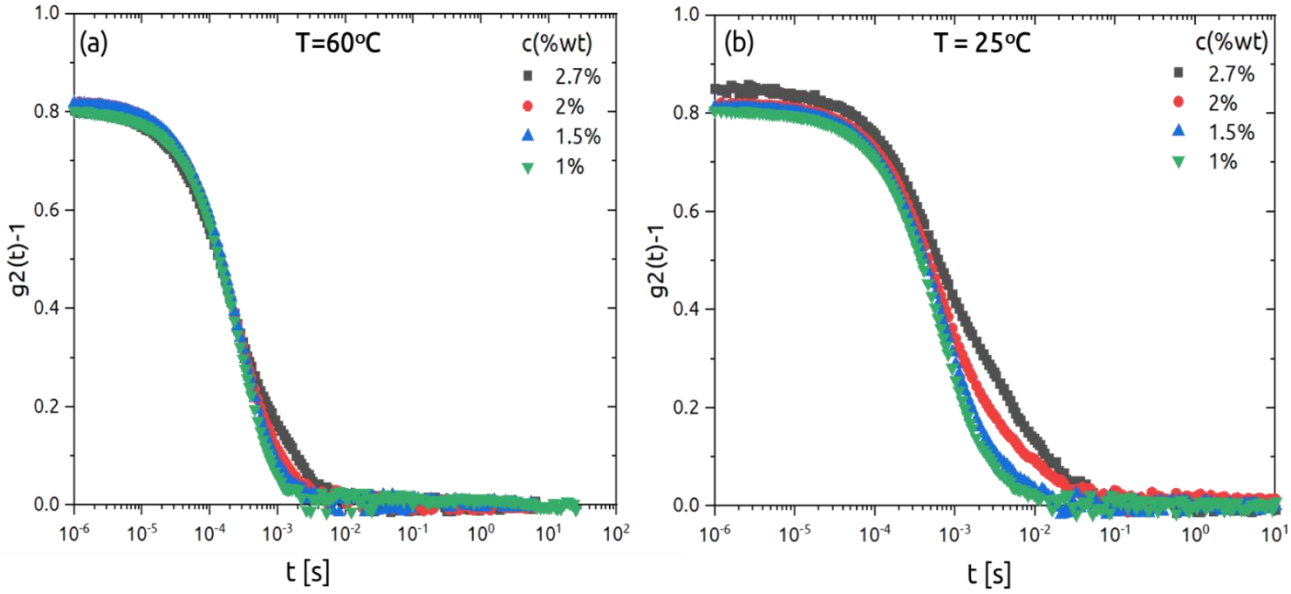

Figure 6.2 : Experimental Intermediate Scattering Functions (ISFs) at fixed wave vector upon increasing attraction strength via decreasing temperature for solutions of a 16-arm TSPs with α (PS) block fraction of 0.49 and Mw^{star}= 835,200 g/mol varying the %wt. concentration (a) T=60°C, athermal state for both A and B-monomers. (b) T=25°C, poor solvent for outer B-block.

formed [94]. TSPs self-assemble in different structures due to the competition between enthalpic attraction amongst the solvophobic tails of the f arms and the entropic self-avoid repulsion of the inner part. Concerning the role of f on the self-organization into different micellar aggregates, simulations reveal the formation of soft patchy particles with the number of patches depending on f and the strength of attraction fraction of solvophobic groups [95]. In this chapter we investigate two different 16-arm telechelic star polymers of relatively high M_w which vary their outer B-block fraction; (i) f16-S1 with α (PS)=0.49 and M_w^{star}=835,200 g/mol, (ii) f16-S2 with α(PS)=0.25 and M_w^{star}=996,400 g/mol. Details about the samples can be found in Table 4.1.

In Figure 6.1, we show the experimental ISFs at a fixed scattering wave vector and various temperatures for sample f6-S1, with 16 arms and PS fraction 0.5 and different concentrations, varying from 2.7%wt to 1.0%wt. One can appreciate qualitative differences in the trend of

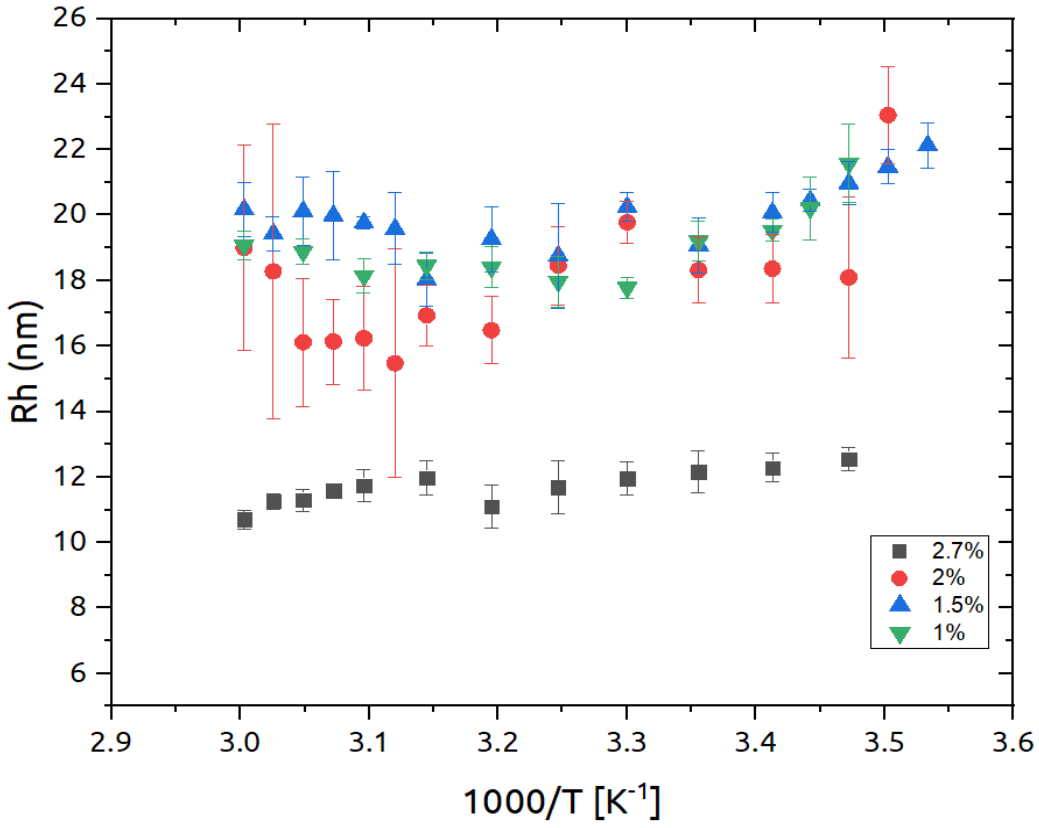

Figure 6.3: Hydrodynamic radius extracted from experimental ISFs for 16 arm TSP with α (PS) =0.49 and Mw=835,200 g/mol. Data for four different concentrations are shown.

cluster formation compared to 3-arm TSPs, presumably because intra molecular interactions are promoted when f increases. For the two comparatively highest concentrations (2.7%wt.and 2.0%wt.) an inherent slow mode appears even at high temperatures, but it does not seem to be a distinct indication of aggregation due to attractions between the sticky ends. Accounting for the effect of temperature variation on solvent viscosity, the data collapse at all temperatures, except for those below 30°C (see Figure AI.1) Also, the intercept of the ISF (at short times) is increasing with concentration at high temperatures, due to the fact that the scattering intensity originating from density fluctuations associated to solvent molecules is minimized because of greater number density in polymer stars. To further justify this, we present in Figure 6.2 the ISFs collected for all concentrations at high temperature, where both blocks are in good solvent conditions. The respective presentation at a lower temperature is depicted in Figure 6.2(b), where high attraction strength reflects the reduced solvent quality for the outer B-monomers. The extracted R_h values of the fast mode for 2.7%wt are much

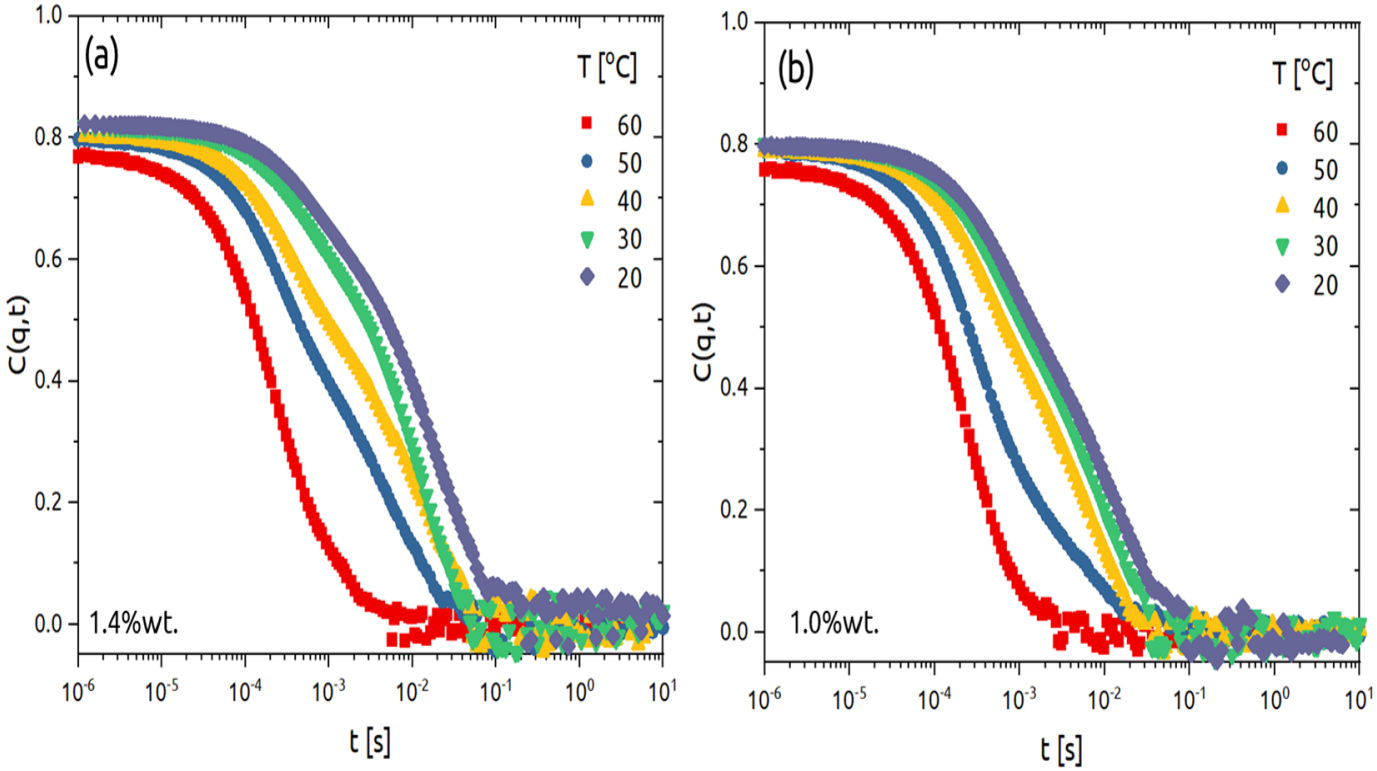

Figure 6.4: Experimental Intermediate Scattering Functions (ISFs) upon increasing attraction strength via decreasing temperature for solutions of a 16-arm TSPs with α (PS) block fraction of 0.25 and M_w^{star}= 915,000 g/mol varying the %wt. concentration (a) 1.0%wt. , (b) 1.0%wt.

smaller compared to lower concentrations and upon diluting the size they increase systematically (Figure 6.3). This could be attributed to steric restrictions caused by adjacent stars which influence the (inter- and intra-star) associations. Interestingly, we observe no decrease upon cooling. In the very dilute regime, where in principle single TSP's cannot feel each other, self-assembly is manifested by the formation of patches [96], [97],[95]. It is possible that is absence in size reduction reflects the inter- and intra-star interactions (we never have a single star) and the size extracted is a mean value, with small changes in the order of 10% not being discerned. In addition the actual hydrodynamic radius increases for temperature below 20°C which is the region where both A and B blocks are in bad solvent conditions. This we explain as a result of two or more stars aggregating. We studied in chapter 5 the effect of different outer B block fraction for 3 arm TSPs in dilute regime. Overall, we show that higher PS fractions yield smaller Rh sizes. Moreover, the characteristic decrease in size for lower α (PS) was shifting to lower temperatures. Moreover, the ISFs exhibit a very similar behavior with a slow mode appearing when the temperature is decreasing. Figure 6.4

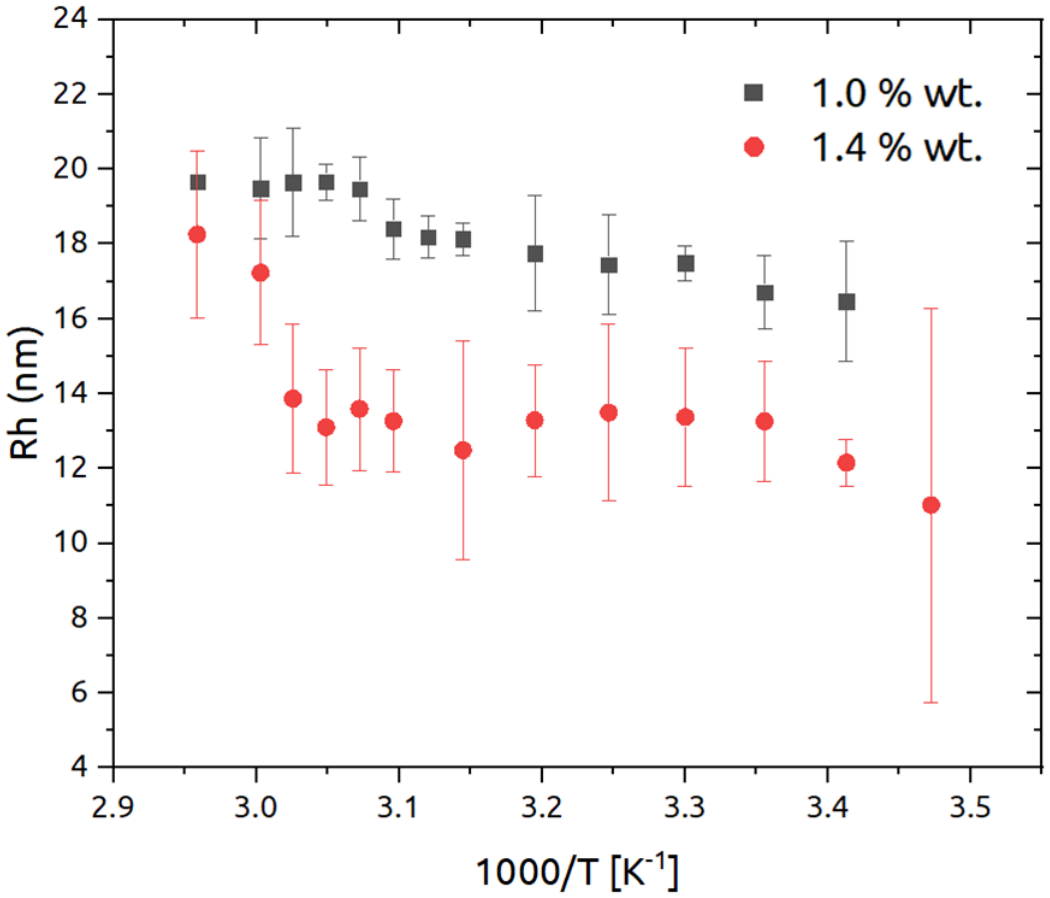

Figure 6.5: The hydrodynamic radius, Rh, of single stars extracted from the fast process in the experimental ISFs for a16 arm TSP with PS fraction of 0.29.

depicts the ISFs of two solutions at different concentrations (1.4% and 1.0%wt.) for a 16-arm TSP with α (PS) = 0.25. Interestingly, we see a slow mode when the solvent deteriorates, which appears to be very broad, hinting at the formation of a network. Note that we have similar average molecular weight in the two 16-arm TSPs, however we probe a clear two-step decay for lower concentration only in one case, where the outer B-block fraction is less. What is remarkable is that the cluster formation is observed at high temperatures above the cloud point of the outer B-block. A tentative explanation could be associated to the much higher molecular weight both per arm and per star and the consequent change in solvent quality (compare also to the analogous 3-arm TSPs). To extract the hydrodynamic sizes of the two processes, i.e., individual TSPs and clusters, we used the CONTIN analysis. At high temperatures, for 1.4%wt., $R_h \approx 18 \pm 2$ nm and for 1.0%wt, $R_h \approx 20 \pm 1.4$ nm (see Figure 6.5). Compared to the findings for size of the single TSP with higher PS fraction, we see that the

size is larger when the polystyrene fraction is greater. The radius of gyration of the polystyrene outer blocks is expanded to approximately the same size as the whole macromolecule while that of the polyisoprene inner segment assumes the dimensions of a homo-polyisoprene star of equivalent molecular weight and functionality [98],[99]. So, the greater the PS fraction, the greater the size. This is in agreement with the results of the same study on lower functionality telechelic stars discussed in Chapter 5. However, we only see a decrease of the size in the case of 0.3 PS which much steeper in the case of 1.4%wt. (~30%) compared to 1%wt. (~10%). Furthermore, a second decrease of the single-TSP Rh occurs at temperatures below the θ-temperature of the inner block for the lower PS fraction (0.25), in contrast to the higher one (0.49) . This is attributed to the intramolecular interactions since the solvent quality becomes worse for almost half of the TSP, leading in to collapse into a patchy watermelon structure. Data for the slow modes are not discussed here, yet are shown in the supplementary information (Figure AI.2); they require further quantitative analysis in the future.

CHAPTER 7: SELF-ORGANIZATION AND DYNAMICS OF STAR DIBLOCK-CO-POLYMERS IN A SELECTIVE SOLVENT FOR OUTER-BLOCK

As detailed in chapters 5 and 6, exposing TSPs to a selective solvent for the inner block, leads to an interplay between inter- versus intra-star associations which provides a rich and tunable behavior already in dilute solutions. For example, the experiments performed for dilute solutions of 3-arm TSPs provide insights for fine tuning the self-assembly into micelle aggregates and percolated networks. The latter reflects enhanced micellar interconnectivity. On the other hand, TSPs of higher functionality and high PS fraction do not show evidence of a distinct slow mode. This triggers further investigations. In this chapter we discuss the self-organization and dynamics of stars of diblock-co-polymer arms consisting of polyisoprene (PI) outer and polystyrene (PS) inner blocks, dissolved 1-phenyldodecane which is selective for the outer block. Two different diblock-co-polymer stars were studied; (i) sample f6-inv in Table 4.1 with inner block fraction of α(PS)=0.49, functionality of 6 arms and M_w^{star}=270,000 g/mol; (ii)

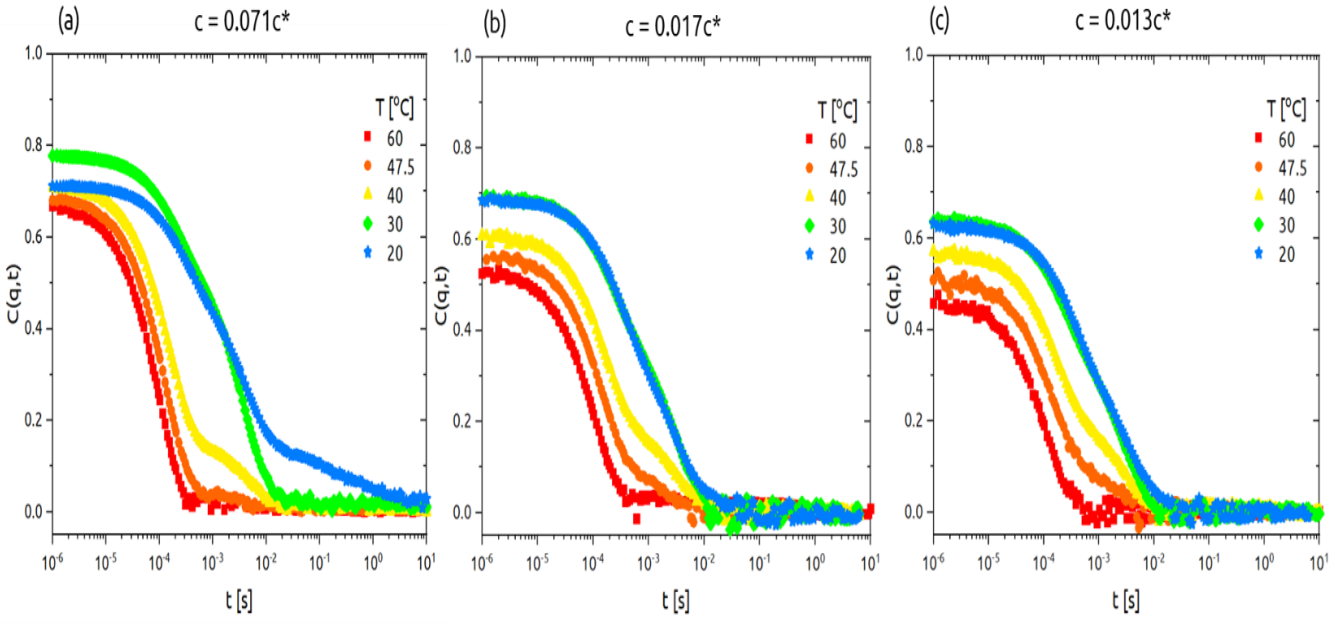

Figure 7.1: Experimental Intermediate Scattering Functions upon increasing attraction strength via decreasing temperature for dilute solutions of 6-arm Diblock copolymer (f6-inv) star in selective solvent to outer block, at varying concentrations (a) c = 0.071c* (b) c = 0.017c* (c)c = 0.013c*

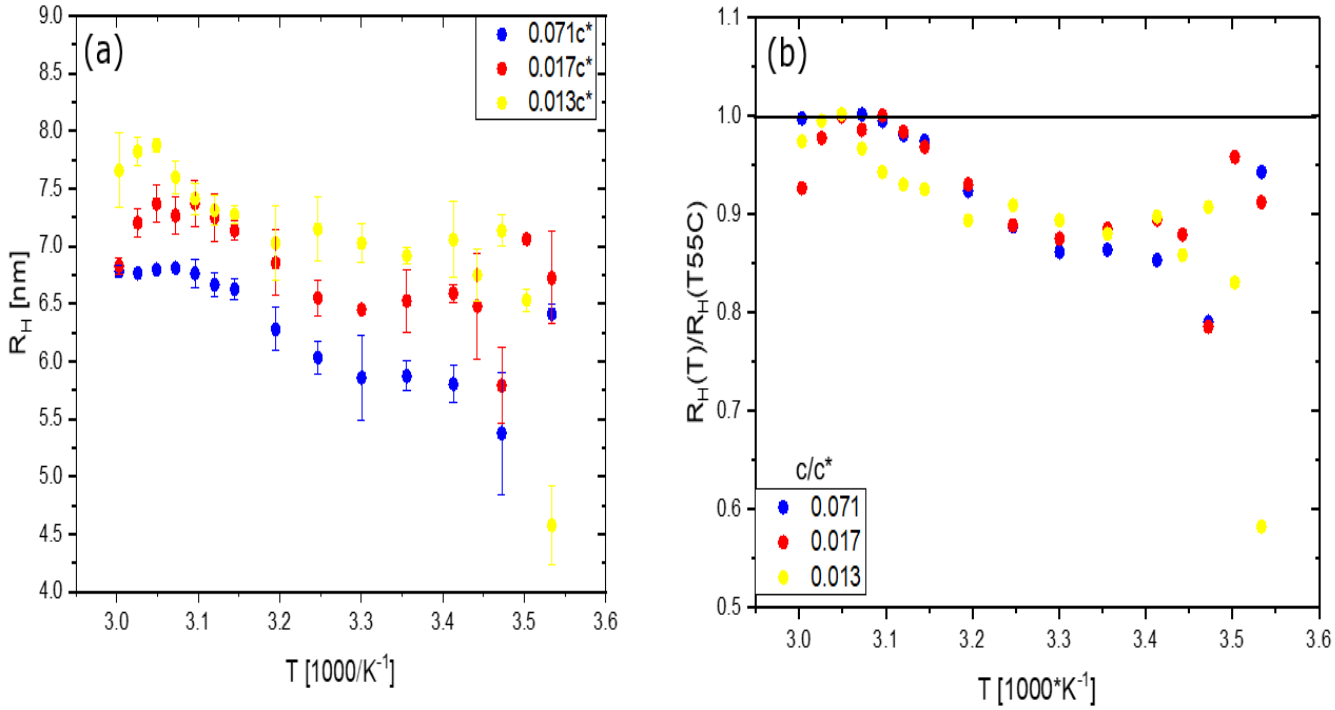

Figure 7.2: (a) The hydrodynamic radius, Rh, extracted from the fast process of the experimental ISFs for three concentrations of the 6-arm star in selective solvent for the outer block. (b) The Rh normalized by its plateau value at high temperatures.

sample f16-inv with α(PS)=0.50, functionality of 16 arms and M_w^{star}=816,000 g/mol. The sample preparation protocol of previous chapter. All concentrations investigated are in dilute regime. Note that c^* is calculated using the R_h value of the single star at high temperatures. The ISFs show two distinct trends upon changing temperature (see Figure 7.1). At high temperatures, there is a single exponential decay that indicates the existence of individual stars in solution. However, when the temperature is reduced below the θ-temperature (~52.5°C) of the inner-block, the ISF features a two-step decay which indicates coexistence of two distinct populations in the system. The first decay (fast process) in the ISF is similar to the one observed at high temperatures and hence represents the individual stars in solution. On the other hand, the second slow decay (slow process) reflects the presence of large aggregates (clusters of TSPs). The slow process becomes more pronounced as the temperature is decreased further. This trend is almost identical to what we have observed so far in the case of TSPs. However, in this case when we are below the θ-point for the outer block, so the star is in bad solvent conditions for both blocks, instead of noticing a broadening of the slow mode and distinctive increase of the intercept value (as in TSPs), we barely see any change. The CONTIN algorithm [57], [100] was used to extract the relaxation time, hence the

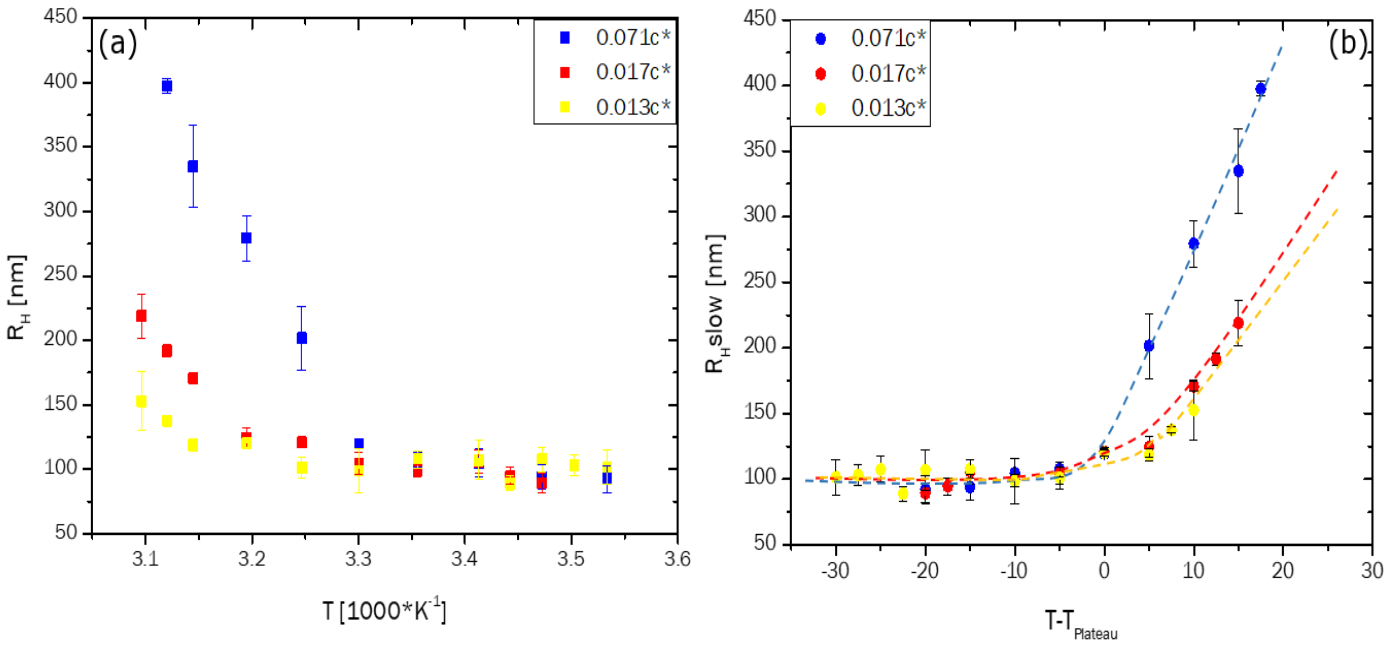

Figure 7.3: (a) The hydrodynamic radius, Rh, of clusters extracted from the slow process of the experimental ISFs. (b) The Rh scaled by its value at the temperature value when the plateau first appears. The dashed lines are a guide for the eye.

hydrodynamic radius, of each decay. Figure 7.2 depicts results for the fast mode. To start with, for all three concentrations a step decrease of size is observed when we pass over the θ-temperature of PS (inner block). We believe that upon worsening the solvent for the inner block, the solvophilic hairy corona acts as a protecting shield and the solvophobic core that shrinks leading to a size decrease [101]. Evidently, the single molecular morphology of the $(BA)_n$ star-block copolymer is very similar to the micelle self-assembled by linear AB diblock copolymers, yet in the case of infinite dilution unimolecular micelles are formed. Despite that, there is a slight increase of the R_h value upon decreasing concentration when we normalized with the R_h value that corresponds to the high temperature plateau, all appear to have the same relative decrease (~13.0%), see Figure 7.2(b). Compared with the findings of Chapters 5 and 6 for TSPs, there is no formation of various patches because there are no sticky ends. Sheng and coworkers nicely confirm this via particle dynamics simulation analysis [102]. An illustration for comparison of such 5 arm diblock-co-polymer stars $(AB)_n$ and $(BA)_n$ can be found in the supplementary information (see Figure AI.3). This may affect the actual self-assembly mechanism. Indeed, in Figure 7.3 we show the hydrodynamic radius associated with the slow mode of the experimental ISFs, where one may observe that even though all three concentrations start off with a decreasing tendency for Rh, after a certain temperature it

reaches a plateau value. When shifted by the temperature where this plateau first appears, we see that the plateau value is the always same (~100 nm). The only thing changing is actually the slope, i.e., the transition to the plateau value. Note that this effect could be due to saturation of the number of stars that could organize per micelle.[102], [103] Estimating Rh to be around 7.0 nm, we can calculate that approximately fifteen stars are organized into a micelle. So once this limit is reached, the micelles don't grow further in size, instead more micelles formed. Further, we compare a dilute solution of 16-arm diblock-copolymer star (PS-b-PI) in selective solvent for the outer polyisoprene block, having nearly the same fraction and very similar molecular weight with the 16-arm TSP (selective solvent for inner block) from chapter 6. Experimental ISFs upon increasing attraction strength by decreasing temperature are presented for two different concentrations in Figure 7.4. For clarity of presentation, we plot only three temperatures representing good solvent conditions (T=60°C), selective for outer block (T=40°C) and bad solvent for both blocks (T=20°C). Even though the appearance

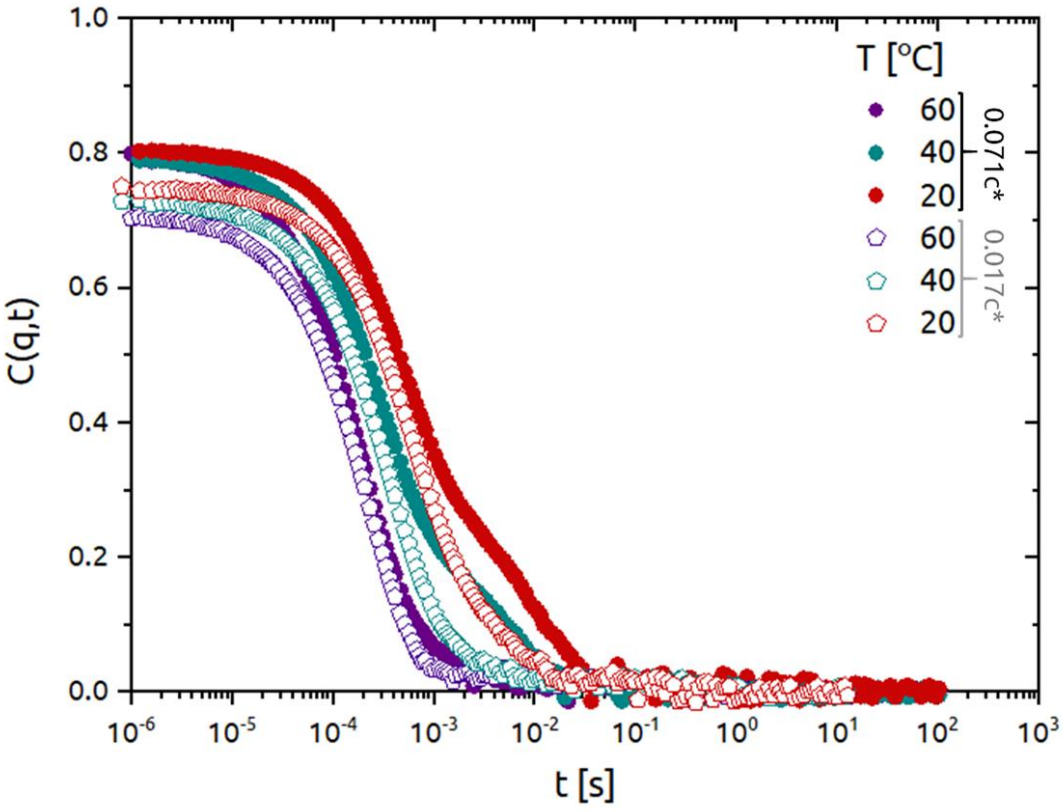

Figure 7.4: Experimental Intermediate Scattering Functions [g^2 (t)-1] upon increasing attraction strength via decreasing temperature for dilute solutions of 16-arm Diblock copolymer (f16-inv) in selective solvent for the outer block of two different concentrations. The closed symbols are for c = 0.071c* and the open symbols are c = 0.017c*.

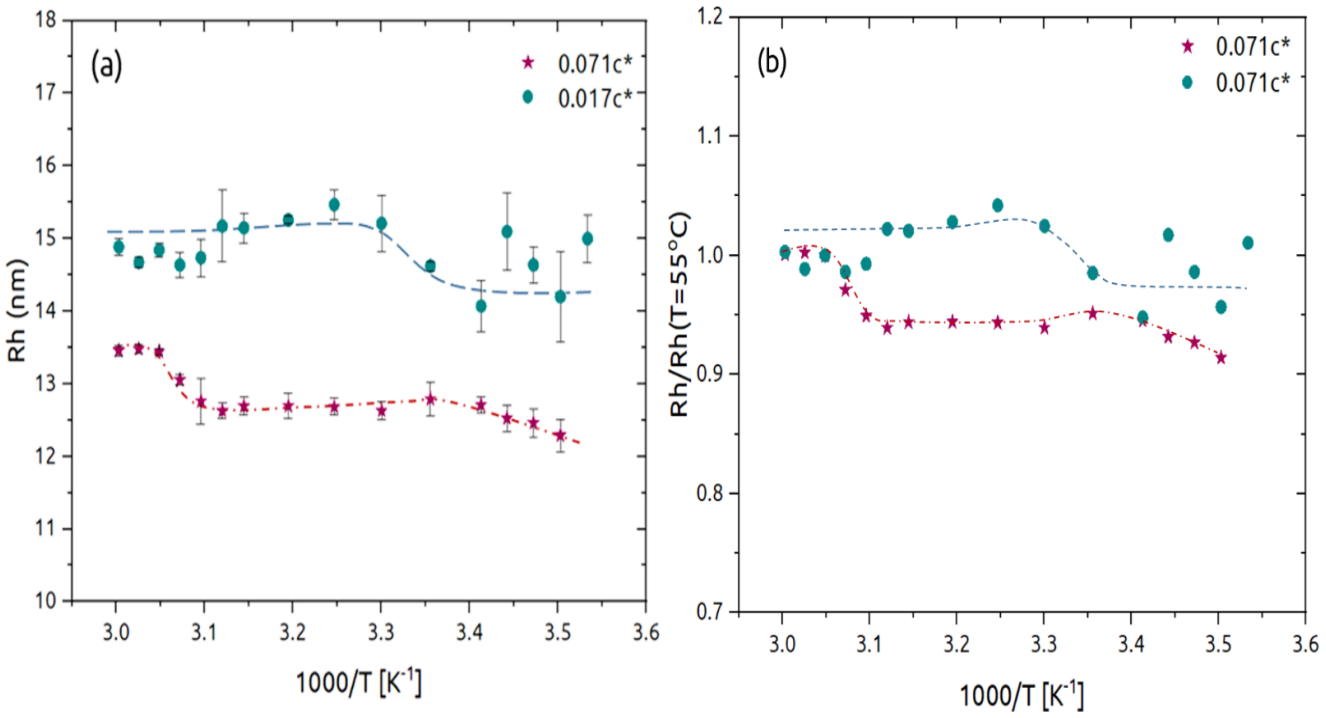

Figure 7.5: (a) The hydrodynamic radius, Rh, extracted from the fast process in the experimental ISFs for two concentrations of the 16 arm star in selective solvent for the outer block. (b) Rh normalized by its plateau value at high temperatures. Concentrations of c = 0.071c* and c = 0.017c* are presented.

of a second mode indicating a bigger population is rather obvious in the case of c=0.071c*, when moving towards infinite dilution (c=0.017c*) it fades out. We then analyze the ISFs to get information about the hydrodynamic sizes of both populations. Figure 7.5 depicts the Rh extracted from the fast mode. Is clear that once again we observe a small size reduction due to shrinkage of the solvophobic core. This however is not the case for the concentration of 0.017c*. Data collected for this sample are much more scattered and the overall size we get is higher, however stars in selective solvent seem to have smaller sizes, as also observed in simulation studies. For clarity and better comparison with the previous 16-arm TSPs, we normalized the Rh with its value at high temperature (see Figure 7.5(b)). Remarkably, for the TSP case mentioned in Chapter 5, where there is local intra-particle aggregation, no size drop was observed whatsoever at single molecular level (fast mode). Helpful insights were provided by coarse-grained molecular dynamics simulations performed in the group of Prof. C. N.Likos that a drop of size on cooling is evident for both types of f=16 stars (see Figure 7.6).This appears to Remarkably, at the reverse case mentioned in Chapter 5, where there is local intra-particle aggregation happening, no size drop was shown whatsoever at single

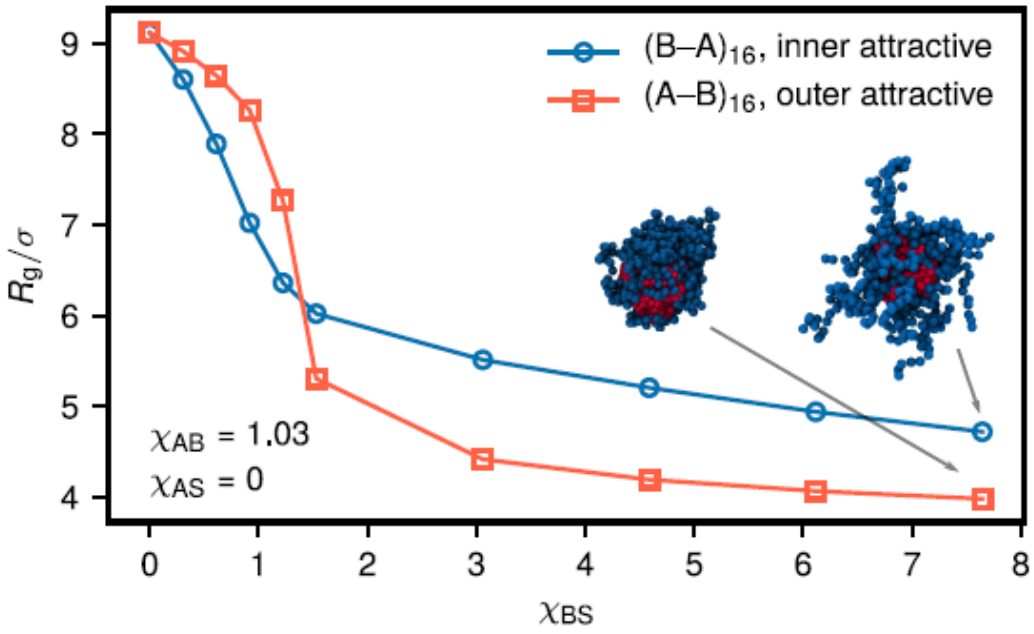

Figure 7.6: Single star size as a function of monomer-solvent interactions for different architectures. Rg of a single star with $(B–A)_{16}$ (blue line) and $(A–B)_{16}$ (red line) architecture for different solvent qualities. B blocks are subject to different solvent conditions and the solvent quality is controlled by varying χ_{BS} (Flory-Huggins parameter between B block and solvent molecules). As a reference point, B is correlated to PS and A to PI monomers. σ is for the size of the monomer that they account the same. This plot is reproduced without permission from simulation analysis of Iurii Chubak, University of Vienna.

molecular level. Helpful insight was provided from molecular DP simulations performed by C. Likos group at the same molecules, show that a drop of size on cooling is evident for both types of f=16 (see Figure 7.6).This appears to contradict the experimental data provided when PS is outside. The main reason for discrepancy is that the simulations are coarse-grained and not atomistic so is not an exact copy of the star molecule. In addition, simulations are for a single star in a box whereas in our case the molecular study is inside a dilute solution. At last, simulation analysis accounts only for a theta point of only for B-block or else PS. At this instant, all inner B-blocks of the star form a solvophobic core since they are relatively large in length. However, the outer, solvophilic A-blocks give rise to a shell of hairy arm. This offers steric protection and prevents the contact between two B-block cores. To a first approach, the effective interaction potential between two such stars is repulsive and consequently the size should remain constant up to the point where the temperature is reduced below the θ-point of the outer block. Since the solvents becomes less favorable for A, the interactions between A-A blocks are more attractive. Representative snapshots from simulations are presented in the inset of Figure 7.6. Figure 7.7 depicts the temperature-dependent Rh data

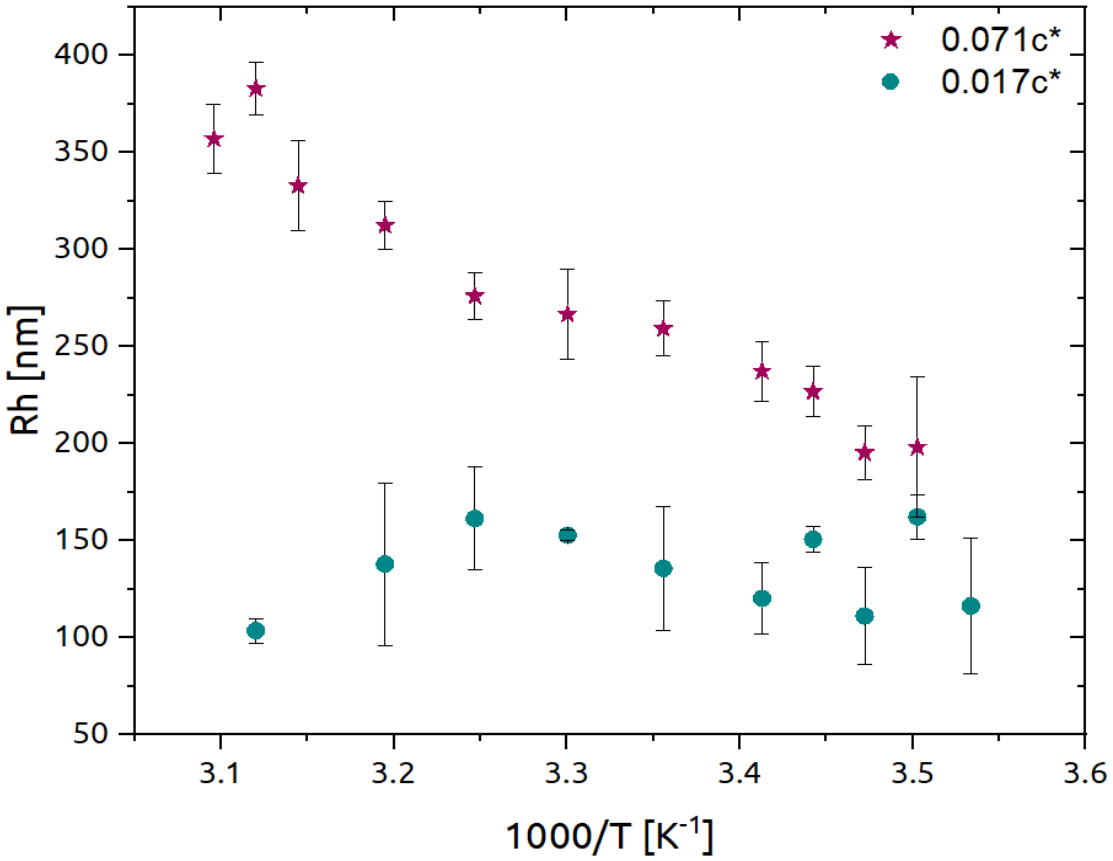

Figure 7.7: The hydrodynamic radius, Rh, of the clusters extracted from the slow process in the experimental ISFs for two concentrations of the 16-arm star with selective solvent for the outer block. Data for concentrations of c = 0.071c* and c = 0.017c* are presented.

for the clusters associated with the slow mode. For the slightly more concentrated system the initial value of around 350 nm gradually drops to sizes around 200 nm. Still, for the more dilute case, we always obtain a steady value around 150 nm. Is very important to highlight that all experiments were performed at an equilibrium state. Interestingly, the TSPs reached this state very fast especially when compared with the inverse system which could take up to 12 hours to equilibrate. Simulation snapshots for both cases are presented in appendix I (Figure AI.4).

CHAPTER 8: REINFORCING THE MECHANICAL PROPERTIES OF HAGFISH MUCIN HYDROGELS

In this chapter, we examine different approaches to reinforce (i.e., improve the mechanical properties) of the major component of hagfish slime, the mucin proteins originated from gland mucous cells. Mucin proteins make a highly elastic mucus hydrogel. Its viscoelastic character is derived from the interactions which are believed to be mostly of hydrophobic and electrostatic origin. We recall that the leading part of the protein backbone is a polypeptide decorated with oligosaccharide side-chains and is known to be anionic because of the existence of terminal carboxyl groups that participate in repulsive electrostatic interactions. Moreover, some peptide residues , i.e. proline, give rise to hydrophobic interactions in the system, whereas cysteine-rich domains act as disulfide bonding sites [16], [17], [104]. All these parameters which strongly affect the final material properties are not easily controlled. With this in mind, we as address here the challenge to make this hydrogel more robust and essentially improve its mechanical performance. Adding composites with filler nanoparticles is one of the traditional approaches to toughen elastomers. Inspired by its nature and the original mechanism of the slime hydrogel formation, we attempted a different approach, i.e., the mechanical reinforcement via interpenetrating networks. The sample preparation protocol we followed for forming all mucus gels characterized with capillary break-up extensional rheology is the fast network formation via sloshing (see 4.2.3, section I.), while additives were introduced into the system after gelation. We also present data obtained by small-amplitude oscillatory shear rheology. For the experiments, the mucin hydrogel was formed via the dialysis protocol as presented in part 4.2.3, section II. We chose to use this method since due of ion screening there is more water intake and we can produce larger amounts. This is very useful for conventional rheology where it was needed around 1 mL of sample for the geometry we used was necessary for measurements. The larger fraction of these studies took place in ETH Zürich at the Department for Health Sciences and Technology under the supervision of Prof. Peter Fischer.

8.1 Addition of Silica Nanoparticles

We incorporated silica nanoparticles into hagfish mucus hydrogels with two different ways (Fig.AII.1). SiO2 nanoparticles (SNPs) were originally expected to be very promising since they are typically widely used in biological applications due to their excellent biocompatibility, low toxicity, thermal stability and, importantly, easy large-scale synthetic route. However, as soon as the SNPs came in contact with the mucin network, the collapsed and phase-separated. Visual observations indicate a transition from originally a transparent gel to a milky, tacky and gummy-like sample (Fig.AII.1). Regardless of that, we tested its response with CaBER but not surprisingly no capillary filament formation was possible, and a breakage occurs whilst the two plates separate (Figure 8.1). We attribute this response to the way by which the anionic charges (COO^-) at the backbone of mucin proteins are affected by the anionic sites (O^-), yielding an instant network collapse. This triggered an attempt to dissolve the SNPs in a selection of dispersing media where the type of ions in the solution and the salinity of the medium were varied, hence altering their pH and ionic strength. Some combinations

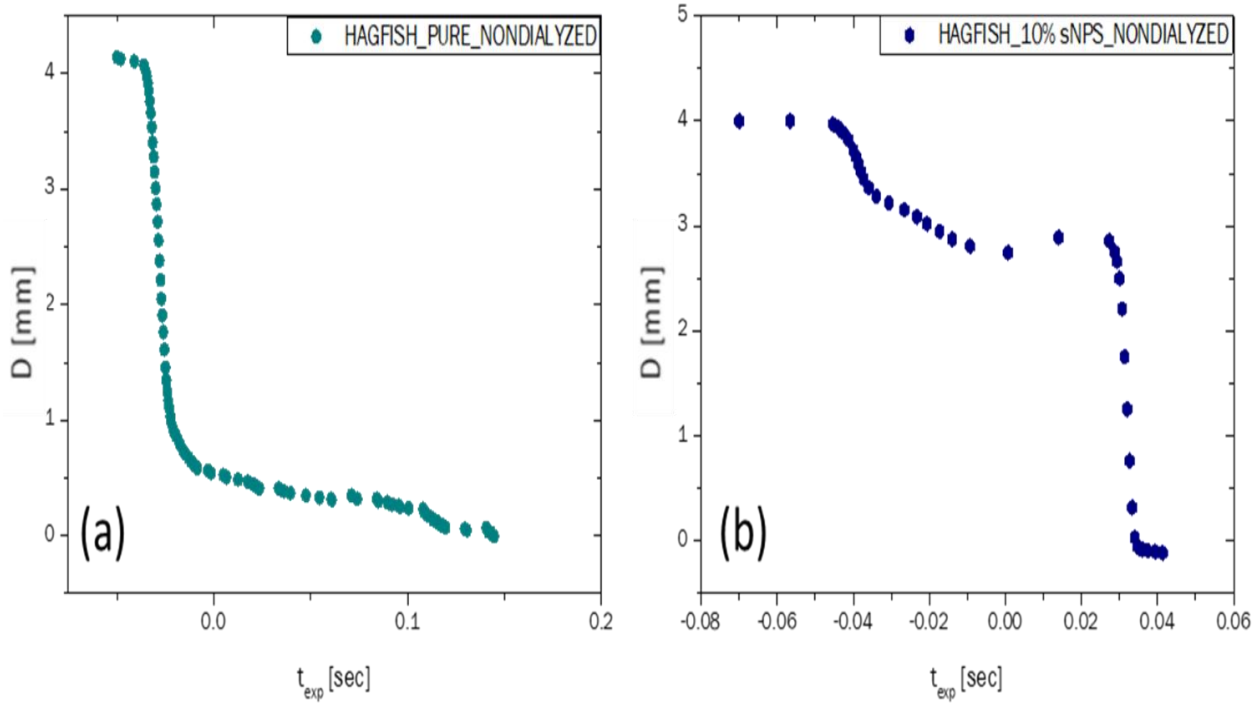

Figure 8.1: CaBER tests on (a) Hagfish slime without additives and (b) when 10% SNPs were added to the same sample. In the first case we have a normal response of capillary breaking with t_{br}=0.15 s, whereas in the second case there is a 'snap' during strike time and an apparent capillary break at 0.04 s. Both graphs are in Lin-Lin scale for clarity.

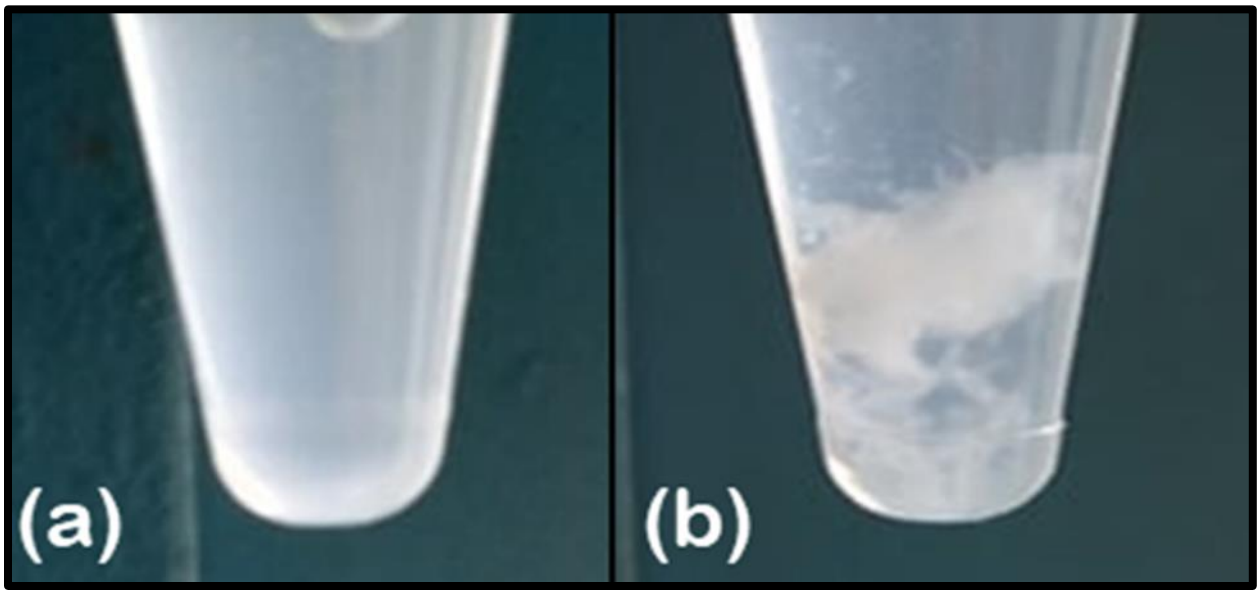

Figure 8.2: (a) Pure hagfish mucus hydrogel before the addition of SNPs (b) after the addition of the stabilized SNPs suspension with 0.1M HCl. The white region is the collapsed network that is phase separated.

tried e.g., artificial sea water) led to an unstable suspension. Next, adding 0.1M HCl, a proton donor, and making the system acidic seemed to stabilize the suspension (which has very low pH value, suggesting that we are far from the isoelectric point of the mucin protein). This approach was suggested by Sofla and coworkers [105], [106]. All pH measurements were performed the pH meter 780 by Metrohm. The next step involved incorporation of the stabilized suspensions to the mucus hydrogel (0.1mg/mL). However, phase separation was again observed and no capillary filament could be formed. An example of the mucin gel before and after the addition of silica nanoparticles is shown in Figure 8.2 showing clear phase separation. Finally, TWEEN®-20 was used as an alternative. It is known to have a positive effect in stabilizing porcine intestinal mucin [107]. Despite our effort to make silica nanoparticles work, none of the aspects we tried was efficient.

8.2 Addition of CARBOPOL® Nanoparticles

As we saw earlier adding silica nanoparticles did not work as reinforcing additives, probably due to their charged surface area, which leads to agglomeration of mucin proteins [108]. This is because positively charged particles act as cross-linkers to mucin gels. We know already that Ca^{2+} cations have a gelling effect in mucin gels [37], [39]. This triggered the need to find efficient alternative non-metallic nanoparticle. We

chose to use CARBOPOL®, a water soluble polymer, mostly used as an emulsifying, thickening and gelling agent. It is essentially a carbomer of high molecular weight cross-linked polyacrylic acid polymers. Carbomers have a carbohydrate backbone and –COOH sides, so when introduced into hagfish slime most probably they should interact with the anionic sites of mucin glycol proteins, primarily through hydrogen bonding. However, since we don't know neither the exact chemical structure of CARBOPOL®, nor the exact form of mucin-like glycoproteins, it is not possible to reach definite conclusions. We prepared a control sample, a pure mucus gel with a concentration in mucin vesicles of 1.58mg/mL. To this sample we added the CARBOPOL® aqueous solution by gently mixing, and then tested it with CaBER. The amount of the additive nanoparticle was gradually increased up to the point where the capillary was not breaking even after 120 seconds. In Figure 8.3 the extensional data of different samples

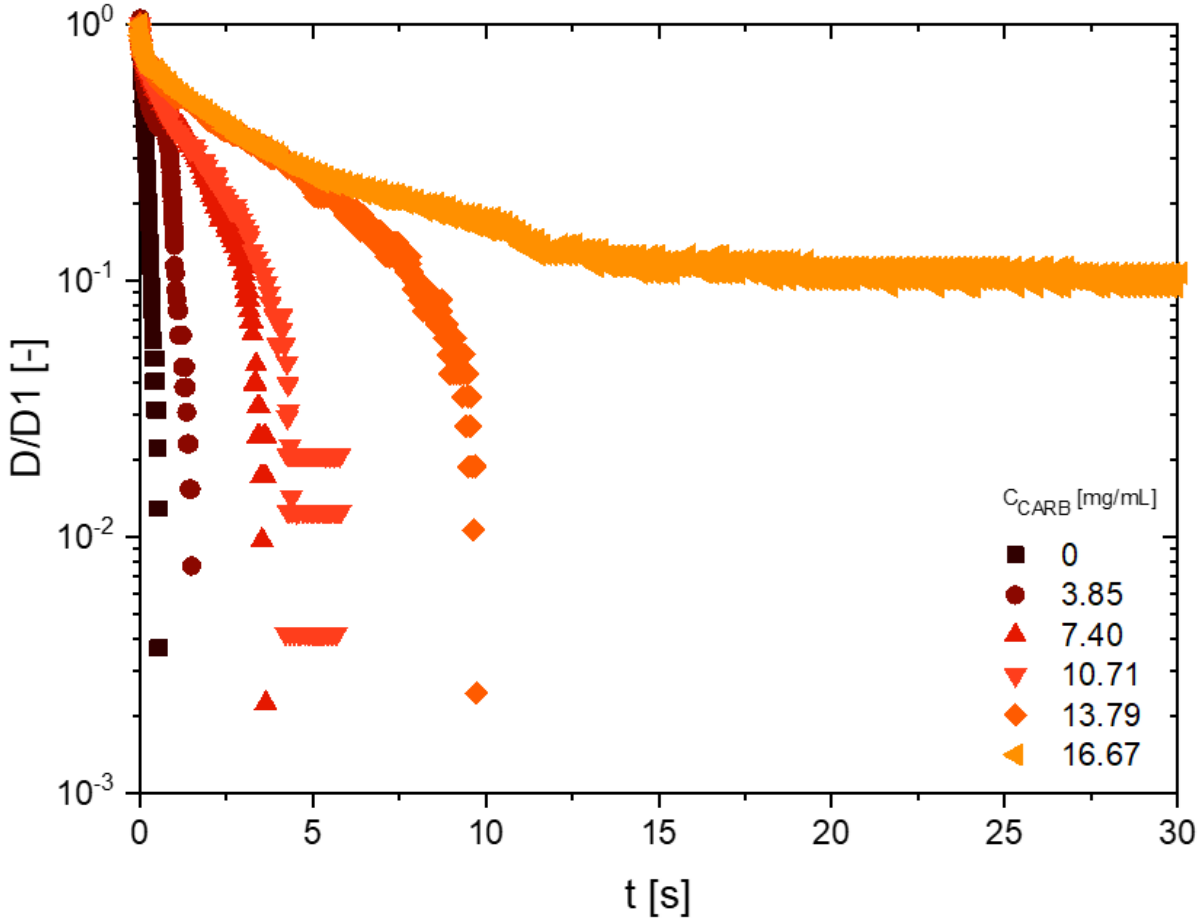

Figure 8.3: Capillary Break-up Extensional Tests on hagfish gels composites where CARBOPOL® nanoparticles where used as additives. As a reference, the pure mucus gel is used. The estimated concentration is c_{mucin} = 1.58 mg/mL.

tested are depicted. Note that for the largest concentration of CARBOPOL® a shorter test time window as used in order to better visualize and comparison between various data curves. We consider them to be space-filling particles which increase the elastic modulus of the network by increase of the volume fraction (akin to Guth-Gold effect [109]). In addition, the interfacial area between the nanofillers and the polymer affects the properties of the composite [110], [111]. This mechanism seems to be at work in the present case of mucus gel. However, it is known from the literature [66], and confirmed by our experiments, that the mucus hydrogel is not stable over time, as it undergoes significant weakening. This was also the case even when the carbomer fillers were used. To obtain more insights, we further characterized the effect of carbomer

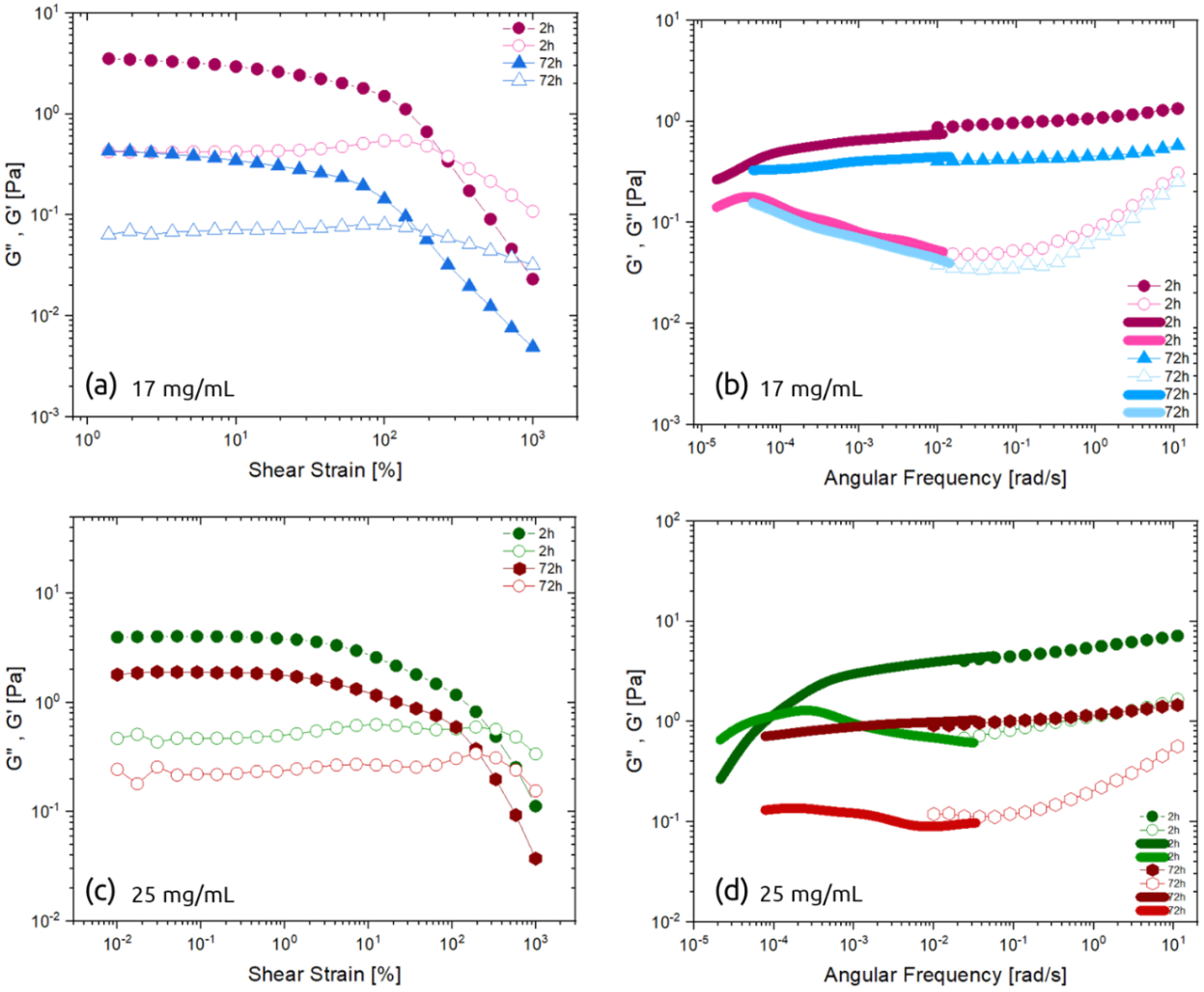

Figure 8.4: Oscillatory shear rheometry for two different concentrations of CARBOPOL® nanofiller, 17 mg/mL (top) and 25 mg/mL (bottom). Closed symbols represent the storage modulus G' whereas open symbols the loss modulus G''. Lines indicate creep experiments converted into viscoelastic moduli.

nanofillers by means of small-amplitude oscillatory shear rheology (SAOS). In Figure 8.4 we show dynamic strain sweeps and dynamic frequency spectra complemented by creep tests for a mucus gel of about 0.4mg/mL. We know from previous works [34], [39], [66] that this concentration of mucin proteins corresponds to a storage modulus of about 0.05 Pa. For consistency, we have also tested the response of a mucus gel of 0.65 mg/mL and our findings match with the ones reported in the literature (see Figure AII.2). We chose to study the linear rheology only for concentrations of the additive that effectively improved the mechanical stability in CaBER tests (17mg/mL and 25 mg/mL). We show here characteristic data curves of two different time periods; (i) after 2 hours from loading and (ii) after 72 hours from loading the sample. One can clearly see that for both concentrations the storage moduli appears to be much higher compared to the pure mucus hydrogel, yet in both cases the sample weakens over time. Regarding the 17mg/mL, G' is about 1 Pa whereas for the 25mg/mL about 4 Pa when first tested after an equilibration of 2 hours, but it drops to 0.3 Pa and 1 Pa, respectively, after 72 hours. Further, when comparing the dynamic strain sweeps (Figure 8.4 (a) and (c)), we observe that the linear region is shifted towards lower strain amplitudes with time. Moreover, in the case of 17 mg/mL the drop is steeper, whereas for 25 mg/mL it is a 2-step drop. This could reflect a first relaxation of CARBOPOL® particles and later on of the gel. Finally, we only observe a low-frequency moduli crossover for the 25 mg/mL after 2 hours at about 10^{-4} rad/s, which could be a potential effect of the nanoparticles not being completely dispersed and homogenized in the gel at this relatively high number density.

8.3 Addition of Organosilica (MPTS) Nanoparticles

The next step was to embed the thiolated organosilica (MPTS) nanoparticles into the mucus hydrogel. Organosilica nanoparticles made out of MPTS [81], [112] which are not hard spheres, have been tested and characterized as mucoadhesive agents[81], [82]. Their adhesive character derives from disulfide bonding between their –SH ends and cysteine domains. For their characterization, aqueous suspensions of MPTS particles were prepared and both their zeta-potential and size were measured (see Chapter 4). All values obtained are a close agreement with the literature [113]. When we tested their

Figure 8.5: Mucus hydrogel after the addition of MPTS nanoparticles (1.20 mg/mL).

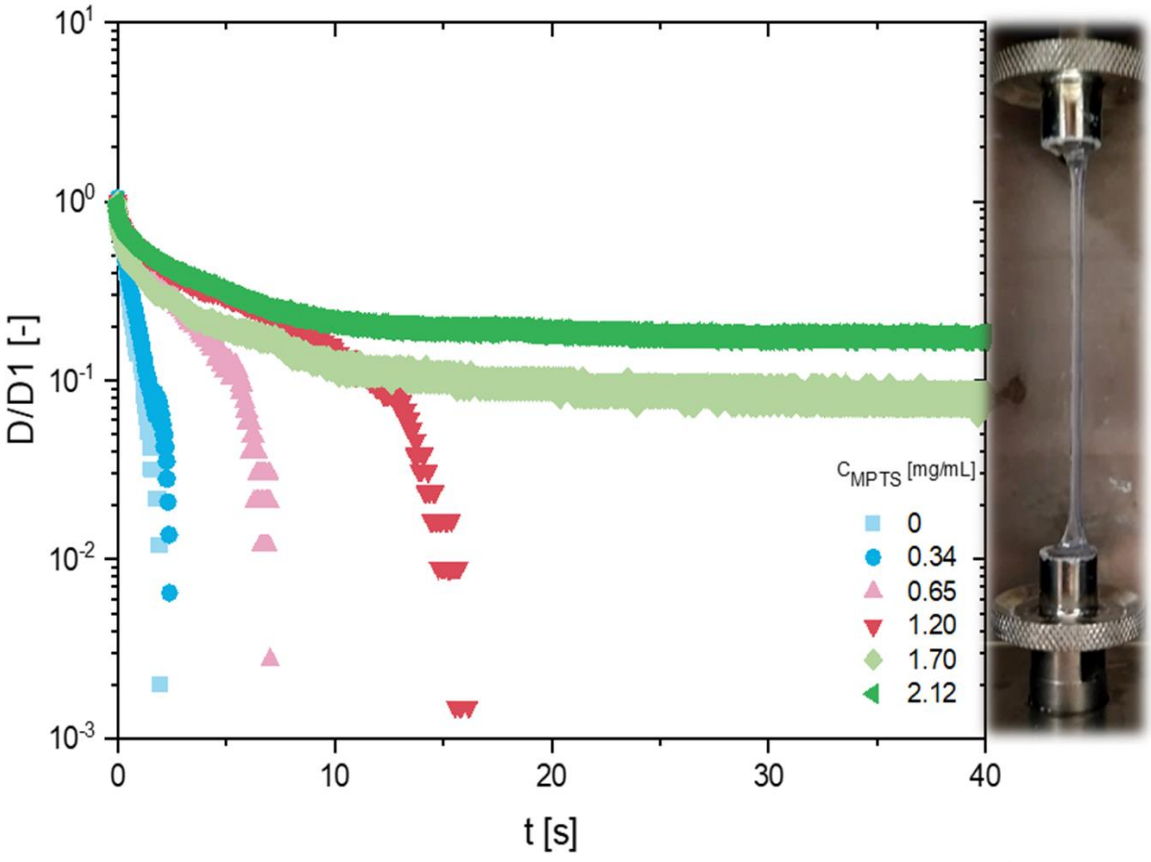

Figure 8.6: Capillary Break-up Extensional Tests on hagfish gel composites based on nanoparticle additives made of thiolated organosilica (MPTS). For reference, the pure mucus gel used. The estimated concentration is c_{mucin} = 1.52 mg/mL.

interactions with mucin proteins, we observed that when their concentration increased, some flaky regions appeared, however no phase separation was observed visually (Figure 8.5). We have noted that, the more organosilica particles we add the more these domains grow, so we have decided to work with very small nanoparticle concentrations. This could be attributed to possible hydrophobic interactions between the hydrophobic regions of the backbone (COO-) and exposed negative sites of the MPTS body (O-). This is similar to the collapse mechanism of the SiO_2 described earlier. Nonetheless, the effect of these organosilica nanoparticles is undoubtedly exceptional since we manage

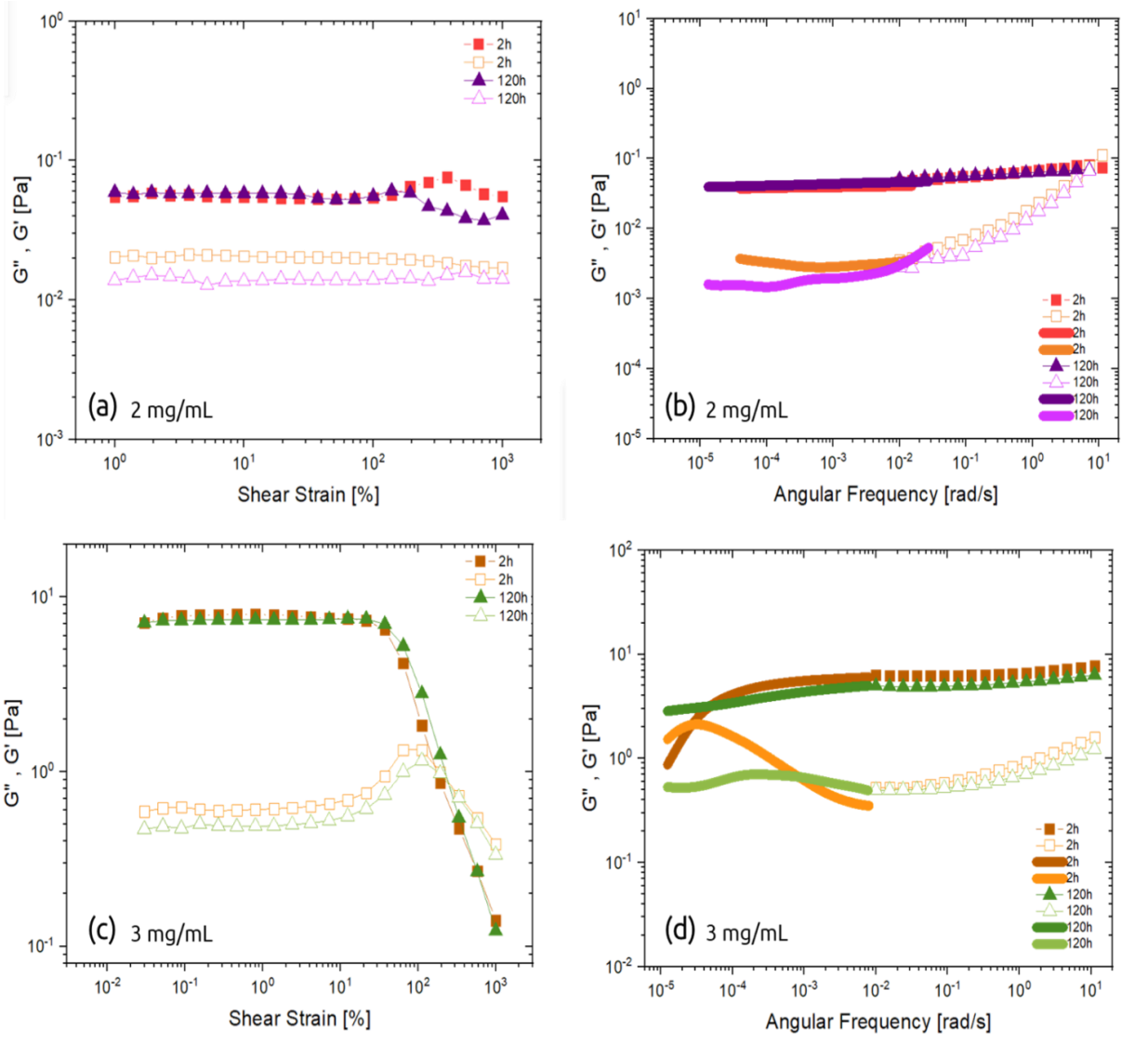

Figure 8.7: Oscillatory shear rheometry for two different concentrations of organosilica (MPTS) - mucin nanocomposite, 2 mg/mL (top) and 3 mg/mL (bottom). Closed symbols represent the storage modulus G' whereas open symbols the loss modulus G''. Lines represent creep experiments converted into moduli.

to reach a state where the mucin behaves like an adhesive. This is presented in the inset of Figure 8.6, where the two plates are separated at maximum distance (~30cm) and the sample holds very firmly and does not break. The increase in modulus was due to the enhanced interactions, i.e., hydrogen bonding, disulfide bonding between the nanoparticles and the mucin matrix. This restricts the segmental motion at the MPTS NPs/mucin interface. In addition, the –S-S- bridges are a result of chemical modification of the mucin network, yielding a denser system with reduced mobility of chains. In general, crosslinks form a more rigid, non-flowing network when compared to conventional (physical) entanglements. Even thought we did not have the same quantitative effect in shear, it is evident that this mucin nanocomposites system is very stable over time, especially for 3 mg/mL of MPTS nanofillers (Figure 8.7). The lower concentration does not seem to further strengthen the hydrogel and the plateau modulus has values ~0.05Pa, very close to the one of the mucus gel and at the resolution limit of the rheometer. Nevertheless it really improves its stability over time since the slime without additives becomes completely liquid-like in one day (see Figure

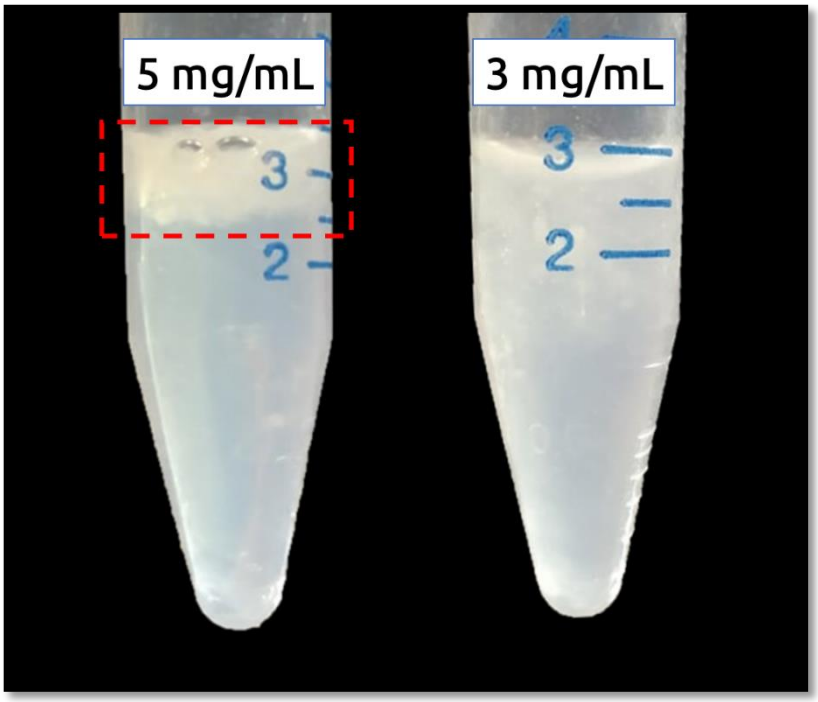

Figure 8.8: Nanocomposites of mucus hydrogel (0.5 mg/mL) with embedded organosilica nanoparticles: (i) 5mg/mL –left and (ii) 3mg/mL –right. The red box highlights the phase separated mucin. However, both samples have heterogeneities.

S2.2 (a)). As for the higher concentration, the plateau G' value is remarkably greater, at values around 5 Pa. Regarding dynamic strain sweeps (Figure 8.7(a) and (c)), for the lowest amount of MPTS particles we see no transition to the nonlinear viscoelastic region but for the case of 3 mg/mL MPTS this transition is very clear. Indeed, at high strain values the G'' reaches a maximum and then we observe a crossover. After this point both moduli decrease and the slopes modulus for G' is around 2 whereas for G" around 1 indicative for transition of jammed systems [114]. As mentioned earlier, the more we increased the concentration, the flakes become more evident and growing in size, and at around 5 mg/mL the system phase separates (Figure 8.7) and of course we could not load it in order to test it. This sets the upper limit in concentration.

8.4 Interpenetrating Networks – Addition of PVA

Interpenetrating networks are known to have a strengthening effect [115][43]. Double network gels (DNs) are novel materials having both high water content and high mechanical strength [42], [43], [49]. DN gels are characterized by a two-component polymeric network; the minor is a highly crosslinked polyelectrolyte polymer chain which forms the rigid skeleton and is the part that strengthens the system, whereas the other one is a network formed by poorly crosslinked neutral polymers which are not fully stretched. When this DN system is subjected to elongation, the weak component uncoils and provides a 'hidden' length in the network, making it highly elastic. This is known as the ductile compound. It was highlighted earlier that mucin-like glycoproteins are charged and thus build a polyelectrolyte network which is more brittle and less elastic than the original hagfish slime. Poly (Ethylene Oxide) is a polymer that can be easily dissolved with various salts making it sensitive to charges [116]. Poly (Vinyl Acetate), on the other hand, is a purely neutral polymer. Polyvinyl alcohol (PVA) is a hydrophilic, biodegradable, non-toxic, semi-crystalline polymer with a wide array of commercial uses. The physical hydrogel of PVA, which is biocompatible and has good mechanical properties [80], [117], [118], is an excellent candidate to be combined with other chemically cross-linked polymer hydrogels. Moreover, PVA can behave like a

hydrogel due to crystalline micro-domains and extensive interchain H-bonding between its hydroxyl side groups. To justify the double network effect, we tested both PVA and PEO solutions. Despite the fact that the interaction with the mucin matrix was weak in both cases, we only have a noteworthy enhancement when PVA solution is introduced. For this reason, we only proceeded on testing with CaBER mucus/PVA mixtures and explored the effects of different amounts of the latter. We prepared samples with different PVA concentration but identical amount of mucin vesicles (1.58mg/mL). It was observed that even low quantities of PVA could enhance the mechanical properties of the mucus gel. When the amount of PVA-solution was further increased to 12 mg/mL, the final composite appeared to be weaker, however it formed

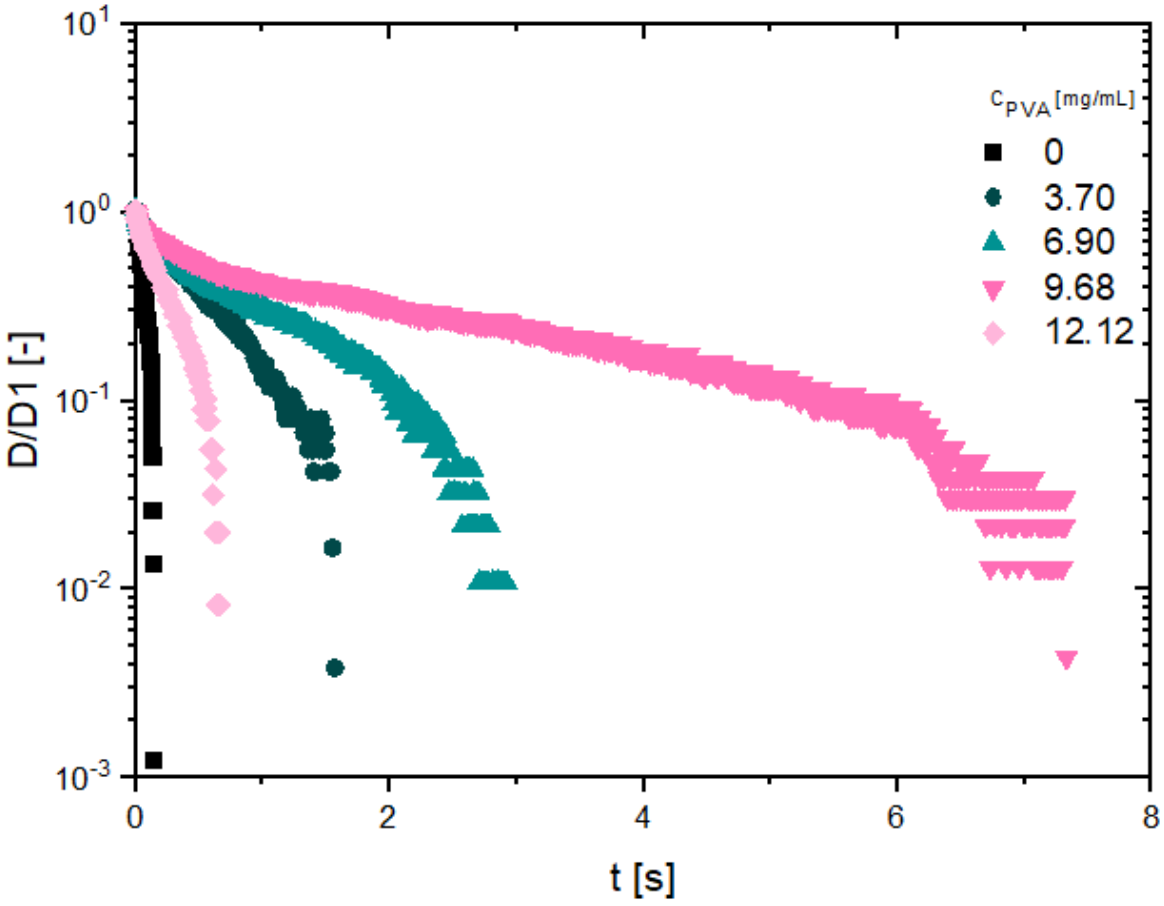

Figure 8.9: Capillary Break-up Extensional Tests with hagfish gel nanocomposites where PVA was used to study the double network approach as a means to improve mechanical properties of mucus hydrogel. For reference, the pure mucus gel is used. The estimated concentration is c_{mucin} = 1.58 mg/mL.

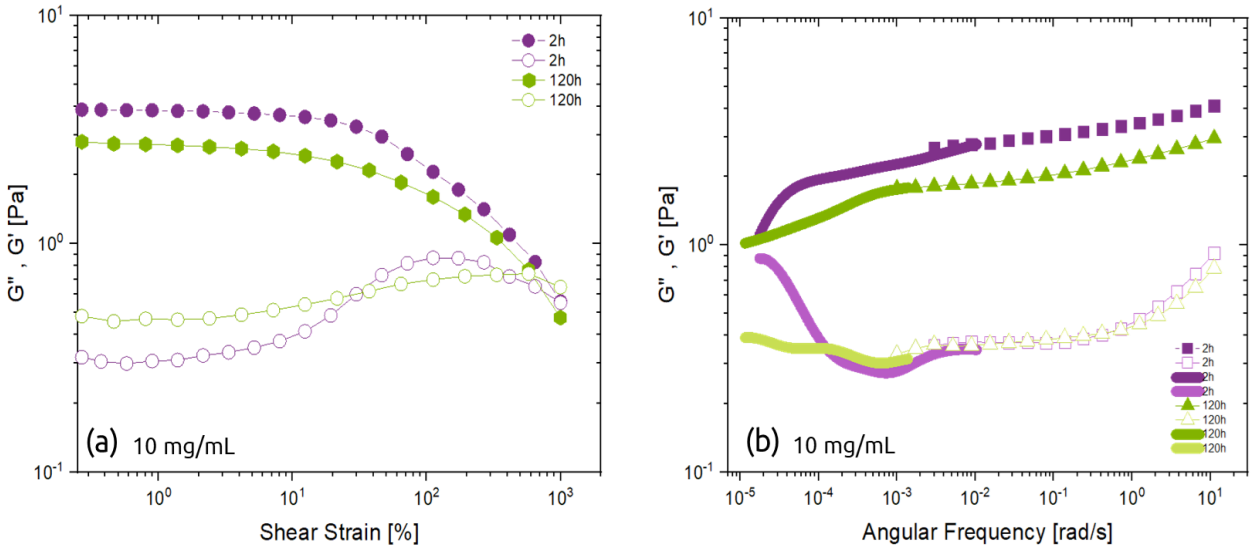

Figure 8.10: Oscillatory shear rheometry for PVA/mucus nanocomposites at a concentration of 10 mg/mL PVA and 0.36 mg/mL mucin proteins. Closed symbols are storage modulus G' whereas open symbols loss modulus G''. Lines represent creep experiments converted into moduli.

a stronger capillary compare to the pure hagfish mucus hydrogel. This could be due to the fact that 12mg/L PVA solution (5%) was diluting the system enough so there was no double network effect. We may speculate, since there was not a complete collapse, that instead of having a system of two interpenetrating networks, the PVA macromolecules do not form a physical network and they just coil around the mucin matrix, creating in this way a semi-interpenetrating network. This leads evidently to a weaker response due to a reduced energy dissipation mechanism. The relevant extensional data are presented in Figure 8.9. Regarding shear measurements, due to limited amount of (mucin) sample. We conducted SAOS rheometry with only one concentration of PVA, 10mg/mL, and carefully introduced it into a mucus gel of 0.36 mg/mL. In Figure 8.10 we present dynamic strain sweep data and dynamic frequency spectra. Interestingly, this combination appears to have a large linear viscoelastic region since even after very large values of shear strain (~1000%), we do not see a moduli crossover in the DSS tests. However, at high shear rates we note again a decrease of the storage modulus and an increase of the loss modulus by more than 10%, indicating an internal structural change. Finally, we observe an increase of the storage modulus, ~ 2 Pa and the gel is relatively stable over time and did not show signs of strong aging.

8.5 Summary and Discussion

To conclude, in order to map the interaction of all additives tested with the mucin proteins we created a state diagram (Collapse/No Collapse) presented in Figure 8.11. SNPs failed in all cases, no matter what the dispersing medium was. However, some alternative additives worked well with the hagfish mucin network (green dots). The collapsed state is highlighted with red, whereas the gel with additives that did not fail with green. For further comparison, in Figure 8.12 the CaBER tests of the most promising nanocomposites are plotted, with reference point being a mucus gel of 1.58 mg/mL. It is clear that the pure mucus undergoes a more rapid filament breakup than PVA/Mucus gel, whilst the CARBOPOL® and MPTS composites do not break at all, but eventually approach a constant finite value corresponding to a thin residual strand. This tendency to form threads is perceived as a typical behavior of adhesives. We fit our data

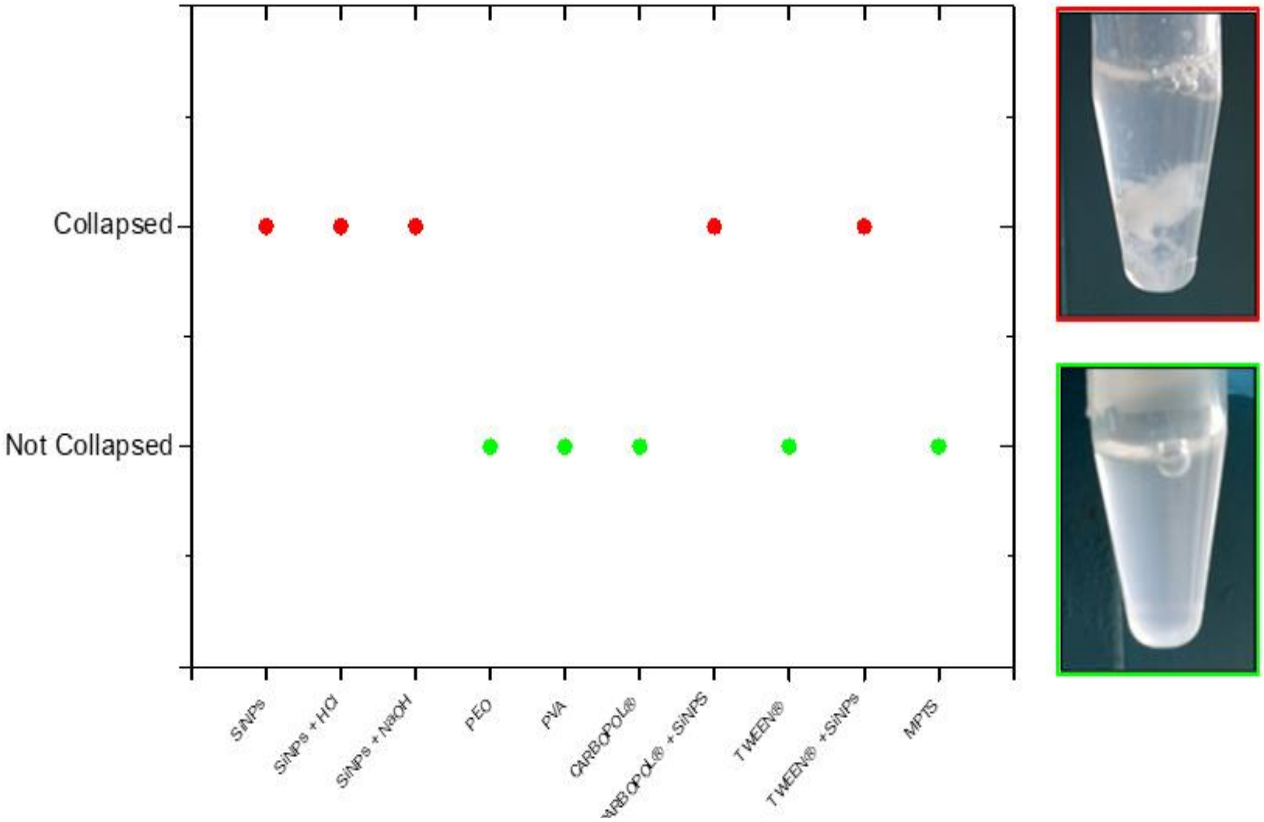

Figure 8.11: Effective state diagram of the interaction of hagfish mucin gel with different nanoparticles forming nanocomposites. With (●) are the additives that collapsed the network and with (●) are the ones where mixing was successful. Images to the right show a typical behavior of each state.

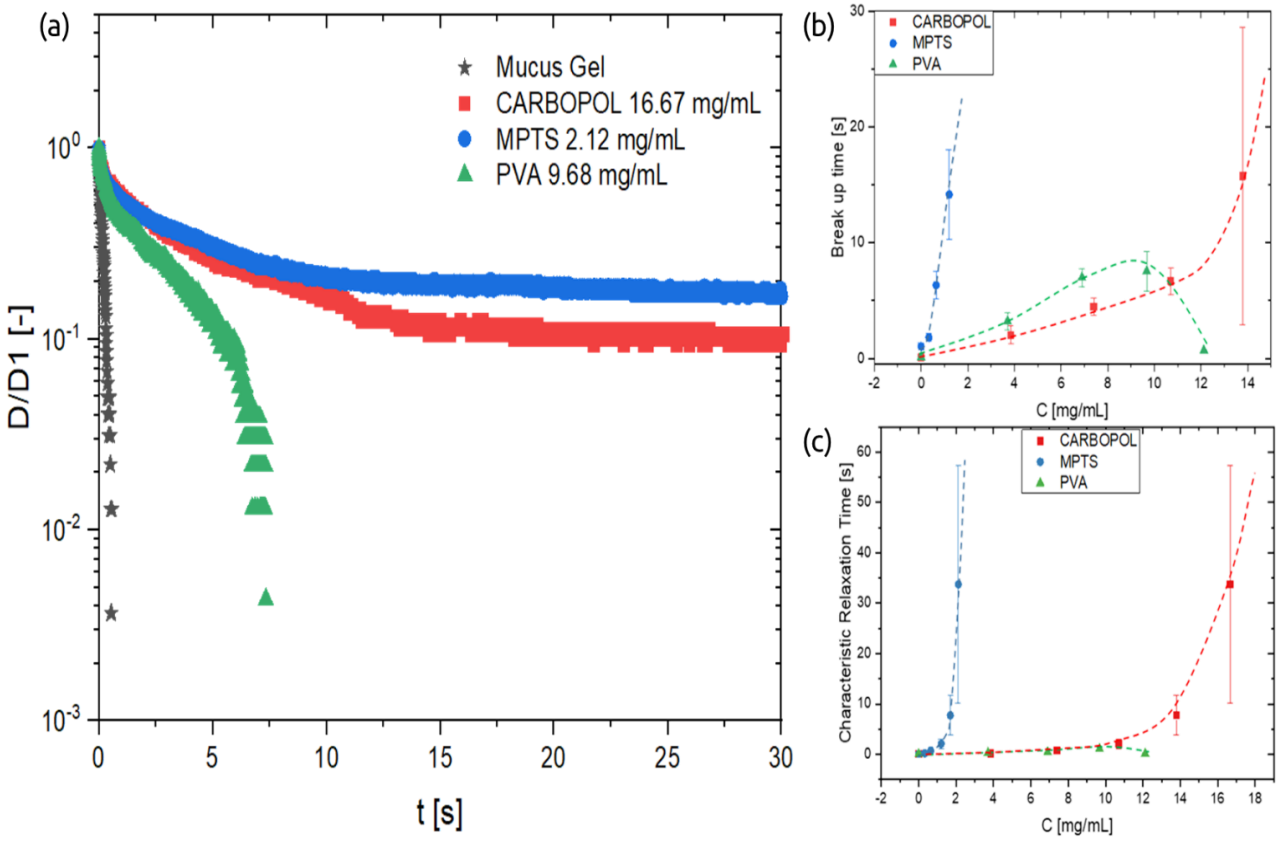

Figure 8.12: (a) Capillary breakup rheology tests of the optimal formulations for each additive and the mucus gel without additive (b) Critical break-up time of filaments with concentrations (c) Characteristic relaxation time with concentration as obtained for the elastocapillary fit. The dashed lines are a guide to the eye and they go to infinite when it the capillary is not breaking.

curves with the elastocapillary model (eq. 3.11) to extract a characteristic relaxation time (λ) of the filament. The results (Figure 8.12(b) and (c)) reveal that both breakup time (τ_B) and characteristic relaxation time (λ) increase gradually with increasing the concentration of the nanoparticle. Note that for PVA we observe a drop after a critical concentration of ~10mg/mL. Regarding the linear viscoelastic measurements, in Figure 8.13 we plot and compare the dynamic frequency spectra after equilibration. Interestingly, the MPTS organosilica particles have a weak effect at lower concentrations, which becomes significantly enhanced if we only add 1mg/mL more. Note that, much less quantities are needed for the organosilica fillers to reach significant effective strengthening. However, one should be very careful since even with very low amounts there is a formation of flaky regions and eventually phase separation and breakdown of the mucin hydrogel. In addition, these nanocomposites

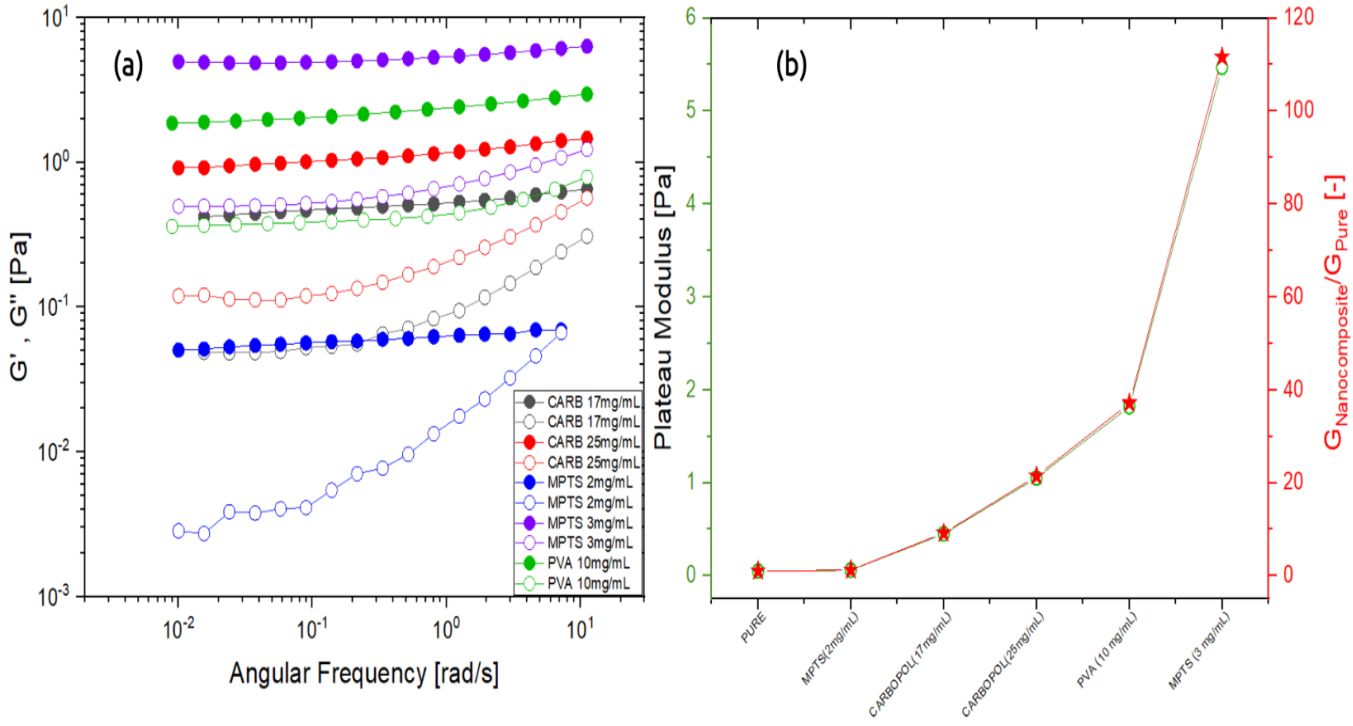

Figure 8.13: (a) Dynamic Frequency Spectra of each mucin nanocomposites studied. The test results shown were obtained after equilibration over time (b) Plateau Modulus of each mixed and also normalized by the modulus of the mucus gel used as reference.

are stable, ie, they exhibit a very steady response over time. The higher value of storage modulus was obtained for MPTS at 3mg/mL, followed by PVA at 10 mg/mL. This trend apparently contradicts the results obtained from capillary break-up rheometry. As opposed to conventional rheometers, which impose a controlled stress or strain on the fluid, a filament breakup rheometer imposes a rapid axial step strain of prescribed magnitude to induce a statically-unstable shape and then allows the necked sample to relax and break under the action of capillary forces. So we have to keep in mind that we test different mechanisms of deformation. Moreover, due to limited amounts of sample, we were not able to make a fully conclusive study regarding the latter set of experiments. Whereas this needs further investigations, the fact the strong reinforcement is possible with very small amounts of added nanoparticles and very small overall material concentration in water, represents an important, intriguing finding.

CHAPTER 9. CONCLUSIONS AND PERSPECTIVES

Associating macromolecular systems are promising building blocks for materials with tunable mechanical and rheological properties. We have shown that the simplest possible telechelic star polymers with 3 arms represent a paradigm of soft patchy particle, whose properties can be tuned by the strength of attraction between its associating terminal monomers, i.e., by selecting a solvent which is at the same time good for the inner blocks but poor for the outer ones, and then changing the system's temperature. Moreover, we have investigated the self-assembly of TSPs with a variable size of the outer block as well as the overall arm length, which are subject to worsening solvent conditions, in dilute solutions. Our DLS results show two distinct relaxation modes upon lowering the temperature below a critical value: the fast-relaxing mode that corresponds to individual stars in solution and the slow-relaxing mode due to the presence of large aggregates. We find that the size of both populations decreases upon cooling. For single TSPs, the decay is associated with the formation of a single patch, where all three arms come together. However, we find that the transition temperature increases with the degree of polymerization of TSP arms, while keeping the fraction of solvophobic monomers constant. The formed aggregates in solution are much larger than single stars. Simulations at a higher concentration of TSPs reveal the formation of micellar aggregates with complex internal structure. Upon worsening the solvent quality for the outer block, the solvent becomes more strongly expelled from the aggregate's interior, which causes the reduction of its size, similarly to the experimental behavior. TSPs with higher functionality and molecular weight are different. Interestingly, the TSP with 0.5 fraction of outer B block self-organizes at relatively low temperatures (below 30°C) and the size of the fast mode is unchanged. Yet, for the lower fraction (0.3 PS) star, we a two-step decay of the size of the fast mode results from intramolecular patches formed upon worsening the solvent quality. There is a clear indication of aggregation, reflected in the presence of the slow process which has a very broad shoulder attributed to the formation of a percolated network with no clear form factor. Finally, we studied the dynamics of 6 and 16 arm diblock-co-polymer star in a selective solvent for the outer block. Due to the difference in the position of the solvophobic block, the single molecular conformation of the $(AB)_n$ type star block is quite different from that of the (BA)n type TSP, leading to different type of aggregates. In particular, the tendency to forming

micelles and the supramolecular structures are different between in the two types. Solvophobic nanodomains serve as junction locations for forming multimolecular micelles, not a gel such as that in the case of sticky end arms. Undoubtedly, more concentrated regimes should be explored to help us understand the kinetics and dynamics of their self-organization mechanism. Also the effect of molecular weight both on the volume transition and the size and type of supramolecular clusters formed should be investigated. Rheological studies of the tunable flow properties as well as simulation studies would provide further insights for understanding the interplay of interactions and polymer dynamics and for exploiting these materials in applications. The second part of this thesis focused on the polyelectrolyte hydrogel formed from the mucin-like protein network derived from mucin vesicles of Hagfish. We demonstrated pathways to enhance their mechanical properties. We found that silica nanoparticles were not promising at all since there was a collapse of the polymeric network which led to an irreversible flaky state. Alternatively, organosilica nanoparticles were prepared and tested and indeed a strengthening effect was observed when adding even very low amounts. Our rheological studies show indeed that these particles significantly enhance the stiffness of the hydrogel and also its time stability. Notably the nanocomposite was highly heterogeneous: there was always a very small portion of the system that exhibited again similar behavior to the silica nanoparticles but this it seemed to be integrated to the gel and did not precipitate. This effects became more predominant as we increased the concentration and eventually further addition of nanoparticles yielded collapse of the nanocomposites. CARBOPOL® was also proved to be a successful additives, and the capillary filaments formed were very stable. CARBOPOL® - increased the modulus of the mucus gel but not its time stability. Finally, the use PVA to form a double network was also shown to be another promising avenue for reinforcement, however there was a limitation in the amount add since after a certain point the effect of the double network is counteracted by actual dilution of the DN system. Nevertheless, when tested the rheology of PVA/mucus with conventional oscillatory shear rheology, the results were extraordinary regarding both time stability and increase of modulus. These results are promising and will prompt many more investigations. However in lack of a clear understanding of the fillier-mucin interactions and the mechanism of reinforcement, it is not possible to identify the best reinforcing agent. To gain further insight of the effects of additives on the mucus properties, it is important to further

characterize the systems via DLS experiments to obtain information on the spatiotemporal changes and perform a more extended study with shear rheology, including nonlinear. Preliminary results of IR experiments to healthy freeze-dried mucin, as well as to a collapsed state due to high concentration of MPTS NPs, are promising since there appears to be a decrease of –OH bonding at the collapsed state indicating a more hydrophobic character. Despite this, the effect is still strong not allowing to unambiguously track other important bonding (i.e. S-S) in the single bond regime of wavelengths. NMR spectroscopy as well as imaging techniques (i.e., TEM) could help mapping the interactions between the mucin matrix and the particles. Concerning the mucoadhesive particles, better control could be achieved by incorporating chemical groups in the polymer network that have affinity to the NP precursors (nucleation groups), for example decorated with PEG. At last, inspired by our work would be possible to try reinforcing the TSPs networks utilizing the mechanisms studied for mucus hydrogel and thus create well-defined nanocomposites.

III. REFERENCES

[1] F. Brochard-Wyart, "Pierre-Gilles de Gennes (1932–2007)," *Nature*, vol. 448, no. 7150, pp. 149–149, Jul. 2007, doi: 10.1038/448149a.

[2] A. Nelson, "Stimuli-responsive polymers: Engineering interactions," *Nat. Mater.*, vol. 7, no. 7, pp. 523–525, 2008, doi: 10.1038/nmat2214.

[3] R. Liang, H. Yu, L. Wang, L. Lin, N. Wang, and K. U. R. Naveed, "Highly Tough Hydrogels with the Body Temperature-Responsive Shape Memory Effect," *ACS Appl. Mater. Interfaces*, vol. 11, no. 46, pp. 43563–43572, Nov. 2019, doi: 10.1021/acsami.9b14756.

[4] R. Elashnikov, P. Slepička, S. Rimpelova, P. Ulbrich, V. Švorčík, and O. Lyutakov, "Temperature-responsive PLLA/PNIPAM nanofibers for switchable release," *Mater. Sci. Eng. C*, vol. 72, pp. 293–300, Mar. 2017, doi: 10.1016/j.msec.2016.11.028.

[5] L. Yu, P. Si, L. Bauman, and B. Zhao, "Synergetic Combination of Interfacial Engineering and Shape-Changing Modulation for Biomimetic Soft Robotic Devices," *Langmuir*, vol. 36, no. 13, pp. 3279–3291, Apr. 2020, doi: 10.1021/acs.langmuir.9b03773.

[6] C. Bombonnel, C. Vancaeyzeele, G. Guérin, and F. Vidal, "Fabrication of bicontinuous double networks as thermal and pH stimuli responsive drug carriers for on-demand release," *Mater. Sci. Eng. C*, vol. 109, p. 110495, Apr. 2020, doi: 10.1016/j.msec.2019.110495.

[7] C. Brazzale *et al.*, "Control of targeting ligand display by pH-responsive polymers on gold nanoparticles mediates selective entry into cancer cells," *Nanoscale*, vol. 9, no. 31, pp. 11137–11147, Aug. 2017, doi: 10.1039/c7nr02595e.

[8] J. Su, F. Chen, V. L. Cryns, and P. B. Messersmith, "Catechol polymers for pH-responsive, targeted drug delivery to cancer cells," *J. Am. Chem. Soc.*, vol. 133, no. 31, pp. 11850–11853, Aug. 2011, doi: 10.1021/ja203077x.

[9] M. E. Lee and A. M. Armani, "Flexible UV Exposure Sensor Based on UV Responsive Polymer," *ACS Sensors*, vol. 1, no. 10, pp. 1251–1255, 2016, doi: 10.1021/acssensors.6b00491.

[10] P. Han *et al.*, "UV-responsive polymeric superamphiphile based on a complex of malachite green derivative and a double hydrophilic block copolymer," *Langmuir*, vol. 27, no. 23, pp. 14108–14111, Dec. 2011, doi: 10.1021/la203486q.

[11] C. Hörenz, K. Bertula, T. Tiainen, S. Hietala, V. Hynninen, and O. Ikkala, "UV-Triggered On-Demand Temperature-Responsive Reversible and Irreversible Gelation of Cellulose Nanocrystals," *Biomacromolecules*, vol. 21, no. 2, pp. 830–838, Feb. 2020, doi: 10.1021/acs.biomac.9b01519.

[12] S. Biffi, R. Cerbino, G. Nava, F. Bomboi, F. Sciortino, and T. Bellini, "Equilibrium gels of low-valence DNA nanostars: A colloidal model for strong glass formers," *Soft Matter*, vol. 11, no. 16, pp. 3132–3138, Apr. 2015, doi: 10.1039/c4sm02144d.

[13] C. A. Mirkin, R. L. Letsinger, R. C. Mucic, and J. J. Storhoff, "A DNA-based method for rationally assembling nanoparticles into macroscopic materials," *Nature*, vol. 382, no. 6592, pp. 607–609, Aug. 1996, doi: 10.1038/382607a0.

[14] S. Angioletti-Uberti, B. M. Mognetti, and D. Frenkel, “Re-entrant melting as a design principle for DNA-coated colloids,” *Nat. Mater.*, vol. 11, no. 6, pp. 518–522, Jun. 2012, doi: 10.1038/nmat3314.

[15] R. Dreyfus *et al.*, “Simple quantitative model for the reversible association of DNA coated colloids,” *Phys. Rev. Lett.*, vol. 102, no. 4, p. 048301, Jan. 2009, doi: 10.1103/PhysRevLett.102.048301.

[16] R. A. Cone, “Barrier properties of mucus,” *Advanced Drug Delivery Reviews*, vol. 61, no. 2. Elsevier, pp. 75–85, 27-Feb-2009, doi: 10.1016/j.addr.2008.09.008.

[17] M. E. V. Johansson and G. C. Hansson, “Immunological aspects of intestinal mucus and mucins,” *Nature Reviews Immunology*, vol. 16, no. 10. Nature Publishing Group, pp. 639–649, 01-Oct-2016, doi: 10.1038/nri.2016.88.

[18] R. W. Style, L. Isa, and E. R. Dufresne, “Adsorption of soft particles at fluid interfaces,” *Soft Matter*, vol. 11, no. 37, pp. 7412–7419, Aug. 2015, doi: 10.1039/c5sm01743b.

[19] D. Vlassopoulos and M. Cloitre, “Tunable rheology of dense soft deformable colloids,” *Current Opinion in Colloid and Interface Science*. 2014, doi: 10.1016/j.cocis.2014.09.007.

[20] F. Lo Verso and C. N. Likos, “End-functionalized polymers: Versatile building blocks for soft materials,” *Polymer*, vol. 49, no. 6. Elsevier BV, pp. 1425–1434, 17-Mar-2008, doi: 10.1016/j.polymer.2007.11.051.

[21] Y. Tsukahara and K. Adachi, “T Telechelic Polymer: Preparation and Application,” doi: 10.1007/978-3-642-29648-2.

[22] M. Szwarc, “‘Living’ polymers,” *Nature*, vol. 178, no. 4543, pp. 1168–1169, 1956, doi: 10.1038/1781168a0.

[23] T. J. Kealy and P. L. Pauson, “A new type of organo-iron compound,” *Nature*, vol. 168, no. 4285. Nature Publishing Group, pp. 1039–1040, 1951, doi: 10.1038/1681039b0.

[24] C. A. Uraneck, H. L. Hsieh, and O. G. Buck, “Telechelic polymers,” *J. Polym. Sci.*, vol. 46, no. 148, pp. 535–539, Oct. 1960, doi: 10.1002/pol.1960.1204614825.

[25] M. Pitsikalis, N. Hadjichristidis, and J. W. Mays, “Model mono-, di-, and tri-ω-functionalized three-arm star polybutadienes. Association behavior in dilute solution by dynamic light scattering and viscometry,” *Macromolecules*, vol. 29, no. 1, pp. 179–184, Jan. 1996, doi: 10.1021/ma951001s.

[26] G. Broze, R. Jérôme, and P. Teyssié, “Halato-Telechelic Polymers. 4. Synthesis and Dilute-Solution Behavior,” *Macromolecules*, vol. 15, no. 3, pp. 920–927, May 1982, doi: 10.1021/ma00231a044.

[27] A. Salazar, *Advanced Chordate Zoology - Aubrey Salazar - Βιβλία Google*, 1st ed. ED-TECH PRESS, 2018.

[28] J. Varner, P. Neame, and G. W. Litman, “A serum heterodimer from hagfish (Eptatretus stoutii) exhibits structural similarity and partial sequence identity with immunoglobulin.,” *Proc. Natl. Acad. Sci. U. S. A.*, vol. 88, no. 5, pp. 1746–50, Mar. 1991, doi: 10.1073/pnas.88.5.1746.

[29] M. Reinecke, “Substance P is a vasoactive hormone in the atlantic hagfish Myxine glutinosa (Cyclostomata),” *Gen. Comp. Endocrinol.*, vol. 66, no. 2, pp. 291–296, May 1987, doi: 10.1016/0016-6480(87)90279-6.

[30] R. H. Spitzer and E. A. Koch, “Hagfish Skin and Slime Glands,” in *The Biology of Hagfishes*, Dordrecht: Springer Netherlands, 1998, pp. 109–132.

[31] V. Zintzen, C. D. Roberts, M. J. Anderson, A. L. Stewart, C. D. Struthers, and E. S. Harvey, “Hagfish predatory behaviour and slime defence mechanism,” *Sci. Rep.*, vol. 1, no. 1, p. 131, Dec. 2011, doi: 10.1038/srep00131.

[32] B. Fernholm, “Thread Cells from the Slime Glands of Hagfish (Myxinidae),” *Acta Zool.*, vol. 62, no. 3, pp. 137–145, Sep. 1981, doi: 10.1111/j.1463-6395.1981.tb00623.x.

[33] “Cyclostomes: Origin and Habitat | Vertebrates | Chordata | Zoology.” [Online]. Available: http://www.notesonzoology.com/phylum-chordata/cyclostomes/cyclostomes-origin-and-habitat-vertebrates-chordata-zoology/7873. [Accessed: 02-Dec-2019].

[34] L. Böni, P. Fischer, L. Böcker, S. Kuster, and P. A. Rühs, “Hagfish slime and mucin flow properties and their implications for defense,” *Sci. Rep.*, vol. 6, no. 1, p. 30371, Sep. 2016, doi: 10.1038/srep30371.

[35] J. M. Coles, D. P. Chang, and S. Zauscher, “Molecular mechanisms of aqueous boundary lubrication by mucinous glycoproteins,” *Curr. Opin. Colloid Interface Sci.*, vol. 15, no. 6, pp. 406–416, Dec. 2010, doi: 10.1016/J.COCIS.2010.07.002.

[36] X. Yang *et al.*, “Immobilization of Pseudorabies Virus in Porcine Tracheal Respiratory Mucus Revealed by Single Particle Tracking,” *PLoS One*, vol. 7, no. 12, p. e51054, Dec. 2012, doi: 10.1371/journal.pone.0051054.

[37] E. J. Herr, M. A. Clifford, G. G. Goss, and S. D. Fudge, “Defensive slime formation in Pacific hagfish requires Ca2+ aquaporin-mediated swelling of released mucin vesicles,” *J. Exp. Biol.*, vol. 217, pp. 2288–2296, 2014.

[38] L. J. Böni *et al.*, “Hagfish slime exudate stabilization and its effect on slime formation and functionality.,” *Biol. Open*, vol. 6, no. 7, pp. 1115–1122, Jul. 2017, doi: 10.1242/bio.025528.

[39] K. Rementzi, L. J. Böni, J. Adamcik, P. Fischer, and D. Vlassopoulos, “Structure and dynamics of hagfish mucin in different saline environments,” *Soft Matter*, vol. 15, no. 42, pp. 8627–8637, Oct. 2019, doi: 10.1039/C9SM00971J.

[40] K. Dušek and W. Prins, “Structure and elasticity of non-crystalline polymer networks,” in *Fortschritte der Hochpolymeren-Forschung*, Springer-Verlag, 2006, pp. 1–102.

[41] A. R. Reeves and M. Rutten, “meric dielectric materials and polymers having nonlinear optical properties,” 1988.

[42] J. P. Gong, Y. Katsuyama, T. Kurokawa, and Y. Osada, “Double-Network Hydrogels with Extremely High Mechanical Strength,” *Adv. Mater.*, vol. 15, no. 14, pp. 1155–1158, Jul. 2003, doi: 10.1002/adma.200304907.

[43] J. P. Gong, “Why are double network hydrogels so tough?,” *Soft Matter*, vol. 6, no. 12, p. 2583, Jun. 2010, doi: 10.1039/b924290b.

[44] T. L. Sun *et al.*, “Physical hydrogels composed of polyampholytes demonstrate high toughness and viscoelasticity,” *Nat. Mater.*, vol. 12, no. 10, pp. 932–937, Oct. 2013, doi: 10.1038/nmat3713.

[45] M. Rubinstein, R. H. Colby, A. V Dobrynin, and J.-F. Joanny, “Elastic Modulus and Equilibrium Swelling of Polyelectrolyte Gels,” 1996.

[46] R. Takahashi *et al.*, “Coupled instabilities of surface crease and bulk bending during fast free swelling of hydrogels,” *Soft Matter*, vol. 12, no. 23, pp. 5081–5088, Jun. 2016, doi: 10.1039/c6sm00578k.

[47] J. B. Thompson, J. H. Kindt, B. Drake, H. G. Hansma, D. E. Morse, and P. K. Hansma, “Bone indentation recovery time correlates with bond reforming time,” *Nature*, vol. 414, no. 6865, pp. 773–776, Dec. 2001, doi: 10.1038/414773a.

[48] G. E. Fantner *et al.*, “Sacrificial bonds and hidden length dissipate energy as mineralized fibrils separate during bone fracture,” *Nat. Mater.*, vol. 4, no. 8, pp. 612–616, Aug. 2005, doi: 10.1038/nmat1428.

[49] J. P. Gong, Y. Katsuyama, T. Kurokawa, and Y. Osada, “Double-Network Hydrogels with Extremely High Mechanical Strength,” *Adv. Mater.*, vol. 15, no. 14, pp. 1155–1158, Jul. 2003, doi: 10.1002/adma.200304907.

[50] “Editorial: ‘Plenty of room’ revisited,” *Nat. Nanotechnol.*, vol. 4, no. 12, p. 781, 2009, doi: 10.1038/nnano.2009.356.

[51] B. Pukánszky and E. Fekete, “Adhesion and surface modification,” *Adv. Polym. Sci.*, vol. 139, pp. 109–153, 1999, doi: 10.1007/3-540-69220-7_3.

[52] E. Guth, “Theory of Filler Reinforcement,” *Rubber Chem. Technol.*, vol. 18, no. 3, pp. 596–604, Sep. 1945, doi: 10.5254/1.3546754.

[53] A. A. Gavrilov, A. V. Chertovich, P. G. Khalatur, and A. R. Khokhlov, “Study of the mechanisms of filler reinforcement in elastomer nanocomposites,” *Macromolecules*, vol. 47, no. 15, pp. 5400–5408, Aug. 2014, doi: 10.1021/ma500947g.

[54] R. Everaers and K. Kremer, “Communications to the Editor Test of the Foundations of Classical Rubber Elasticity,” 1995.

[55] M. Vacatello, “Monte Carlo simulations of polymer melts filled with solid nanoparticles,” *Macromolecules*, vol. 34, no. 6, pp. 1946–1952, Mar. 2001, doi: 10.1021/ma0015370.

[56] G. D. Smith, D. Bedrov, L. Li, and O. Byutner, “Perspective: Outstanding theoretical questions in polymer-nanoparticle hybrids,” *J. Chem. Phys.*, vol. 117, p. 20901, 2002, doi: 10.1063/1.1516589.

[57] S. W. Provencher, “A constrained regularization method for inverting data represented by linear algebraic or integral equations,” *Comput. Phys. Commun.*, vol. 27, no. 3, pp. 213–227, Sep. 1982, doi: 10.1016/0010-4655(82)90173-4.

[58] S. W. Provencher, “Inverse problems in polymer characterization : direcr analysis of polydispersity with photon correlation spectroscopy,” *Die Makromol. Chemie und Phys.*, 1979.

[59] A. Scotti *et al.*, “The CONTIN algorithm and its application to determine the size distribution of microgel suspensions,” *J. Chem. Phys.*, vol. 142, no. 23, p. 234905, Jun. 2015, doi: 10.1063/1.4921686.

[60] H.-H. Perkampus, *UV-VIS Spectroscopy and Its Applications*. Springer Berlin Heidelberg, 1992.

[61] Q. Huang, “Basic Principles of Spectroscopy,” RUTGERTS , New Jershey, 2013.

[62] R. W. Ricci, M. Ditzler, and L. P. Nestor, “Discovering the Beer-Lambert Law,” *J. Chem. Educ.*, vol. 71, no. 11, p. 983, 1994, doi: 10.1021/ED071P983.

[63] D. . Swinehart, “The Beer-Lambert Law,” *J. Chem. Educ.*, vol. 39, no. 7, pp. 333–335, 1962.

[64] A. Townshen, *Principles of Instrumental Analysis*, vol. 152. 1983.

[65] R. H. Spitzer, S. W. Downing, E. A. Koch, W. L. Salo, and L. J. Saidel, “Hagfish slime gland thread cells. II. Isolation and characterization of intermediate filament components associated with the thread,” *J. Cell Biol.*, vol. 98, no. 2, pp. 670–677, 1984, doi: 10.1083/jcb.98.2.670.

[66] K. Rementzi, “Rheology and dynamics of tunable soft materials: from synthetic microgels to biological hydrogels,” 2019.

[67] R. J. Hunter, *Zeta potential in colloid science : principles and applications*. .

[68] J. D. Clogston and A. K. Patri, *Zeta Potential Measurement : Characterization of Nanoparticles Intended for Drug Delivery*. Humana Press, 2011.

[69] M. V. Smoluchowski, “‘Contribution to the theory of electro-osmosis and related phenomena.,’” *Bull Int Acad Sci Cracovie*, vol. 3, pp. 184–199, 1903.

[70] M. Rubinstein and R. H. Colby, *Polymer Physics - - Google Books*. OUP Oxford, 2003.

[71] Thomas G. Mezger, *Applied Rheology: With Joe Flow on Rheology Road*, 2nd ed. Anton Paar GmbH, 2018.

[72] R. M. L. Evans, M. Tassieri, D. Auhl, and T. A. Waigh, “Direct conversion of rheological compliance measurements into storage and loss moduli,” *Phys. Rev. E - Stat. Nonlinear, Soft Matter Phys.*, vol. 80, no. 1, p. 012501, Aug. 2009, doi: 10.1103/PhysRevE.80.012501.

[73] G. H. McKinley and A. Tripathi, “How to extract the Newtonian viscosity from capillary breakup measurements in a filament rheometer,” *J. Rheol. (N. Y. N. Y).*, vol. 653, no. 44, p. 2000, 2000.

[74] V. Sharma, A. M. Arezoo, and G. H. McKinley, “‘Beads on a String’ Structures and Extensional Rheometry using Jet Break-up.”

[75] E. J. Herr, T. M. Winegard, M. . J. O’Donnell, P. H. Yancey, and D. . Fudge, “Stabilization and Swelling of Hagfish Slime Mucin Vesicles,” *J. Exp. Biol.*, vol. 213, no. 7, pp. 1092–1099, Aug. 2010, doi: 10.1242/jeb.01730.

[76] J. E. Herr, A. M. Clifford, G. G. Goss, and D. S. Fudge, “Defensive slime formation in Pacific hagfish requires Ca2+-] and aquaporinmediated swelling of released mucin vesicles,” *J. Exp. Biol.*, vol. 217, no. 13, pp. 2288–2296, Jul. 2014, doi: 10.1242/jeb.101584.

[77] W. L. Salo, S. W. Downing, W. A. Lidinsky, W. H. Gallagher, R. H. Spitzer, and E. A. Koch, “Fractionation of Hagfish Slime Gland Secretions: Partial Characterization of the Mucous Vesicle Fraction,” *Prep. Biochem.*, vol. 13, no. 2, pp. 103–135, Jul. 1983, doi: 10.1080/00327488308068743.

[78] HORIBA, “Technical Note Reference Materials: Colloidal Silica as a particle size and charge reference material.”

[79] F. Auriemma, C. De Rosa, and R. Triolo, “Slow Crystallization Kinetics of Poly(vinyl alcohol) in Confined Environment during Cryotropic Gelation of Aqueous Solutions,” 2006, doi: 10.1021/ma061955q.

[80] D. Thomas and P. Cebe, “Self-nucleation and crystallization of polyvinyl alcohol,” *J. Therm. Anal. Calorim.*, vol. 127, no. 1, pp. 885–894, Jan. 2017, doi: 10.1007/s10973-016-5811-1.

[81] G. S. Irmukhametova, G. A. Mun, and V. V. Khutoryanskiy, “Thiolated Mucoadhesive and PEGylated Nonmucoadhesive Organosilica Nanoparticles from 3-Mercaptopropyltrimethoxysilane,” *Langmuir*, vol. 27, no. 15, pp. 9551–9556, Aug. 2011, doi: 10.1021/la201385h.

[82] M. Nakamura, A. Awaad, K. Hayashi, K. Ochiai, and K. Ishimura, “Thiol-organosilica particles internally functionalized with propidium iodide as a multicolor fluorescence and x-ray computed tomography probe and application for non-invasive functional gastrointestinal tract imaging,” *Chem. Mater.*, vol. 24, no. 19, pp. 3772–3779, Oct. 2012, doi: 10.1021/cm3023677.

[83] J. H. Al Mahrooqi, E. A. Mun, A. C. Williams, and V. V. Khutoryanskiy, “Controlling the Size of Thiolated Organosilica Nanoparticles,” *Langmuir*, vol. 34, no. 28, pp. 8347–8354, Jul. 2018, doi: 10.1021/acs.langmuir.8b01556.

[84] R. Zurflüh, “Isolation and characterization and hagfish mucin,” 2016.

[85] L. J. Böni, “Biophysics and Biomimetics of Hagfish Slime,” ETH Zurich, 2018.

[86] F. Lo Verso, C. N. Likos, C. Mayer, and H. Löwen, “Collapse of telechelic star polymers to watermelon structures,” *Phys. Rev. Lett.*, vol. 96, no. 18, p. 187802, May 2006, doi: 10.1103/PhysRevLett.96.187802.

[87] L. Rovigatti, B. Capone, and C. N. Likos, “Soft self-assembled nanoparticles with temperature-dependent properties,” *Nanoscale*, vol. 8, no. 6, pp. 3288–3295, Feb. 2016, doi: 10.1039/c5nr04661k.

[88] S. Qian, R. Liu, G. Han, K. Shi, and W. Zhang, “Star amphiphilic block copolymers: Synthesis: via polymerization-induced self-assembly and crosslinking within nanoparticles, and solution and interfacial properties,” *Polym. Chem.*, vol. 11, no. 14, pp. 2532–2541, Apr. 2020, doi: 10.1039/c9py01656b.

[89] Y. Zhang, T. Guan, G. Han, T. Guo, and W. Zhang, “Star Block Copolymer Nanoassemblies: Block Sequence is All-Important,” *Macromolecules*, vol. 52, no. 2, pp. 718–728, Jan. 2019, doi: 10.1021/acs.macromol.8b02427.

[90] E. Moghimi *et al.*, “Self-Organization and Flow of Low-Functionality Telechelic Star Polymers with Varying Attraction,” *ACS Macro Lett.*, vol. 8, no. 7, pp. 766–772, 2019, doi: 10.1021/acsmacrolett.9b00211.

[91] B. Capone, I. Coluzza, F. Loverso, C. N. Likos, and R. Blaak, “Telechelic star polymers as self-assembling units from the molecular to the macroscopic scale,” *Phys. Rev. Lett.*, vol. 109, no. 23, p. 238301, Dec. 2012, doi: 10.1103/PhysRevLett.109.238301.

[92] J. Yang, R. Wang, and D. Xie, “Self-organization in suspensions of telechelic star polymers,” *Polymer (Guildf).*, vol. 205, p. 122866, Aug. 2020, doi: 10.1016/j.polymer.2020.122866.

[93] E. Moghimi, G. Polymeropoulos, N. Hadjichristidis, and C. N. Likos, “The influence of arm composition on the self-assembly of low-functionality telechelic star polymers in dilute solutions,” *Polym. Colloid Sci.*, 2020.

[94] L. Rovigatti, B. Capone, and C. N. Likos, “Soft self-assembled nanoparticles with temperature-dependent properties,” *Nanoscale*, vol. 8, no. 6, pp. 3288–3295, Feb. 2016, doi: 10.1039/c5nr04661k.

[95] B. Capone, I. Coluzza, F. Loverso, C. N. Likos, and R. Blaak, “Telechelic star polymers as self-assembling units from the molecular to the macroscopic scale,” *Phys. Rev. Lett.*, vol. 109, no.

23, p. 238301, Dec. 2012, doi: 10.1103/PhysRevLett.109.238301.

[96] I. C. Ga, D. Jaramillo-cano, and C. N. Likos, “Self-organization of gel networks formed by block copolymer stars,” pp. 29–38, 2019, doi: 10.1039/c9sm00111e.

[97] F. Lo Verso, C. N. Likos, C. Mayer, and H. Löwen, “Collapse of telechelic star polymers to watermelon structures,” *Phys. Rev. Lett.*, vol. 96, no. 18, p. 187802, May 2006, doi: 10.1103/PhysRevLett.96.187802.

[98] A. B. Nguyen, N. Hadjichristidis, and L. J. Fetters, “) Bank, M.; Leffingwell, J.; Thies, C. Macromolecules 1971, 4, 43,” Cornell Uni-versity Press, 1986.

[99] N. Hadjichristidis and J. Roovers, “Conformation of poly(isoprene-gstyrene) in dilute solution,” *J. Polym. Sci. Polym. Phys. Ed.*, vol. 16, no. 5, pp. 851–858, May 1978, doi: 10.1002/pol.1978.180160510.

[100] P. Stephen W., “CONTIN: A GENARAL PURPOSE CONSTRAINED REGULARIZATION PROGRAM FOR INVERTING NOISY LINEAR ALGEBRAIC AND INTEGRAL EQUATIONS,” *Comput. Phys. Commun.*, vol. 27, pp. 229–242, 1982.

[101] J. Pablo Hinestrosa, David Uhrig, D. L. Pickel, J. W. Mays, and S. M. K. II, “Hydrodynamics of polystyrene– polyisoprene miktoarm star copolymers in a selective and a non-selective solvent,” *Soft Matter*, vol. 8, no. 39, pp. 10061–10071, Sep. 2012, doi: 10.1039/C2SM25882J.

[102] Y. J. Sheng, C. H. Nung, and H. K. Tsao, “Morphologies of star-block copolymers in dilute solutions,” *J. Phys. Chem. B*, vol. 110, no. 43, pp. 21643–21650, 2006, doi: 10.1021/jp0642950.

[103] F. Lo Verso, A. Z. Panagiotopoulos, and C. N. Likos, “Aggregation phenomena in telechelic star polymer solutions,” doi: 10.1103/PhysRevE.79.010401.

[104] G. J. Strous and J. Dekker, “Mucin-type glycoproteins,” *Crit. Rev. Biochem. Mol. Biol.*, vol. 27, no. 1–2, pp. 57–92, 1992, doi: 10.3109/10409239209082559.

[105] S. Jafari Daghlian Sofla, L. A. James, and Y. Zhang, “Insight into the stability of hydrophilic silica nanoparticles in seawater for Enhanced oil recovery implications,” *Fuel*, vol. 216, pp. 559–571, Mar. 2018, doi: 10.1016/J.FUEL.2017.11.091.

[106] A. A. Keller *et al.*, “Stability and Aggregation of Metal Oxide Nanoparticles in Natural Aqueous Matrices,” *Environ. Sci. Technol.*, vol. 44, no. 6, pp. 1962–1967, Mar. 2010, doi: 10.1021/es902987d.

[107] J. Y. Lock, T. L. Carlson, C.-M. Wang, A. Chen, and R. L. Carrier, “Acute Exposure to Commonly Ingested Emulsifiers Alters Intestinal Mucus Structure and Transport Properties,” *Sci. Rep.*, vol. 8, no. 1, p. 10008, Dec. 2018, doi: 10.1038/s41598-018-27957-2.

[108] E. Y. T. Chen, Y.-C. Wang, C.-S. Chen, and W.-C. Chin, “Functionalized positive nanoparticles reduce mucin swelling and dispersion.,” *PLoS One*, vol. 5, no. 11, p. e15434, Nov. 2010, doi: 10.1371/journal.pone.0015434.

[109] E. Guth, “Theory of Filler Reinforcement,” *Rubber Chem. Technol.*, vol. 18, no. 3, pp. 596–604, Sep. 1945, doi: 10.5254/1.3546754.

[110] S. Fu, Z. Sun, P. Huang, Y. Li, and N. Hu, “Some basic aspects of polymer nanocomposites: A critical review,” *Nano Mater. Sci.*, vol. 1, no. 1, pp. 2–30, Mar. 2019, doi: 10.1016/j.nanoms.2019.02.006.

[111] D. M., E. Guillaume, and C. Chivas-Joly, “Properties of Nanofillers in Polymer,” in

Nanocomposites and Polymers with Analytical Methods, InTech, 2011.

[112] T. M. Ways, W. Lau, and V. Khutoryanskiy, “Chitosan and Its Derivatives for Application in Mucoadhesive Drug Delivery Systems,” *Polymers (Basel).*, vol. 10, no. 3, p. 267, Mar. 2018, doi: 10.3390/polym10030267.

[113] T. M. M. Ways, W. M. Lau, K. W. Ng, and V. V. Khutoryanskiy, “Synthesis of thiolated, PEGylated and POZylated silica nanoparticles and evaluation of their retention on rat intestinal mucosa in vitro,” *Eur. J. Pharm. Sci.*, vol. 122, pp. 230–238, Sep. 2018, doi: 10.1016/j.ejps.2018.06.032.

[114] C. Pellet and M. Cloitre, “The glass and jamming transitions of soft polyelectrolyte microgel suspensions,” *Soft Matter*, vol. 12, no. 16, pp. 3710–3720, Apr. 2016, doi: 10.1039/c5sm03001c.

[115] S. M. Ha, W. Yuan, Q. Pei, R. Pelrine, and S. Stanford, “Interpenetrating Polymer Networks for High-Performance Electroelastomer Artificial Muscles,” *Adv. Mater.*, vol. 18, no. 7, pp. 887–891, Apr. 2006, doi: 10.1002/adma.200502437.

[116] M. S. Khan, A. Shakoor, and J. Nisar, “Conductance study of poly(ethylene oxide)- and poly(propylene oxide)-based polyelectrolytes,” *Ionics (Kiel).*, vol. 16, no. 6, pp. 539–542, Jul. 2010, doi: 10.1007/s11581-010-0424-3.

[117] S. Jiang, S. Liu, and W. Feng, “PVA hydrogel properties for biomedical application,” *J. Mech. Behav. Biomed. Mater.*, vol. 4, no. 7, pp. 1228–1233, Oct. 2011, doi: 10.1016/j.jmbbm.2011.04.005.

[118] U. Fumio, Y. Hiroshi, N. Kumiko, N. Sachihiko, S. Kenji, and M. Yasunori, “Swelling and mechanical properties of poly(vinyl alcohol) hydrogels,” *Int. J. Pharm.*, vol. 58, no. 2, pp. 135–142, Jan. 1990, doi: 10.1016/0378-5173(90)90251-X.

IV. APPENDIX I: TELECHELIC STAR POLYMERS

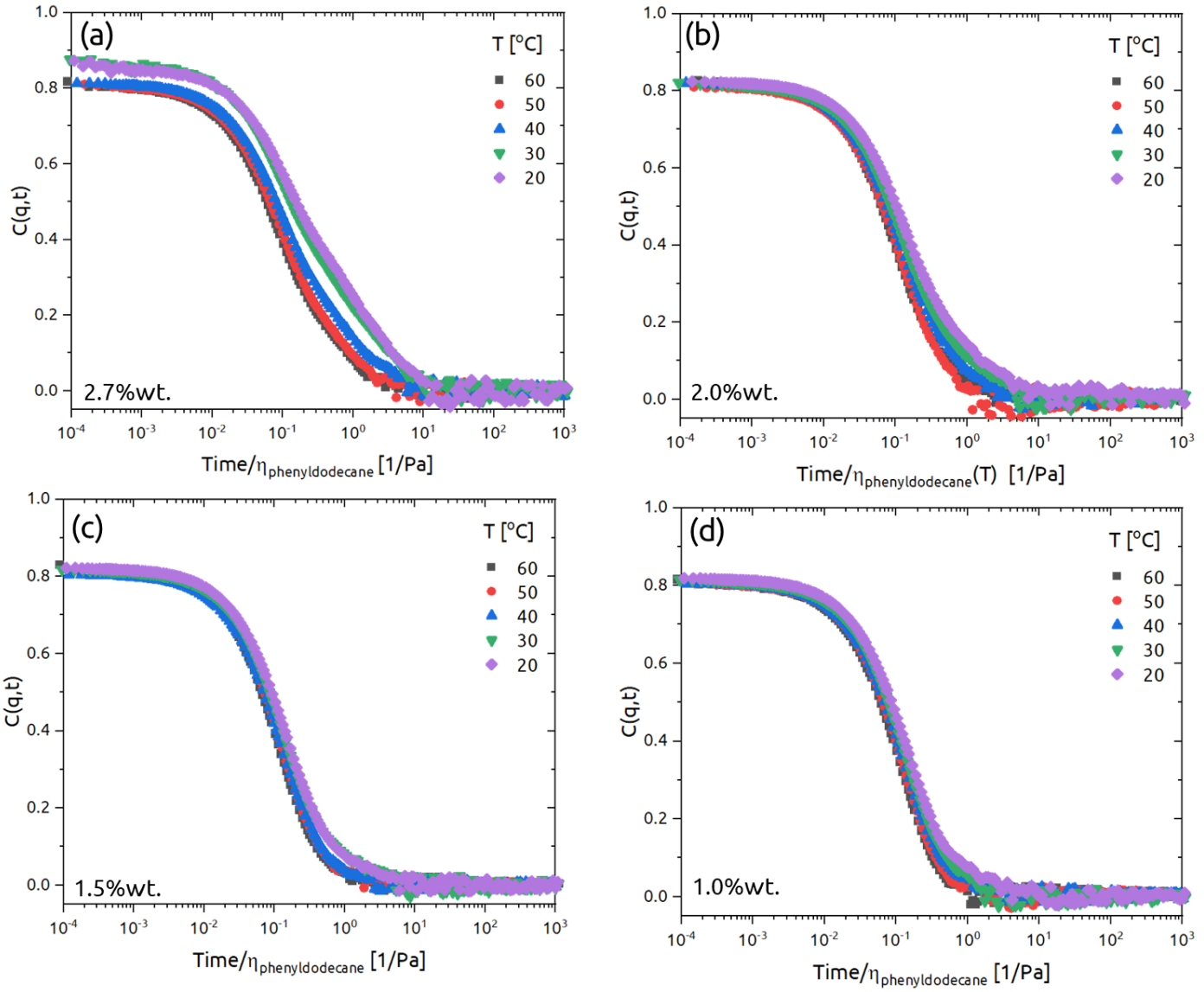

Figure AI.1: Experimental ISFs for a 16-arm TSP with α (PS) =0.5 at fixed value of the scattering wave vector (q = 0.02475 nm^{-1}). The temperature-dependent viscosity effect of the solvent is accounted for. Four different concentrations are shown (a) 2.7%wt. (b) 2.0%wt. (c) 1.5%wt. and (d) 1.0%wt.

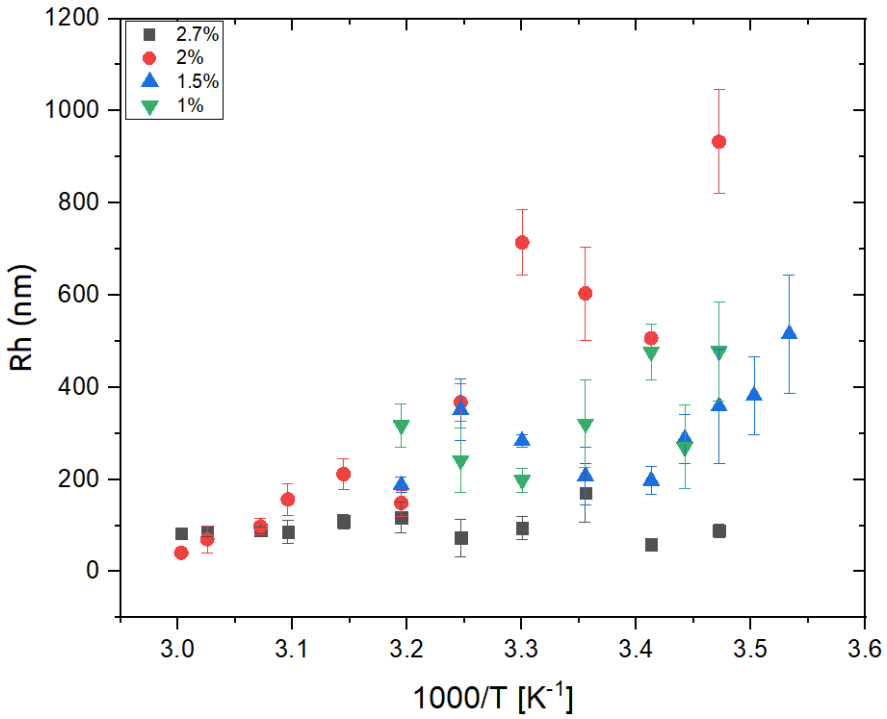

Figure A.I.2: Hydrodynamic radius extracted from the slow mode of the experimental ISFs for 16-arm TSP with α (PS) =0.49 and Mw=835,200 g/mol. Data for four different concentrations are shown.

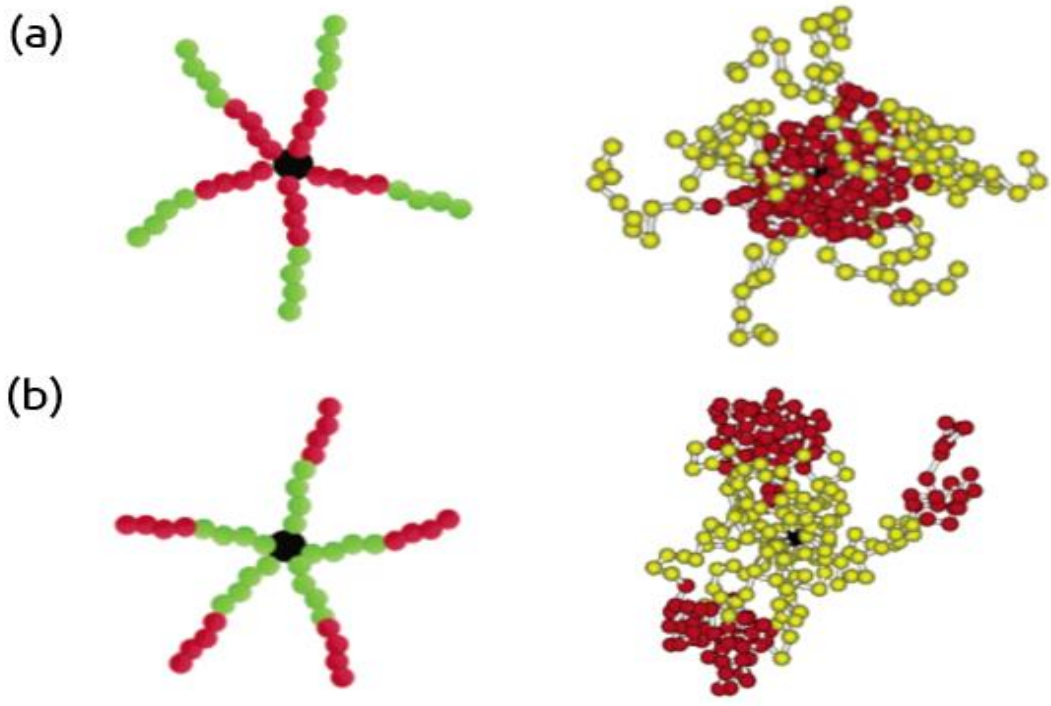

Figure AI.3: Left; schematic illustrations of star-block copolymers (a) $(BA)_n$ type and (b) $(AB)_n$ type. For simplicity, a star with 5 arms is shown. The green beads represent the solvophilic A and red beads the solvophobic B. The black bead is the center (core) of the star. Right; Snapshots taken from DPD simulations in nonselective solvent for yellow/green beads for n=14. These cartoons are taken from Sheng *et al.*, J.Phys.Chem, 2006.

V. APPENDIX II: HAGFISH

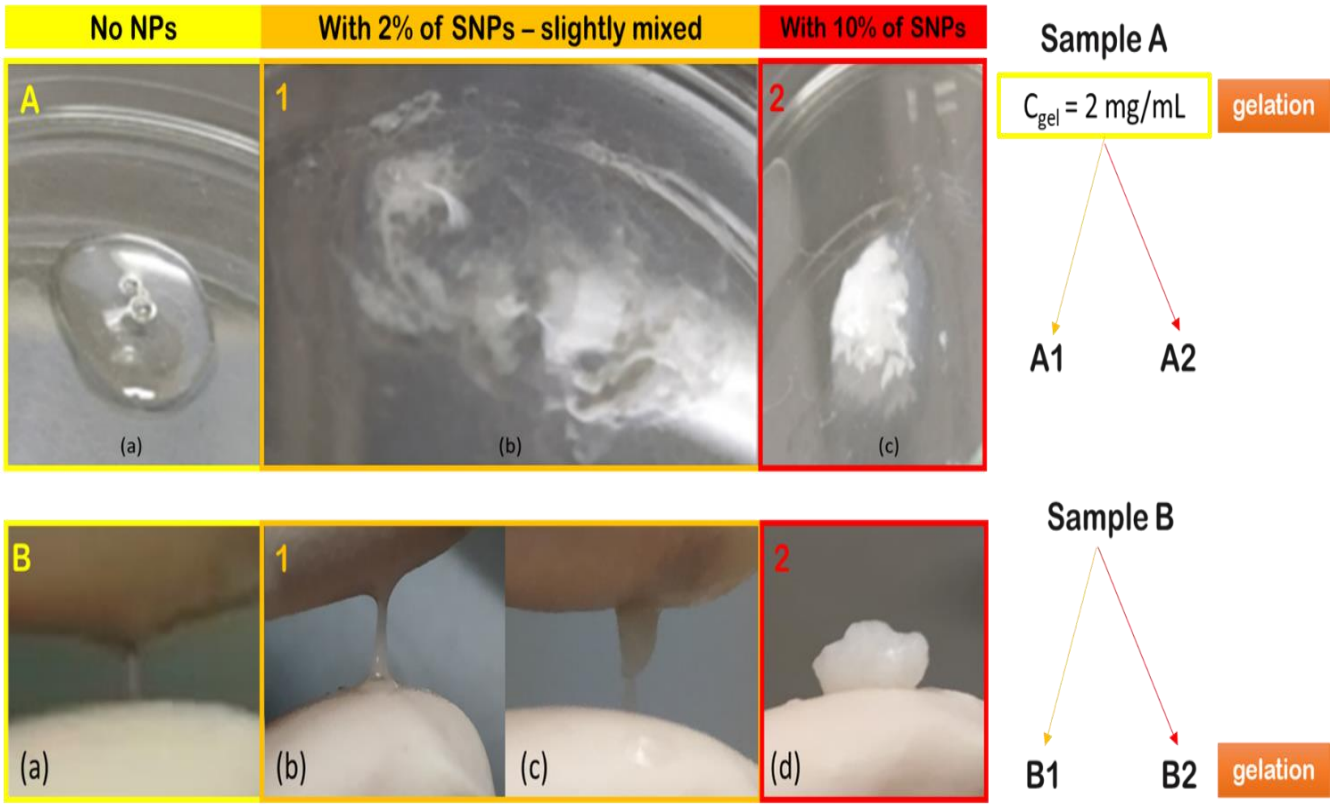

Figure AII.1: (A) Photos of the slime after mixing. In sample A series first, we formed the gel and then added the silica nano-fillers. In all samples the $m_{vesicles}$ was 0.945 mg and the total volume is V_{TOT}= 250µL (a) Non-Dialyzed slime (b) A1=2% SNPs (c) A2=10%SNPs. (B) Finger test for capillary formation check. In sample B series the sample was loaded in the Eppendorf and then sloshed to form a macroscopically homogeneous gel.(a) hagfish slime (b) B1: 2% SNPs (c) B1 : 2% SNPs after the bottom and top plates came to contact (d)B2: 10% SNPs, where one can clearly see its "gummy-like" appearance. Note that in series B there was plenty of dispersant left in the mixing Eppendorf due to phase separation.

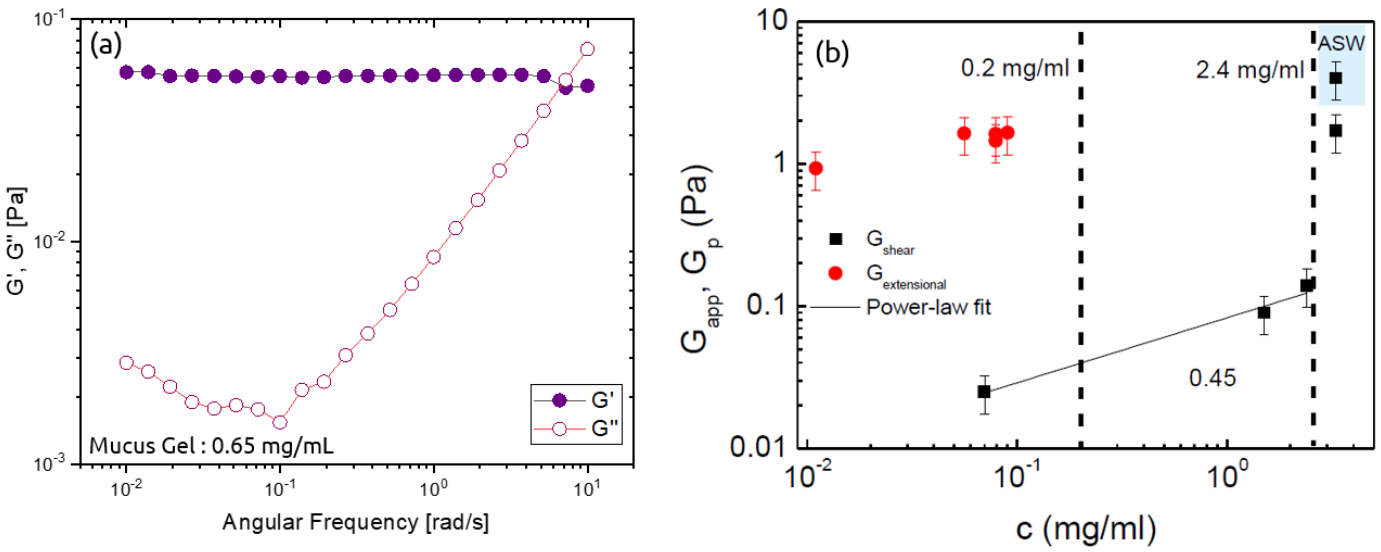

Figure AII.2: (a) Dynamic frequency spectra of a mucus hydrogel with concentration 0.65mg/mL after 2 hours of equilibration (b) Values of plateau modulus (G_p) plotted against concentration. Taken from [39]